Regular Article - Experimental Physics

Measurement of the 1-jettiness event shape observable in deep-inelastic electron-proton scattering at HERA

H1 Collaboration

V. Andreev[50], M. Arratia[34], A. Baghdasaryan[46], A. Baty[9], K. Begzsuren[40], A. Bolz[17], V. Boudry[30], G. Brandt[15], D. Britzger[26], A. Buniatyan[7], L. Bystritskaya[50], A. J. Campbell[17], K. B. Cantun Avila[47], K. Cerny[28], V. Chekelian[26], Z. Chen[36], J. G. Contreras[47], J. Cvach[32], J. B. Dainton[23], K. Daum[45], A. Deshpande[38,42], C. Diaconu[25], A. Drees[38], G. Eckerlin[17], S. Egli[43], E. Elsen[17], L. Favart[4], A. Fedotov[50], J. Feltesse[14], M. Fleischer[17], A. Fomenko[50], C. Gal[38], J. Gayler[17], L. Goerlich[20], N. Gogitidze[17], M. Gouzevitch[50], C. Grab[48], T. Greenshaw[23], G. Grindhammer[26], D. Haidt[17], R. C. W. Henderson[21], J. Hessler[26], J. Hladký[32], D. Hoffmann[25], R. Horisberger[43], T. Hreus[49], F. Huber[18], P. M. Jacobs[5], M. Jacquet[29], T. Janssen[4], A. W. Jung[44], J. Katzy[17], C. Kiesling[26], M. Klein[23], C. Kleinwort[17], H. T. Klest[38,22], S. Kluth[26], R. Kogler[17], P. Kostka[23], J. Kretzschmar[23], D. Krücker[17], K. Krüger[17], M. P. J. Landon[24], W. Lange[17], P. Laycock[42], S. H. Lee[2,39], S. Levonian[17], W. Li[19], J. Lin[19], K. Lipka[17], B. List[17], J. List[17], B. Lobodzinski[26], O. R. Long[34], E. Malinovski[50], H.-U. Martyn[1], S. J. Maxfield[23], A. Mehta[23], A. B. Meyer[17], J. Meyer[17], S. Mikocki[20], V. M. Mikuni[5], M. M. Mondal[27], K. Müller[49], B. Nachman[5], Th. Naumann[17], P. R. Newman[7], C. Niebuhr[17], G. Nowak[20], J. E. Olsson[17], D. Ozerov[50], S. Park[38], C. Pascaud[29], G. D. Patel[23], E. Perez[13], A. Petrukhin[37], I. Picuric[31], D. Pitzl[17], R. Polifka[33], S. Preins[34], V. Radescu[18], N. Raicevic[31], T. Ravdandorj[40], D. Reichelt[12], P. Reimer[32], E. Rizvi[24], P. Robmann[49], R. Roosen[4], A. Rostovtsev[50], M. Rotaru[8], D. P. C. Sankey[10], M. Sauter[18], E. Sauvan[3,25], S. Schmitt[17,a], B. A. Schmookler[38], G. Schnell[6], L. Schoeffel[14], A. Schöning[18], S. Schumann[16], F. Sefkow[17], S. Shushkevich[26], Y. Soloviev[17], P. Sopicki[20], D. South[17], A. Specka[30], M. Steder[17], B. Stella[35], L. Stöcker[16], U. Straumann[49], C. Sun[38], T. Sykora[33], P. D. Thompson[7], F. Torales Acosta[5], D. Traynor[24], B. Tseepeldorj[40,41], Z. Tu[42], G. Tustin[38], A. Valkárová[33], C. Vallée[25], P. van Mechelen[4], D. Wegener[11], E. Wünsch[17], J. Žáček[33], J. Zhang[36], Z. Zhang[29], R. Žlebčík[33], H. Zohrabyan[46], F. Zomer[29]

[1] I. Physikalisches Institut der RWTH, Aachen, Germany
[2] University of Michigan, Ann Arbor, MI 48109, USA
[3] LAPP, Université de Savoie, CNRS/IN2P3, Annecy-le-Vieux, France
[4] Inter-University Institute for High Energies ULB-VUB, Brussels and Universiteit Antwerpen, Antwerp, Belgium
[5] Lawrence Berkeley National Laboratory, Berkeley, CA 94720, USA
[6] Department of Physics, University of the Basque Country UPV/EHU, 48080 Bilbao, Spain
[7] School of Physics and Astronomy, University of Birmingham, Birmingham, UK
[8] Horia Hulubei National Institute for R&D in Physics and Nuclear Engineering (IFIN-HH), Bucharest, Romania
[9] University of Illinois, Chicago, IL 60607, USA
[10] STFC, Rutherford Appleton Laboratory, Didcot, Oxfordshire, UK
[11] Institut für Physik, TU Dortmund, Dortmund, Germany
[12] Institute for Particle Physics Phenomenology, Durham University, Durham, UK
[13] CERN, Geneva, Switzerland
[14] IRFU, CEA, Université Paris-Saclay, Gif-sur-Yvette, France
[15] II. Physikalisches Institut, Universität Göttingen, Göttingen, Germany
[16] Institut für Theoretische Physik, Universität Göttingen, Göttingen, Germany
[17] Deutsches Elektronen-Synchrotron DESY, Hamburg and Zeuthen, Germany
[18] Physikalisches Institut, Universität Heidelberg, Heidelberg, Germany
[19] Rice University, Houston, TX 77005-1827, USA
[20] Institute of Nuclear Physics Polish Academy of Sciences, Kraków, Poland
[21] Department of Physics, University of Lancaster, Lancaster, UK
[22] Argonne National Laboratory, Lemont, IL 60439, USA
[23] Department of Physics, University of Liverpool, Liverpool, UK
[24] School of Physics and Astronomy, Queen Mary, University of London, London, UK
[25] Aix Marseille Univ, CNRS/IN2P3, CPPM, Marseille, France
[26] Max-Planck-Institut für Physik, Munich, Germany
[27] National Institute of Science Education and Research, Jatni, Odisha, India
[28] Joint Laboratory of Optics, Palacký University, Olomouc, Czech Republic

[29] IJCLab, Université Paris-Saclay, CNRS/IN2P3, Orsay, France

[30] LLR, Ecole Polytechnique, CNRS/IN2P3, Palaiseau, France

[31] Faculty of Science, University of Montenegro, Podgorica, Montenegro

[32] Institute of Physics, Academy of Sciences of the Czech Republic, Prague, Czech Republic

[33] Faculty of Mathematics and Physics, Charles University, Prague, Czech Republic

[34] University of California, Riverside, CA 92521, USA

[35] Dipartimento di Fisica Universitá di Roma Tre and INFN Roma 3, Rome, Italy

[36] Shandong University, Jinan, Shandong, People's Republic of China

[37] Fakultät IV-Department für Physik, Universität Siegen, Siegen, Germany

[38] Stony Brook University, Stony Brook, NY 11794, USA

[39] Physics Department, University of Tennessee, Knoxville, TN 37996, USA

[40] Institute of Physics and Technology of the Mongolian Academy of Sciences, Ulaanbaatar, Mongolia

[41] Ulaanbaatar University, Ulaanbaatar, Mongolia

[42] Brookhaven National Laboratory, Upton, NY 11973, USA

[43] Paul Scherrer Institut, Villigen, Switzerland

[44] Department of Physics and Astronomy, Purdue University, West Lafayette, IN 47907, USA

[45] Fachbereich C, Universität Wuppertal, Wuppertal, Germany

[46] Yerevan Physics Institute, Yerevan, Armenia

[47] Departamento de Fisica Aplicada, CINVESTAV, Mérida, Yucatán, Mexico

[48] Institut für Teilchenphysik, ETH, Zurich, Switzerland

[49] Physik-Institut der Universität Zürich, Zurich, Switzerland

[50] Affiliated with an institute covered by a current or former collaboration agreement with DESY, Hamburg and Zeuthen, Germany

[a] e-mail: stefan.schmitt@desy.de (corresponding author)

Abstract The H1 Collaboration reports the first measurement of the 1-jettiness event shape observable τ_1^b in neutral-current deep-inelastic electron-proton scattering (DIS). The observable τ_1^b is equivalent to a thrust observable defined in the Breit frame. The data sample was collected at the HERA ep collider in the years 2003–2007 with center-of-mass energy of $\sqrt{s} = 319\,\mathrm{GeV}$, corresponding to an integrated luminosity of $351.1\,\mathrm{pb^{-1}}$. Triple differential cross sections are provided as a function of τ_1^b, event virtuality Q^2, and inelasticity y, in the kinematic region $Q^2 > 150\,\mathrm{GeV^2}$. Single differential cross sections are provided as a function of τ_1^b in a limited kinematic range. Double differential cross sections are measured, in contrast, integrated over τ_1^b and represent the inclusive neutral-current DIS cross section measured as a function of Q^2 and y. The data are compared to a variety of predictions and include long-standing and more recent Monte Carlo event generators, predictions in fixed-order perturbative QCD where calculations up to $\mathcal{O}(\alpha_s^3)$ are available for τ_1^b or inclusive DIS, and resummed predictions at next-to-leading logarithmic accuracy matched to fixed order predictions at $\mathcal{O}(\alpha_s^2)$. These comparisons reveal sensitivity of the 1-jettiness observable to QCD parton shower and resummation effects, as well as the modeling of hadronization and fragmentation. Within their range of validity, the fixed-order predictions provide a good description of the data. Monte Carlo event generators are predictive over the full measured range and hence their underlying models and parameters can be constrained by comparing to the presented data.

1 Introduction

Measurements in high-energy lepton-proton deep-inelastic scattering (DIS) have played an important role in understanding the structure of Quantum Chromodynamics (QCD) [1–4]. Inclusive neutral-current DIS cross section measure-

ments probe the distribution of partonic constituents of the proton, and test perturbative QCD (pQCD) over a wide range of energy scale. Beyond those inclusive cross sections, dedicated measurements of the shape and substructure of the hadronic final state (HFS) provide rigorous tests of pQCD calculations. Observables related to the HFS are among others the properties of jets, heavy-quark production, or event shape quantities. They are sensitive to the strong coupling constant and the gluon content of the proton. In addition, they can be used to test the modeling of non-perturbative (NP) effects, particularly hadronization and fragmentation. However, comprehensive measurements of HFS observables over the full HFS phase space in neutral-current DIS were not performed in the past due to experimental and theoretical limitations.

Event shapes have been studied extensively in e^+e^- collisions [5–21], and in hadron–hadron collisions [22–32]. Several event shape observables were also measured in neutral-current (NC) DIS using data from the HERA-I data taking period (1992–2000) [33–37], which demonstrated sensitivity to the strong coupling constant $\alpha_s(m_Z)$, as well as to hadronization and resummation effects. Nevertheless, event shapes have not been studied to date as extensively in DIS as in e^+e^- and hadronic collisions due to the more limited precision in predicting event shapes in DIS as compared to e^+e^- collisions [38–41]. In this article, the H1 Collaboration reports the first measurement of the 1-jettiness event shape observable τ_1^b in ep collisions. This variable has theoretical advantages over previously studied event shape observables, since it is free of non-global logarithms [42,43] and thus can be calculated with high theoretical accuracy. Furthermore, it is closely related to event shapes in e^+e^- collisions.

A traditional event shape observable is thrust T [44,45], which quantifies the momentum distribution of the HFS along a defined axis. There is freedom in choosing the projection axis, normalization and reference frames to analyzing the thrust observable in DIS. A common choice of these conditions is given by the Breit frame of reference [46], with the polar angle dividing the event into two hemispheres. These are referred to as the *current* (or *jet*) hemisphere, $\mathcal{H}_C$, and the *target fragmentation* (or *beam*) hemisphere, with polar angles smaller or larger than $\frac{\pi}{2}$, respectively.[1] In the Breit frame, the photon momentum[2] is aligned with the positive z

axis, i.e. $q_b = (0, 0, Q; 0)$. A natural choice for the axis of Thrust is the photon axis with normalization $\frac{Q}{2}$, and thus this variant of thrust is computed as

$$T_{zQ} = 2 \sum_{i \in \mathcal{H}_C} \frac{P_{z,i}}{Q}, \tag{1}$$

where the sum runs over all HFS particles in the Breit frame current hemisphere $\mathcal{H}_C$. This variant of Thrust is a scaling variable [47].

A generalized set of inclusive observables defined with respect to the Breit frame axis, named *current jet thrust* observables, is discussed in Ref. [48]. Power corrections, next-to-leading order QCD corrections, and resummed predictions for such observables have been calculated [43,49–55]. A change in notation has likewise been introduced,

$$\tau_{zQ} = 1 - T_{zQ}. \tag{2}$$

It was shown that τ_{zQ} is infrared and collinear safe, that it fulfills the criteria required for analytic or automatized resummation, and that it is free of non-global logarithms [47,56–58].

In the framework of soft-collinear effective theory (SCET), τ_{zQ} is one variant of a more general class of global event-shape observables called 1-jettiness [52,59–61],

$$\tau_{zQ} = \tau_1^b = \frac{2}{Q^2} \sum_{i \in X} \min \left(x_{\text{Bj}} P \cdot p_i, (q + x_{\text{Bj}} P) \cdot p_i \right), \tag{3}$$

where in this case i runs over *all* final state particles, which renders the calculation of τ_1^b free of non-global logarithms. Here, x_{Bj} is the Bjorken-x scaling variable, q is the exchanged photon four-momentum, and P is the incoming proton four-momentum. The observable τ_1^b is a special case of a general class of N-jettiness observables [59,62–65]. Using momentum conservation, τ_1^b can be rewritten

$$\tau_1^b = 1 - 2 \cdot \sum_{i \in X} \max \left(0, \frac{q \cdot p_i}{q \cdot q} \right)$$
$$= 1 - 2 \cdot \sum_{i \in \mathcal{H}_C} \frac{q \cdot p_i}{q \cdot q}, \tag{4}$$

where the sum runs over all HFS particles in the first expression, but only over particles in the Breit frame current hemisphere $\mathcal{H}_C$ in the second expression. Following Eq. (4) the 1-jettiness is proportional to the sum of particle 4-momenta radiated into $\mathcal{H}_C$, and projected onto the photon four-momentum. It ranges from zero to unity, with $\tau_1^b \sim 0$ indicating an event structure with a single collimated jet emitted into $\mathcal{H}_C$ along the photon direction. There are DIS event configurations at low x_{Bj} where the current hemisphere is empty, corresponding to $\tau_1^b = 1$ [47,51,61]. When the full

---

[1] This sign convention for the z axis in the Breit frame is opposite to that of the *HERA laboratory coordinate system* where the proton moves along the positive z direction, while in the Breit frame as defined here it moves along the negative z direction. The photon then moves in the positive z direction [47]. Some HERA papers define the z-axis in the Breit frame with opposite sign.

[2] In NC DIS, the interaction is mediated by a photon, γZ interference, or Z exchange, which is denoted *photon exchange* in the following. The photon four-momentum q is determined from the incoming and outgoing

Footnote 2 continued
lepton four-vectors, $q = k - k'$. The photon virtuality is $Q^2 = -q \cdot q$.

range of τ_1^b is considered, $\tau_1^b \in [0, 1]$, each event in NC DIS has an associated value of τ_1^b.

This article presents a first measurement of τ_1^b, which constitutes the first triple-differential measurement of an hadronic event shape observable over the full phase space of selected NC DIS event kinematics. It is made possible by recent theoretical developments and improved experimental reconstruction techniques and is based on data recorded with the H1 detector at the HERA collider for ep collisions at $\sqrt{s} = 319$ GeV. Differential cross sections as a function of τ_1^b, as well as the triple-differential cross section as a function of photon virtuality Q^2, event inelasticity y, and τ_1^b, are reported over a large kinematic range. Inclusive DIS cross sections as a function of Q^2 and y, obtained by integrating the triple-differential cross section, are also measured. The data are compared to theoretical calculations based on Monte Carlo (MC) event generators and pQCD, probing their sensitivity to parton showering, resummation, α_s, and non-perturbative effects.

2 Experimental setup

The data were taken with the H1 detector in the years 2003 to 2007 using electron or positron[3] beams that were collided with a proton beam at a center-of-mass energy of $\sqrt{s} = 319$ GeV. The data correspond to an integrated luminosity of $\mathcal{L} = 351.1$ pb^{-1} [66]. The H1 experiment [67–72] was a general purpose particle detector with full azimuthal coverage around the electron–proton interaction region. The H1 Collaboration uses a right handed coordinate system, where the proton beam direction defines the positive z axis. The nominal interaction point is located at $z = 0$.

The H1 detector consists of several subsystems. The main subsystems used for this analysis are the tracking detectors, the liquid argon (LAr) calorimeter, and the backward calorimeter (SpaCal). All these systems are situated inside a superconducting solenoid that provides a magnetic field of 1.16 T. The central tracking system consists of drift and proportional chambers, together with silicon-strip detectors close to the interaction region and covers the polar angular range $15° < \theta < 165°$. The transverse momentum resolution of charged particles is $\sigma_{p_T}/p_T = 0.2\% \, p_T/\text{GeV} \oplus 1.5\%$.

The LAr sampling calorimeter consists of an electromagnetic section made of lead absorbers and an hadronic section with steel absorbers, covering the polar angular range $4° < \theta < 154°$. The energy resolution is $\sigma_E/E = 11\%/\sqrt{E/\text{GeV}} \oplus 1\%$ for electrons and $\sigma_E/E \simeq 55\%/\sqrt{E/\text{GeV}} \oplus 3\%$ for charged pions. The LAr calorime-

ter is used for triggering and particle reconstruction in this analysis.

The SpaCal ('Spaghetti Calorimeter') is a lead-scintillating fiber calorimeter with electromagnetic and hadronic sections, covering the backward direction with polar angular range $153° < \theta < 177°$. The electromagnetic energy resolution $\sigma(E)/E$ is $7\%/\sqrt{E/\text{GeV}} \oplus 1\%$, and in the hadronic section it is $(56 \pm 13)\%$ for charged pions.

Online triggering and event selection follow the procedure described in Ref. [73]. Events are triggered by a high-energy cluster in the LAr calorimeter, with the scattered electron identified using isolation criteria. Events are accepted if the scattered electron has energy $E'_e > 11$ GeV and is found in the high-efficient regions of the LAr calorimeter trigger system, which corresponds to about 90% of its η–φ coverage. The trigger efficiency for inclusive DIS events is greater than 99%.

In order to suppress non-collision backgrounds from cosmic muons, beam-gas interactions, and high energetic muons produced off the proton beam in the HERA tunnel, a triggered event must fulfill certain requirements [73,74]. Events with an energy deposition in the range $\theta > 175°$ are found to be sensitive to non-collision backgrounds and are removed. Events with a topology similar to QED Compton events are also removed [73].

Tracks of charged particles are reconstructed from hits in the tracking detectors. The energy depositions of charged and neutral particles in the calorimeters are clustered and calibrated. Particle candidate four-vectors are then reconstructed offline using an energy-flow algorithm which combines information from tracks with that from clusters [75–77]. The energy of particle candidates is calibrated using a neural-network based shower-classification algorithm and a dedicated jet-calibration sample [78]. The scattered electron candidate is identified as the electromagnetic cluster in the LAr calorimeter which has the highest energy in the event, and which satisfies isolation criteria and is matched with a track [79].

Radiative photons may distort the kinematic reconstruction. Isolated high-energy depositions in the central or backward part of the electromagnetic calorimeters ($\theta > \frac{\pi}{3}$) are found to have a good association with photons radiated off the incoming or scattered electron. Such clusters are treated in the same manner as radiated photons at particle level. If their angular distance to the scattered electron candidate is smaller than the distance to the negative z-axis, they are recombined with the scattered electron to form a dressed scattered electron with four-vector p_e; otherwise, their energy deposition is removed from the event record. This procedure suppresses photons from initial-state QED radiation, which effectively reduce the energy of the incoming lepton. In addition, it provides well-reconstructed observables in the presence of final-state QED radiation. All remaining particle candidates

---

[3] The term 'electron' is used in the following to refer to both electrons and positrons.

which are not classified as the scattered electron, comprise the hadronic final state (HFS), with their sum corresponding to the HFS four-vector, p_h. The incoming electron energy is reconstructed by the Σ method [80], which makes use of the energy and longitudinal momentum of $p_h + p_e$. The photon four-vector q is calculated using the incoming electron energy and p_e. HFS particles satisfying $p_i \cdot q < 0$ are associated to the current hemisphere $\mathcal{H}_C$ in the Breit frame, with their sum forming the current-hemisphere four-vector p_c.

The DIS kinematic observables are the momentum transfer Q^2, the inelasticity y and the scaling variable Bjorken-x. For events without initial- or final-state photons, these are related to the four-vectors q, P and the centre-of mass energy $\sqrt{s}$: $Q^2 = -q \cdot q$, $x = Q^2/(2P \cdot q)$, $Q^2 = sxy$. For this paper, the DIS observables are determined from the four-vectors p_e (with energy E_e and transverse momentum $P_{T,e}$) and p_h, using the IΣ method [80,81],

$$y_\Sigma = \frac{\Sigma_h}{\Sigma_h + \Sigma_e}, \quad Q^2_\Sigma = \frac{P^2_{T,e}}{1 - y_\Sigma},$$
$$x_{I\Sigma} = \frac{E_e}{E_{p0}} \frac{\cos^2 \frac{\theta_e}{2}}{y_\Sigma}. \tag{5}$$

Where appropriate, the electron method is employed to obtain alternative measures of the inelasticity and the momentum transfer as

$$y_e = 1 - \frac{\Sigma_e}{2E_{e0}} \quad \text{and} \quad Q^2_e = \frac{P^2_{T,e}}{1 - y_e}. \tag{6}$$

In these definitions, $\Sigma_i = E_i - P_{z,i}$ for $i = e, h$. The electron and proton beam energies are $E_{e0} = 27.6 \, \text{GeV}$ and $E_{p0} = 920 \, \text{GeV}$, respectively.

The IΣ method achieves good resolution in y over the entire kinematic range [80–82]. Inserting $-Q^2_\Sigma$ for $q \cdot q$ in Eq. (4) provides best resolution for the calculation of τ^b_1 [83]. However, the electron method provides superior resolution in Q^2 and is therefore used for Q^2 dependent measurements, $\propto \frac{d\sigma}{dQ^2}$. The electron-beam energy does not enter the equations of the IΣ method, which thereby is largely insensitive to initial state QED radiative effects. The hadronic angle is defined in this analysis as $\gamma_h = 2 \arctan \frac{\Sigma_h}{P_{T,e}}$.

To achieve high resolution and to reduce initial-state QED radiation effects, events are selected as follows: the ratio of the transverse momentum of the HFS and scattered lepton satisfies $0.6 < P_{T,h}/P_{T,e} < 1.6$; their difference satisfies $P_{T,h} - P_{T,e} < 5 \, \text{GeV}$; and the longitudinal energy-momentum balance is in the range $45 < \Sigma_h + \Sigma_e < 62 \, \text{GeV}$. A current hemisphere four-vector is formed from all HFS particles contained in $\mathcal{H}_C$. Its polar angle θ_c and pseudorapidity η_c, defined in the laboratory frame, are used to classify phase-space regions with lower resolution or reconstruction performance, and to suppress QED radiative effects and contributions from non-collision backgrounds. The following types of events are rejected at detector-level:
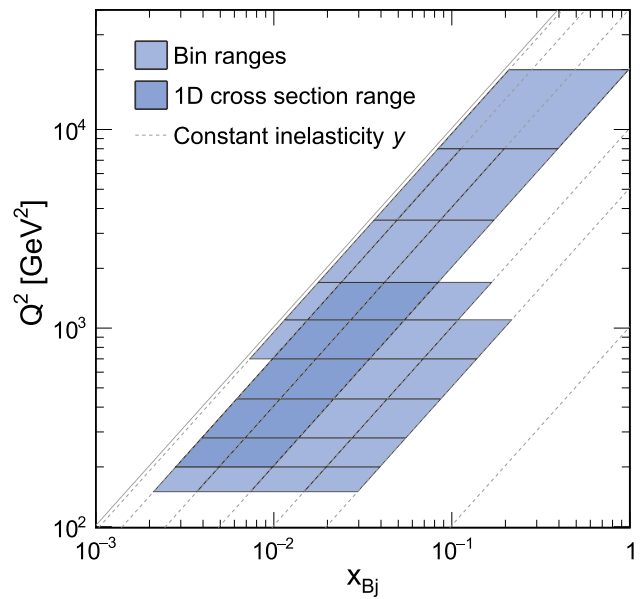
Fig. 1 DIS kinematic plane as a function of x_{Bj} and Q^2. The kinematic range of the measurement is displayed as colored area. The dark shaded area indicates the kinematic range of the reported single-differential cross section ($200 \le Q^2 < 1700 \, \text{GeV}^2$ and $0.2 \le y < 0.7$)

- Events with $\theta_c - \gamma_h > \frac{\pi}{2}$, or with $\theta_c > 3.05$, or with $\theta_c > 2.6$ where β of the boost vector $b = 2x_{Bj}P + q$ ($\beta = \frac{\vec{b}^2}{b^2_E}$) fulfills $\beta > 0.9$, are found to be events with an initial state radiated photon or where a radiated photon was converted to hadrons;
- Events with $\theta_c < 0.12$ cannot be reconstructed well due to limited acceptance in the forward direction;
- Events at low τ^b_1 ($\tau^b_1 < 0.3$) are found to have poor resolution when $\theta_c/\gamma_h > 1.3$;
- Events at large τ^b_1 and low Q^2 ($\tau^b_1 > 0.65$ and $Q^2 < 700 \, \text{GeV}^2$) have poor resolution when $\beta > 0.9$ and $P_{T,c}/P_{T,e} < 0.35$;
- Events at very high value τ^b_1 ($\tau^b_1 > 0.95$) have poor resolution when $\beta > 0.97$;
- Events at low Q^2 ($Q^2 < 700 \, \text{GeV}^2$) have poor resolution for $\eta_c + \ln(\tan \frac{\gamma_h}{2}) > 0.3$.
- Events with $y_e > 0.94$ are removed in order to suppress background contributions from photoproduction.

After the application of all acceptance, background and cleaning cuts, about 35 to 80% of the events generated within the phase space of the measurement are accepted at the detector-level. The cross sections measured in this paper are defined on the particle level, where none of the above technical conditions are applied.

The final selected NC DIS kinematic range of the analysis is shown in Fig. 1 as a function of x_{Bj} and Q^2.

The kinematic range is limited by acceptance, resolution, and trigger: The polar-angle acceptance of the LAr calorime-

ter, $\theta \lesssim 154°$, defines the Q^2 region of the measurement, $Q^2 > 150\,\text{GeV}^2$; The electron energy acceptance corresponds to $y \lesssim 0.7$ for $Q^2 \lesssim 1000\,\text{GeV}^2$; The inelasticity is required to be $y > 0.05$, since acceptance and resolution deteriorate for lower y, where the hadronic angle γ_h becomes small and the Lorentz-factor β of the boost vector approaches unity.

The binning used in this analysis is also presented in Table 1.

Over most of the phase space the binning is dictated by the resolution of τ_1^b. Coarser binning is chosen at the boundaries of the kinematic range due to the following factors:

- low y or large Q^2: large values of τ_1^b have low statistics or lower resolution;
- low y and $\tau_1^b < 0.05$: very low cross section which cannot be resolved.

Altogether 308 cross section values are measured. The respective highest τ_1^b bins ($0.98 \leq \tau_1^b \leq 1$ and $0.6 < \tau_1^b \leq 1$) include events with $\tau_1^b = 1$, in which the current hemisphere is empty. Such events are related to low values of x [47,51,61], and are present because τ_1^b is defined in the Breit frame. They are absent for event shape observables defined in the partonic center-of-mass frame, like thrust in e^+e^- collisions [43,61].

3 Monte Carlo simulations and model predictions

MC event generators are used to correct the data for detector acceptance and resolution effects, and for contributions from ep collisions outside the phase-space of this analysis. The generated events are processed with a detailed simulation of the H1 detector based on GEANT3 [84], supplemented by fast shower simulations [85–90]. The simulated data are reconstructed and processed with the same analysis algorithm as the real data [91–97].

Detector effects are corrected using *regularized unfolding*, based on the simulation of NC DIS events using the MC event generators Djangoh 1.4 [98] and Rapgap 3.1 [99]. Djangoh uses Born level matrix elements for NC DIS and dijet production and applies the color dipole model from Ariadne [100] for higher-order emissions. Rapgap implements Born level matrix elements for NC DIS and dijet production and uses the leading logarithmic approximation for parton shower emission. Both generators are interfaced to Heracles [101] for higher order QED effects at the lepton vertex. Both generators utilise the CTEQ6L parton distribution function (PDF) set [102] and the Lund hadronization model [103,104]. Hadronization model parameters were determined by the ALEPH Collaboration [105].

Contributions to the event yield from processes other than NC DIS are simulated with a variety of MC event generators. Photoproduction events are simulated using Pythia 6.2 [106, 107]. Events with di-lepton production are generated using Grape [108]. A sample of QED Compton events is simulated using the program Compton [109]. Deeply virtual Compton scattering (DVCS) is simulated with Milou [110]. NC DIS events for lower values of Q^2 and for charged current DIS are simulated with Djangoh. Overall, more than 3.4×10^8 signal events were simulated with Djangoh and Rapgap, and about 5.3×10^8 events were simulated in total.

The fully-corrected τ_1^b cross section measurements are compared to a set of theoretical predictions. The following classes of prediction are studied: two long-standing MC event generators as used at HERA; three more recent general-purpose event generators which are widely used in high-energy physics; one dedicated event generator incorporating transverse-momentum dependent effects; and two variants of fixed-order predictions. In order to explore the sensitivity of the data to various QCD effects, in each MC event generator one element is varied, such as the parton shower model, the fixed-order prediction and its matching or merging procedure with the parton shower, the hadronization model, or the PDF set. The fixed-order predictions include variations of the renormalization and factorization scales. In addition, dedicated predictions for the inclusive NC DIS cross sections are studied. The following MC event generators from the HERA era are considered:

- Djangoh 1.4 and Rapgap 3.1, similar to those described above, but with radiative effects switched off in Heracles.

The following recent MC event generators are studied:

- Pythia 8.3 [111,112], where the impact of the parton-shower is studied by employing three different parton-shower models: (i) 'default' dipole-like $p_\perp$-ordered shower with a local dipole recoil strategy (Pythia 8.310) [113], (ii) $p_\perp$-ordered Vincia parton shower based on the antenna formalism at leading color (Pythia 8.307) [114–117], and (iii) the Dire [118–120] parton shower which is an improved dipole-shower with additional treatment of collinear enhancements (Pythia 8.307). All models use the Pythia 8.3 default Lund string model for hadronization [112] and the PDF4LHC21 PDF set [121] for the hard PDFs.
  The Vincia and Dire parton shower use a value of 0.118 for the strong coupling at the mass of the Z boson.
- Powheg Box plus Pythia (Powheg+Pythia) [122] implements predictions in NLO QCD matched to parton showers using the Powheg method [123,124], where the radiation phase space is parameterized according to the Frixione–Kunszt–Signer (FKS) subtraction tech-

Table 1 Binnings used in the analysis

Observable	Binning name	Notation	Binning
τ_1^b	τ_1^b nominal	$b_{\tau_1^b}^{(11)}$	[0, 0.05, 0.1, 0.15, 0.22, 0.3, 0.4, 0.54, 0.72, 0.86, 0.98, $1.0 + \epsilon$]
τ_1^b	τ_1^b coarse	$b_{\tau_1^b}^{(8)}$	[0, 0.05, 0.1, 0.15, 0.22, 0.3, 0.4, 0.6, $1.0 + \epsilon$]
τ_1^b	τ_1^b coarse low y	$b_{\tau_1^b}^{(7)}$	[0, 0.1, 0.15, 0.22, 0.3, 0.4, 0.6, $1.0 + \epsilon$]
y	y	b_y	[0.05, 0.1, 0.2, 0.4, 0.7, 0.94]
Q^2	Q^2	b_{Q^2}	[150, 200, 280, 440, 700, 1100, 1700, 3500, 8000, 20,000] (GeV^2)

nique [125]. Dedicated momentum mappings preserve the DIS kinematic variables. The NLO predictions (up to $\mathcal{O}(\alpha_{\mathrm{s}})$) are then interfaced to parton showers and hadronziation from Pythia 8.308.

- Herwig 7.2 [126], where the impact of different modelling of the hard interaction and its merging or matching with the parton-shower model is studied in three variants: The default prediction implements leading-order matrix elements supplemented with an angular-ordered parton shower [127] and cluster hadronization model [128,129]. The second variant utilises MC@NLO [130] which implements NLO matrix element corrections. Matching with the default angular-ordered parton shower is performed [131]. The third variant also utilises NLO matrix elements, but with dipole merging and a dipole parton shower [131]. Herwig-generated events are further processed with Rivet [132].

- Sherpa 2.2 [133,134], where the modelling of hadronization effects can be studied by using two different hadronization models. The default Sherpa 2.2 predictions are based on multi-leg tree-level matrix elements from Comix [135] that are combined in the CKKW merging formalism [136] with dipole showers [137,138] and supplemented with the cluster hadronization as implemented in AHADIC++ [139]. As an alternative prediction, the parton-level calculation is supplemented with the Lund string fragmentation model [140].

- Predictions from the pre-release version of Sherpa 3.0 [141] are provided by the Sherpa authors featuring a new cluster hadronization model [142] and matrix element calculation at NLO QCD obtained from OpenLoops [143] with the Sherpa dipole shower [138] based on the truncated shower method [144,145]. The predictions are associated with scale uncertainties from a 7-point scale variation by factors of two.

The following dedicated MC event generators are studied:

- Cascade 3 [146] implements off-shell processes via the automated matrix element calculators KaTie [147] and Pegasus [148], parton shower and hadronization through

Pythia 6. This utilises transverse momentum dependent (TMD) PDF sets in the parton branching (PB) methodology [149]. Two PB TMD PDF sets are studied, denoted as *set 1* and *set 2* [150]. They differ primarily in the scale choice for QCD evolution.

The following exact QCD predictions are studied:

- Next-to-next-to-leading order (NNLO) dijet predictions in perturbative QCD up to third order in α_{s} ($\mathcal{O}(\alpha_{\mathrm{s}}^3)$) are obtained for the process $ep \rightarrow e + 2\text{jets} + X$ with the program NNLOJET [55,151–153]. The factorization and renormalization scales are chosen to be $\mu = Q$. Scale uncertainties are determined by the largest difference in the 7-point scale-variation prescription, with scale factors 0.5 and 2.
  The PDF set PDF4LHC21 [121] is used. Non-perturbative correction factors are determined using Djangoh 1.4 and Rapgap 3.1 and are applied to these parton-level predictions as multiplicative correction factors for hadronization effects. These NNLO-dijet predictions are valid only in the region where the $ep \rightarrow e + 2\text{jets} + X$ process dominates and hadronization corrections are small. This corresponds to the region $\tau_1^b \gtrsim 0.1$ and $\tau_1^b \neq 1$.

- Analytic predictions are provided in NNLO⊗NLL′⊗Had accuracy [154], using NLO-dijet matrix elements projected onto the NNLO NC DIS cross section [155] and supplemented with automatized next-to-leading logarithmic accuracy using the Caesar framework [56–58] as implemented in the Sherpa framework [156]. For these predictions, dedicated hadronization corrections are applied as a multiplicative correction matrix obtained from Sherpa 3.0 [157].

Further predictions for τ_1^b have been reported previously but are not available here. These include NNLO predictions supplemented with parton shower [155], next-to-NLL predictions [158], analytic NLL predictions [61], and N3LO predictions using the projection to Born method and a dispersive model for hadronization effects [55,159].

The following predictions are compared to the inclusive NC DIS cross sections measured in bins of Q^2 and y:

- Predictions in NNLO pQCD are obtained with the program Apfel++ [160,161], using the three loop splitting and coefficient functions [162–165] together with the PDF set NNPDF31_nnlo_as_0118. The predictions are associated with PDF uncertainties and with scale uncertainties, where the latter are defined as 7-point scale variations in the coefficient functions. An alternative prediction is obtained with the H1PDF2017NNLO PDF set [166].
- Predictions in approximate next-to-next-to-next-to-leading order (aN3LO) are obtained for inclusive NC DIS cross sections using the program Apfel++ [160,161] and using the MSHT PDFs at a3NLO order [167] and four-loup splitting functions from Refs. [168–170].

4 Data correction: regularized unfolding

The data are corrected for detector effects, background processes, and higher-order QED effects using regularized unfolding [171,172]. This section presents the unfolding procedure and the measurement of the fully-corrected cross sections. In addition, correction factors for hadronization and electroweak effects are discussed.

The signal Monte Carlo generators Djangoh and Rapgap are used together with the detailed simulation of the H1 detector to generate synthetic detector-level events along with corresponding particle-level events (MC event simulation). Within the scope of the analysis, the detector response is found to be well modelled in all studied aspects, which is essential for obtaining accurate unfolding results. Figure 2 shows comparison of these simulations to data for the observables Q^2, y, and τ_1^b.

Both MC event simulations, although based on different physics models, are found to describe the data reasonably well, where typically Rapgap is closer to the data than Djangoh. Some differences are observed in the peak region of τ_1^b and at very small τ_1^b. Overall, the peak seems to be shifted to somewhat lower τ_1^b as compared to data, for both models. Comparisons to other observables, related closely to the detector performance, are discussed in the following.

Figure 3 shows the distribution of P_z^{Breit}, the particle-candidate longitudinal momentum in the Breit frame, compared with simulations for reconstructed clusters and tracks. Good overall agreement between simulations and data is observed, for both clusters and tracks.

The measurement of τ_1^b includes only particle candidates of the current hemisphere. Figure 4 shows relative contributions from different polar angular regions θ and particle energies E. The largest contributions are from objects in the central detector ($25 < \theta < 153°$), and from objects

with large energy ($E > 1.0 \text{ GeV}$). Both types of object are measured well by the relevant H1 sub-detector components, and are modelled well by the MC event simulations. For a small fraction of events with large momentum contribution from tracks some differences become apparent, and Rapgap is closer to the data than Djangoh.

At the particle level (also denoted as *generator* or *hadron level*), the scattered electron is identified with the electron emitted at the DIS vertex. In the case of a photon radiated off the incoming or scattered lepton, the photon is recombined with the scattered electron if the angular distance is smaller than the angular distance to the $-z$-axis; otherwise it is removed from the event record.

The HFS is formed from all remaining particles with proper lifetime $c\tau > 10 \text{ mm}$. The DIS kinematic observables at the particle level are then computed using Eqs. (5) and (6).

The triple-differential cross section is reported as a function of τ_1^b in bins of (Q^2, y), and is obtained as

$$\frac{d\sigma_i}{d\tau_1^b}(Q^2, y) = \frac{\left(A^+(\vec{n}_{\text{data}} - \vec{n}_{\text{Bkg}})\right)_i}{\mathcal{L} \cdot \Delta_{\tau_1^b, i}} \cdot c_{\text{QED},i}, \tag{7}$$

where $\vec{n}_{\text{data}}$ denotes a large data vector of event counts; $\vec{n}_{\text{Bkg}}$ is a corresponding vector with the estimated number of events from processes other than high-Q^2 inclusive NC DIS; $\Delta_{\tau_1^b, i}$ is the bin width of the ith bin of the respective τ_1^b distribution; and A^+ denotes the regularized inverse of the detector response matrix. The parameter c_{QED} is the QED correction factor, and $\mathcal{L}$ specifies the integrated luminosity of the measurement. For this analysis, $\mathcal{L} = 351.1 \text{ pb}^{-1}$ [66], where the e^+ beam data contribute an integrated luminosity of 191.0 pb^{-1}, and the e^- beam data have an integrated luminosity of 160.1 pb^{-1}.

The detector response matrix A is determined using both signal MC event simulators. The TUnfold package [172] is used to calculate the regularized inverse A^+ and to propagate its uncertainties. Finer binning is used at detector than at particle level; typically there are 12 bins in the detector-level histogram. The vector $\vec{n}$ has 4331 entries in the extended detector-level phase space, $0.01 < y < 0.94$ and $Q^2 > 60 \text{ GeV}^2$, and the vector $A^+\vec{n}$ has 572 entries at the particle level. The extended detector-level phase space in y and Q^2 accounts for migrations into and out of the fiducial measurement phase space. In order to obtain the final 324 cross section points from the 572 values, two adjacent values are combined each, with exceptions made at lowest and largest τ_1^b. This procedure stabilizes the unfolding and reduces dependencies on the MC models. The regularization procedure employs the so-called *curvature* mode of TUnfold, which approximates second derivatives, and it acts on the differences of the unfolded results and the MC predictions as a bias distribution. The regularization is applied separately for
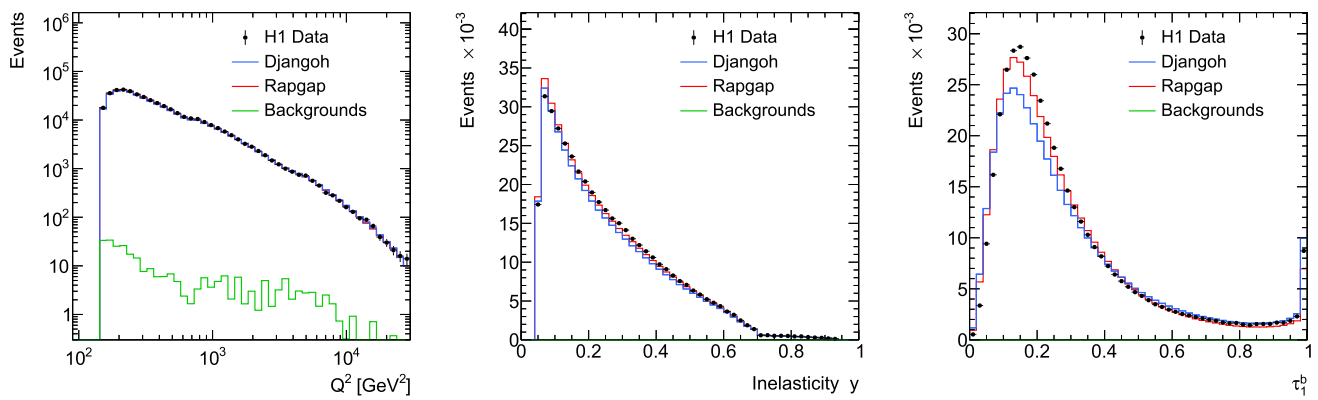
Fig. 2 Detector level distributions of Q^2 (left), y (middle), and τ_1^b (right) of the selected data. The definition of these observables is given by Eq. (5) and (6). The data are compared to the MC event simulations Djangoh and Rapgap. Both simulations include estimated background contributions from processes other than high-Q^2 NC DIS, as indicated by the green line (visible on logarithmic scale)
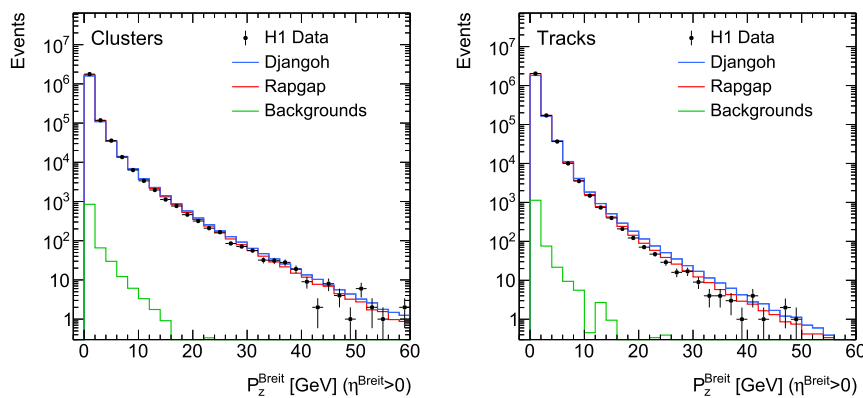
Fig. 3 The longitudinal momentum P_z^{Breit} in the Breit frame of reconstructed particle candidates in the selected events. Only particle candidates with $\eta^{\text{Breit}} > 0$ are displayed, since only those contribute to the actual calculation of τ_1^b. Particle candidates are defined by an energy-flow algorithm taking clusters and tracks into account. Left: the P_z^{Breit} distribution for clusters not associated with a track, right: the P_z^{Breit} distribution for objects associated with a track. The detector-level data are compared to the MC event simulations Djangoh and Rapgap, which include further MC samples for background processes. Further details are given in the Fig. 2 caption

each τ_1^b distribution in the individual (Q^2, y) intervals. The regularization parameter is set to a small value $\tau = 10^{-3.2}$ as suggested by the analysis of Stein's Unbiased Risk Estimator, SURE [173]. The regularization has a moderate impact on the result, and reduces large fluctuations and sizable negative correlations between adjacent data points in some regions of the analysis.

The background vector $\vec{n}_{\text{Bkg}}$ consists of events from photoproduction, charged current DIS, di-lepton production, and DVCS processes. A small number of simulated events which are outside the enlarged phase space at particle level (e.g. $y < 0.01$, or $Q^2 < 120\,\text{GeV}^2$) but migrate into the enlarged detector-level phase space are treated as background, and are also included in $\vec{n}_{\text{Bkg}}$ (acceptance correction).

The multiplicative factor c_{QED} corrects the data for higher-order QED effects and for the positron charge. It is defined as the ratio of the cross section predicted without ($\sigma_{\text{norad}}^{e^- p}$)

to the one with QED radiative effects (σ_{rad}). The factors are determined using the Djangoh event generator, where higher-order QED effects are implemented from Heracles [101]. The factors are validated with Rapgap. The denominator σ_{rad} includes radiative cross sections for electron–proton and positron–proton scattering with relative integrated luminosity weights as for real data. The numerator $\sigma_{\text{norad}}^{e^- p}$ is defined for non-radiative electron–proton scattering ($e^- p$). The resulting cross section measurements are therefore reported for $e^- p$ scattering.[4] The effects of longitudinal polarization of the lepton beam are negligible, due to a nearly balanced mixture of running periods with opposite lepton beam helicities. The QED correction c_{QED} corrects for first-order real emission of photons off the lepton line, including QED Compton

---

[4] At earlier HERA publications $e^+ p$ cross sections were commonly reported.
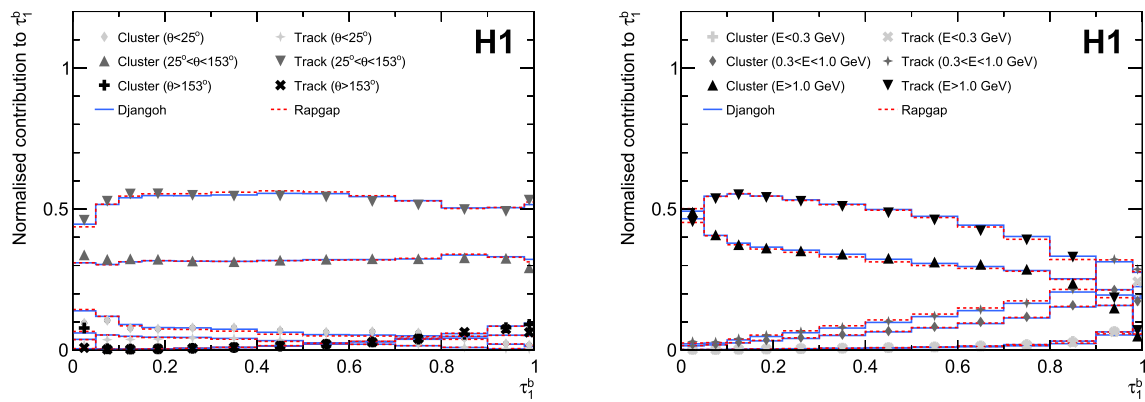
Fig. 4 Left: The normalized contribution to τ_1^b for differently reconstructed particle candidates (tracks or clusters as defined in Fig. 3) in three distinct polar regions θ. The regions are chosen according to θ-ranges, where different components of the H1 detector are relevant for particle reconstruction [69–72]. Right: The normalised contribution to τ_1^b for different ranges of particle energies E and for differently reconstructed particle candidates. The data are compared to the MC event simulations Djangoh and Rapgap. The relative contributions are obtained by calculating a weight $w = \sum_{\text{contrib}} P_z^{\text{Breit}} / \sum_{\text{all}} P_z^{\text{Breit}}$ for each event and each contribution. The resulting distributions are normalized to the τ_1^b distribution

enhancement, photonic vertex correction, and purely photonic self-energy contributions at the external lepton lines. This defines the *non-radiative cross section level* ($\sigma_{\text{norad}}^{e^- p}$), which is reported as the main result of the paper. In line with many previous HERA publications on similar topics the data still include higher-order purely weak effects, self-energy corrections of the exchanged bosons, second order electroweak corrections, and photon-PDF induced contributions.

The QED correction factors c_{QED} are largely independent of the kinematic variables τ_1^b, Q^2, and y owing to the use of the IΣ method and the treatment of radiated photons at the radiative particle level. Effectively, c_{QED} corrects mainly for the cut on the longitudinal energy-momentum balance (($E - P_z)_{\text{gen}} > 45\,\text{GeV}$), which has no effect at the non-radiative cross section level, but is active at the radiative particle-level. When the inverse of c_{QED} is applied, the cross section at the radiative level discussed above is obtained (see also Ref. [83]), where the treatment of radiated photons is relevant.

To simplify comparisons with future theoretical calculations, additional correction factors are determined which optionally can be applied:

- The correction factor c_{NoZ} corrects further for all leading and subleading electroweak corrections, which are γZ and pure Z-exchange, and first order purely weak vertex, self-energy and box corrections. Hence, only leptonic and hadronic corrections to the photon self-energy remain ($\sigma_{\gamma-\text{only}}$).
- The correction factor c_{Born} corrects further to the so-called *DIS Born level* ($\sigma_{\text{Born}}^{e^- p}$), where first order purely weak vertex, self-energy and box corrections are cor-

rected. In addition, corrections for leptonic and hadronic contributions to the photon and Z self-energy are applied.
- The correction factor $c_{e^+ p}$ corrects the reported $e^- p$ non-radiative cross sections to an $e^+ p$ initial state ($\sigma_{\text{norad}}^{e^+ p}$).

The QED correction factor and the optional correction factors can be summarized as:

$$c_{\text{QED}} = \frac{\sigma_{\text{norad}}^{e^- p}}{\sigma_{\text{rad}}}, \; c_{\text{NoZ}} = \frac{\sigma_{\gamma-\text{only}}}{\sigma_{\text{norad}}^{e^- p}}, \; c_{\text{Born}} = \frac{\sigma_{\text{Born}}^{e^- p}}{\sigma_{\text{norad}}^{e^- p}},$$
$$\text{and } c_{e^+ p} = \frac{\sigma_{\text{norad}}^{e^+ p}}{\sigma_{\text{norad}}^{e^- p}}. \tag{8}$$

The single-differential cross section as a function of τ_1^b in the NC DIS kinematic range, $200 < Q^2 < 1700\,\text{GeV}^2$ and $0.2 < y < 0.7$, is obtained by integrating the triple differential cross section for τ_1^b over (Q^2, y). The inclusive NC DIS cross section as a function of Q^2 and y is obtained by integrating the τ_1^b distribution over the (Q^2, y) range. The single-differential and the inclusive NC DIS cross sections, $\frac{d\sigma}{d\tau_1^b}$ and $\frac{d^2\sigma}{dQ^2 dy}$, are reported separately for $e^- p$ and $e^+ p$ scattering, where only data from the respective running periods were analyzed. Unfolding is carried out separately for $e^+ p$ and $e^- p$ data in these cases.

The result of integrating the τ_1^b distribution, as described above, is consistent with the inclusive DIS cross section reported previously [74]. However, the present measurement is not corrected to the bin center but is reported in intervals of Q^2 and y, whereas previous inclusive DIS cross section measurements were reported as a function of Q^2 and x_{Bj} [74,79,174–177]. This is the first inclusive NC DIS cross section measurement at HERA that is corrected using regularised unfolding.

Fixed order calculations do not account for non-perturbative effects due to hadronization of partons into stable hadrons. Such effects can approximately be accounted for by means of bin-wise multiplicative correction factors c_{Had}, defined as the ratio of calculated particle-level and parton-level cross sections. Such hadronization corrections are determined using Djangoh and Rapgap, which are found to be consistent with each other. These factors are also validated using Pythia 8.3. The hadronization correction factors approximately decrease like $1/Q$, and are found to be similar in size to hadronization corrections reported for e^+e^- at $\sqrt{s} \sim Q$ at PETRA [20,178,179].

5 Uncertainties

The measurement is affected by a number of systematic effects. The following sources of uncertainties are considered:

- Statistical uncertainties of the data are propagated to the unfolded cross sections. This procedure results in bin-to-bin correlations, which are provided as supplementary material on the H1 webpage [180].
- The energy of the scattered lepton is measured with a precision of 0.5% in the central and backward region of the detector, and with 1% precision in the forward region of the detector [74].
  The efficiency of the electron identification algorithm is studied with an alternative track-based algorithm and the data and MC simulation are found to agree within 0.2% at lower Q^2 and 1% for $Q^2 > 3500\,\mathrm{GeV}^2$ [74,181].
- The energies of all clusters and tracks receive scale factors from a dedicated jet energy calibration [73,78]. This calibration procedure results in two independent uncertainty contributions, whether clusters are contained in jets or not. The two contributions are denoted as 'jet energy scale uncertainty' (JES) and 'remaining cluster energy scale uncertainty' (RCES), and both uncertainties are determined by varying the energy of the respective HFS objects by $\pm 1\%$. As compared to the JES, the RCES typically affects objects with lower transverse momenta.
- The polar-angle position of the LAr calorimeter with respect to the Central Tracking Detector (CTD) is aligned with a precision of 1 mrad [74]. This uncertainty component is considered separately for the scattered electron and for the HFS objects.
- The unfolding procedure is associated with several uncertainties. Differences in the migration matrix A when determined from Djangoh or Rapgap are denoted as 'model' uncertainty. Half of the difference in each element A_{ij} is propagated to the unfolded cross section. This applies also to events that migrate from outside the

particle-level phase space into detector-level phase space, and to events that are generated in the particle-level phase space but are not reconstructed at detector-level.
Statistical uncertainties in A from the limited event sample of the simulations are also considered. The size of the regularization parameter has an uncertainty of 50% and that variation is propagated to the resulting cross sections [172]. The considered variation covers alternative procedures to determine the regularization strength, including the minimum global correlation coefficient or the L-curve scan [172].

- Other uncertainty components are found to be negligible on their own, and a conservative bin-to-bin uncorrelated uncertainty of 0.5% is introduced to cover the sum of these. An example of the uncertainties included here is the vertex and electron track reconstruction efficiency, which has an uncorrelated uncertainty of 0.2% [181], The distance between the calorimeter cluster of the scattered electron and a vertex-associated track is not described perfectly by the simulation, and the corresponding efficiency correction introduces an uncorrelated uncertainty of about 0.1 to 0.2%. The uncertainty associated with the choice of the regularization strength in the unfolding procedure is found to be below 0.1%. The contributions from other processes than high-Q^2 NC DIS (*backgrounds*) are estimated from MC simulations and a normalization uncertainty of 100% is considered, which results in an uncertainty smaller than 0.1%.
- The normalization uncertainty is found to be 2.7%, and is dominated by the uncertainty on the integrated luminosity [66]. Other normalization uncertainties are negligible in comparison. For example, the efficiency of the trigger is found to be higher than 99.5% [73,74] and the related uncertainty is smaller than 0.5%. Further normalization uncertainties are related to the electron identification, the noise suppression algorithm in the LAr, and to the track and vertex identification.
- The QED correction factors were determined separately with Djangoh and Rapgap and very good agreement was found. While both MC generators implement QED corrections from Heracles, previous studies showed that these are consistent with the program Hector [182] and EPRC [183], and that the contribution from the two-photon exchange, which is not implemented in Heracles, is negligible [74,184]. Consequently, the uncertainty of the QED correction factors represent only their statistical component, while other uncertainties would be of negligible size, when compared to other uncertainty sources.
- Uncertainties of the hadronization correction factors, relevant for a subset of the comparisons only, are determined as half of the difference between the correction factor obtained from Djangoh and Rapgap.

Fig. 5 The differential cross section $d\sigma/d\tau_1^b$ in the kinematic region $200 \leq Q^2/\text{GeV}^2 < 1700$ and $0.2 \leq y < 0.7$ for e^+p (left) and e^-p scattering at $\sqrt{s} = 319$ GeV. The data are corrected for detector effects (acceptance, resolution) and QED radiative effects. The statistical uncertainties are displayed as vertical error bars, systematic uncertainties as shaded areas. The data are compared to the MC predictions from NNLOJET, NNLO⊗NLL′⊗Had, Pythia 8.3, Powheg Box, Herwig 7.2, Sherpa 2.2, Sherpa 3.0, Djangoh, Rapgap, and KaTie+Cascade 3. Selected parameters are varied in the predictions as indicated in brackets. Colored areas indicate theoretical uncertainties associated with some of the predictions (see text). The lower panel displays the ratio of predictions to data

6 Results

Results for the single-differential and triple-differential 1-jettiness cross sections as well as for the double-differential inclusive NC DIS cross section are presented.

Single-differential cross sections as a function of τ_1^b The single-differential 1-jettiness cross sections $\frac{d\sigma}{d\tau_1^b}$ in NC DIS ep scattering in the kinematic range $200 \leq Q^2 < 1700\,\text{GeV}^2$ and $0.2 \leq y < 0.7$ are measured for e^+p and e^-p collisions in Tables 2 and 3 and displayed in Fig. 5. As no significant differences are observed between the two cross sections, the measurement is repeated using the sum of both datasets, corrected to e^-p scattering cross sections, in Table 4 and Fig. 6. The statistical uncertainty in the data is typically around 2 to 4% and the systematic uncertainty is of order 4%. Larger uncertainties are seen for the lowest τ_1^b bin. The differential τ_1^b cross section exhibits a distinct peak at $\tau_1^b \sim 0.13$ and a tail towards high values of τ_1^b. The distinct *DIS peak* is populated by DIS Born-level kinematics with a single hard parton,

the position and shape of which are dominated by hadronization and resummation effects. The tail region is populated by events with hard radiation, including two-jet topologies in the far tail. The cross section at $\tau_1^b \simeq 1$ has a sizeable value, as it includes events with empty current hemisphere in the Breit frame. This event configuration can occur at low x_{Bj} and is studied in a dedicated publication [185]. The data are compared at sufficiently large τ_1^b to NNLO-dijet predictions from NNLOJET up to $\mathcal{O}(\alpha_s^3)$ in the strong coupling. They are compared over the full range in τ_1^b to resummed predictions at NLL accuracy matched to fixed-order predictions at $\mathcal{O}(\alpha_s^2)$ and corrected for hadronization; to various predictions from the recent MC event generators Pythia 8.3, Sherpa 2.2, Sherpa 3.0, Herwig 7.2, and Powheg Box plus Pythia; as well as to the long-standing MC event generators for DIS, Djangoh, Rapgap, and KaTie+Cascade. The agreement between the predictions and data are very similar for e^+p and e^-p cross sections. Further details are discussed below.

Triple-differential cross sections as a function of τ_1^b, Q^2, and y Triple-differential cross sections are presented in Tables 5,
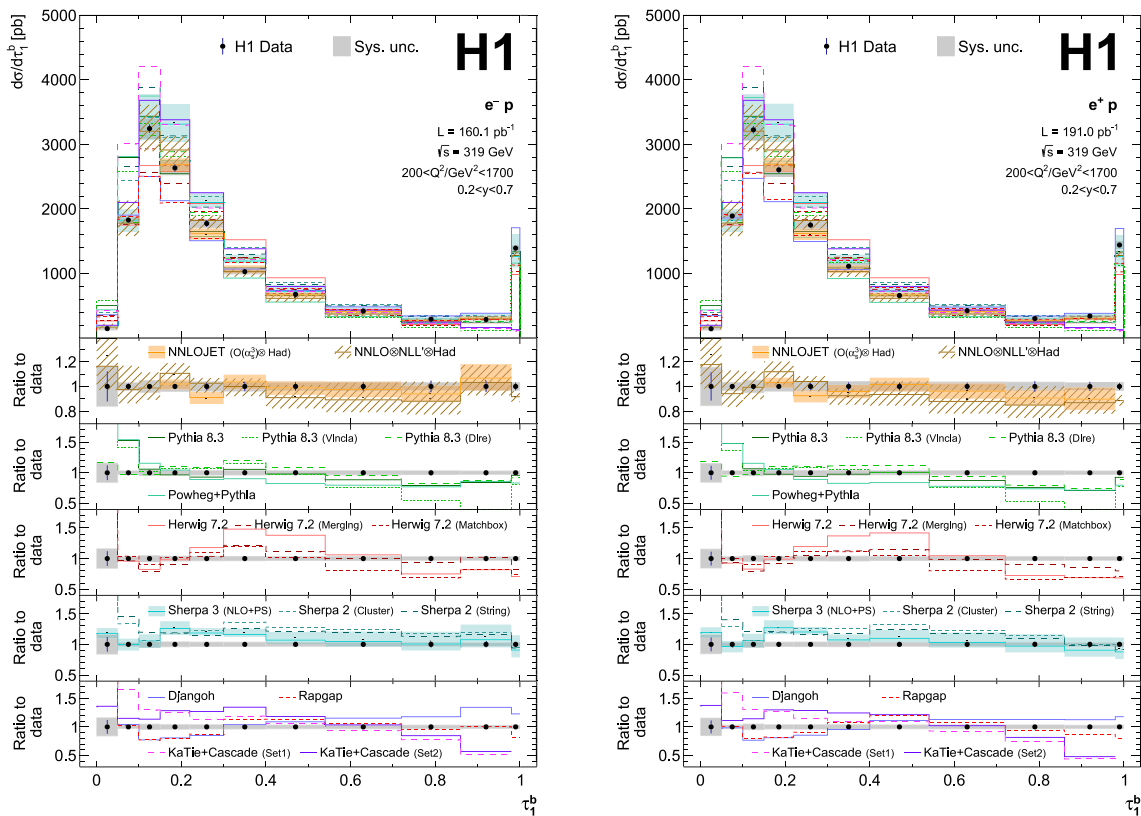
Fig. 6 The differential cross section $d\sigma/d\tau_1^b$ in the kinematic region $200 \leq Q^2/\,\mathrm{GeV}^2 < 1700$ and $0.2 \leq y < 0.7$ for $e^- p$ scattering at $\sqrt{s} = 319\,\mathrm{GeV}$. The data are recorded with electron and positron beams, and corrected to $e^- p$ cross sections using Heracles. Further details are given in the caption of Fig. 5
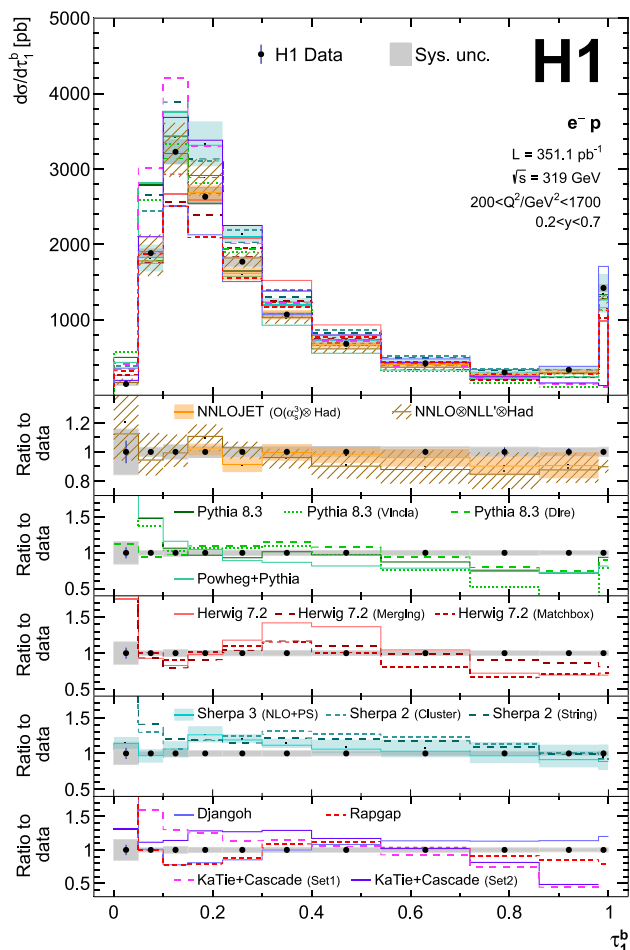
Table 2 Single differential 1-jettiness cross sections for $e^- p$ scattering in the range $200 < Q^2 < 1700\,\mathrm{GeV}^2$ and $0.2 < y < 0.7$, $d\sigma/d\tau_1^b$ [pb/$\Delta\tau_1^b$]. The τ_1^b ranges and the corresponding cross section measurements are indicated, together with the data statistical uncertainty (stat), and the systematic uncertainties: the hadronic (RCES and JES) and electron (ElEn) energy scale uncertainties, the hadron (HadTh) and electron (ElTh) polar angle uncertainties, the model uncertainty (Model), the simulation statistical uncertainty (MCstat), the unfolding uncertainty (Unfold), the electron identification uncertainty (ElecID), the luminosity uncertainty (Lumi), the residual uncorrelated uncertainty (Uncor), and the QED correction uncertainty (QED). The radiative correction factors are also shown

1D 1-jettiness cross sections in $e^- p$ for $200 < Q^2 < 1700\,\mathrm{GeV}^2$ and $0.2 < y < 0.7 - d\sigma/d\tau_1^b$ [pb/$\Delta\tau_1^b$]

| τ_1^b range		Results	Uncertainties													Correction factors					
Min	Max	$\frac{d\sigma}{d\tau_1^b}$	Stat	RCES	JES	HadTh	ElEn	ElTh	Model	MCstat	Unfold	ElecID	Lumi	Uncor	QED	c_{QED}	c_{NoZ}	c_{Born}	c_{e+p}	c_{Had}	δ_{Had}
		(pb)	(%)	(%)	(%)	(%)	(%)	(%)	(%)	(%)	(%)	(%)	(%)	(%)	(%)						(%)
0.00	0.05	144.8	12.1	−0.1	+1.6	+0.8	−0.6	+0.2	−15.6	0.5	−1.1	0.2	2.7	0.5	0.3	1.080	0.975	0.912	0.960	0.102	1.1
0.05	0.10	1827	2.4	+0.5	+1.0	+0.3	−0.9	+0.3	−0.3	0.5	+0.1	0.2	2.7	0.5	0.1	1.070	0.981	0.909	0.974	0.769	1.3
0.10	0.15	3245	2.0	−0.1	+0.6	+0.1	−0.4	+0.5	+4.0	0.6	+0.4	0.2	2.7	0.5	0.1	1.066	0.988	0.912	0.984	1.342	6.7
0.15	0.22	2635	2.2	+0.2	+0.1	−0.1	−1.0	+0.6	+2.8	0.6	−0.6	0.2	2.7	0.5	0.1	1.065	0.989	0.913	0.990	1.397	1.1
0.22	0.30	1774	3.0	+0.4	−0.3	−0.2	−0.7	+0.3	+2.5	0.6	−0.3	0.2	2.7	0.5	0.1	1.071	0.988	0.911	0.989	1.307	1.7
0.30	0.40	1028	3.9	+0.8	−0.7	−0.2	−1.0	+0.4	+2.1	0.4	+0.5	0.2	2.7	0.5	0.1	1.071	0.987	0.912	0.989	1.311	4.5
0.40	0.54	675.7	3.4	+1.0	−0.9	−0.2	−1.4	+0.5	+0.7	0.3	+0.1	0.2	2.7	0.5	0.1	1.069	0.989	0.912	0.991	1.303	6.5
0.54	0.72	417.5	3.4	+0.5	−0.9	−0.2	−1.3	+0.5	−1.6	0.2	+0.0	0.2	2.7	0.5	0.1	1.076	0.987	0.909	0.991	1.268	5.1
0.72	0.86	290.1	4.7	+0.0	−0.7	−0.1	−1.0	+0.5	−1.2	0.3	+0.1	0.2	2.7	0.5	0.2	1.075	0.989	0.911	0.992	1.243	2.1
0.86	0.98	285.6	4.5	+0.0	−0.9	+0.1	−0.5	+0.5	−0.4	0.3	+0.0	0.2	2.7	0.5	0.2	1.073	0.992	0.913	0.994	1.340	1.6
0.98	1.00	1392	3.2	−1.5	−0.2	−0.2	+0.0	+0.3	−1.0	0.2	−0.0	0.2	2.7	0.5	0.2	1.076	0.988	0.913	0.991	0.763	1.1

Table 3 Single differential 1-jettiness cross sections for e^+p scattering in the range $200 < Q^2 < 1700\,\text{GeV}^2$ and $0.2 < y < 0.7$, $\mathrm{d}\sigma/\mathrm{d}\tau_1^b\,[\text{pb}/\Delta\tau_1^b]$. Further details are given in the caption of Table 2

1D 1-jettiness cross sections in e^+p for $200 < Q^2 < 1700\,\text{GeV}^2$ and $0.2 < y < 0.7$ – $\mathrm{d}\sigma/\mathrm{d}\tau_1^b\,[\text{pb}/\Delta\tau_1^b]$

τ_1^b range		Results	Uncertainties													Correction factors					
Min	Max	$\frac{\mathrm{d}\sigma}{\mathrm{d}\tau_1^b}$	Stat	RCES	JES	HadTh	ElEn	ElTh	Model	MCstat	Unfold	ElecID	Lumi	Uncor	QED	c_QED	c_NoZ	c_Born	$c_\text{e+p}$	c_Had	δ_Had
		(pb)	(%)	(%)	(%)	(%)	(%)	(%)	(%)	(%)	(%)	(%)	(%)	(%)	(%)						(%)
0.00	0.05	137.5	11.4	+0.2	+1.7	+0.9	−0.8	+0.2	−15.2	0.5	−0.7	0.2	2.7	0.5	0.3	1.077	1.013	0.916	1.000	0.100	1.1
0.05	0.10	1841	2.1	+0.8	+1.1	+0.4	−0.7	+0.5	+0.4	0.4	+0.7	0.2	2.7	0.5	0.1	1.070	1.005	0.916	1.000	0.761	1.1
0.10	0.15	3174	1.8	+0.2	+0.5	−0.1	−0.6	+0.3	+4.1	0.6	−1.0	0.2	2.7	0.5	0.1	1.065	1.001	0.918	1.000	1.336	6.7
0.15	0.22	2580	1.9	+0.0	−0.1	−0.1	−0.5	+0.4	+2.5	0.6	+0.7	0.2	2.7	0.5	0.1	1.067	0.997	0.917	1.000	1.400	1.1
0.22	0.30	1730	2.7	+0.4	−0.2	−0.1	−1.1	+0.6	+2.5	0.5	+0.4	0.2	2.7	0.5	0.1	1.065	0.996	0.921	1.000	1.308	1.9
0.30	0.40	1099	3.3	+0.8	−0.7	−0.2	−1.2	+0.4	+2.1	0.4	−1.5	0.2	2.7	0.5	0.1	1.067	0.995	0.920	1.000	1.311	4.3
0.40	0.54	651.7	3.2	+1.1	−0.9	−0.2	−1.5	+0.5	+0.5	0.3	+0.5	0.2	2.7	0.5	0.1	1.068	0.996	0.919	1.000	1.302	6.7
0.54	0.72	419.5	3.1	+0.6	−0.8	−0.2	−1.2	+0.5	−1.7	0.2	+0.4	0.2	2.7	0.5	0.1	1.072	0.994	0.917	1.000	1.269	5.1
0.72	0.86	298.2	4.3	−0.0	−0.8	−0.1	−1.0	+0.5	−1.8	0.3	+0.1	0.2	2.7	0.5	0.2	1.072	0.994	0.917	1.000	1.243	2.2
0.86	0.98	337.4	3.7	+0.1	−0.9	−0.0	−0.5	+0.4	−0.9	0.3	−0.0	0.2	2.7	0.5	0.2	1.071	0.995	0.919	1.000	1.340	1.6
0.98	1.00	1428	2.9	−1.4	−0.2	−0.1	+0.1	+0.4	−1.4	0.2	−0.0	0.2	2.7	0.5	0.2	1.075	0.995	0.922	1.000	0.762	1.1

Table 4 Single differential 1-jettiness cross sections for e^-p ($\mathcal{L} = 351.1\,\text{pb}^{-1}$) scattering in the range $200 < Q^2 < 1700\,\text{GeV}^2$ and $0.2 < y < 0.7$, $\mathrm{d}\sigma/\mathrm{d}\tau_1^b\,[\text{pb}/\Delta\tau_1^b]$. Further details are given in the caption of Table 2

1D 1-jettiness cross sections in e^-p ($\mathcal{L} = 351.1\,\text{pb}^{-1}$) for $200 < Q^2 < 1700\,\text{GeV}^2$ and $0.2 < y < 0.7$ – $\mathrm{d}\sigma/\mathrm{d}\tau_1^b\,[\text{pb}/\Delta\tau_1^b]$

τ_1^b range		Results	Uncertainties													Correction factors					
Min	Max	$\frac{\mathrm{d}\sigma}{\mathrm{d}\tau_1^b}$	Stat	RCES	JES	HadTh	ElEn	ElTh	Model	MCstat	Unfold	ElecID	Lumi	Uncor	QED	c_QED	c_NoZ	c_Born	$c_\text{e+p}$	c_Had	δ_Had
		(pb)	(%)	(%)	(%)	(%)	(%)	(%)	(%)	(%)	(%)	(%)	(%)	(%)	(%)						(%)
0.00	0.05	149.8	7.8	+0.0	+1.7	+0.9	−0.6	+0.2	−15.4	0.4	−1.2	0.2	2.7	0.5	0.2	1.101	0.975	0.912	0.960	0.102	1.1
0.05	0.10	1885	1.5	+0.7	+1.1	+0.3	−0.8	+0.4	+0.0	0.3	+0.7	0.2	2.7	0.5	0.1	1.084	0.981	0.909	0.974	0.769	1.3
0.10	0.15	3227	1.2	+0.1	+0.5	−0.0	−0.6	+0.4	+4.0	0.4	−0.8	0.2	2.7	0.5	0.1	1.073	0.988	0.912	0.984	1.342	6.7
0.15	0.22	2632	1.2	+0.1	−0.0	−0.1	−0.8	+0.4	+2.7	0.4	+0.5	0.2	2.7	0.5	0.1	1.070	0.989	0.913	0.990	1.397	1.1
0.22	0.30	1770	1.7	+0.4	−0.2	−0.1	−0.9	+0.5	+2.5	0.3	−0.1	0.2	2.7	0.5	0.1	1.072	0.988	0.911	0.989	1.307	1.7
0.30	0.40	1070	2.3	+0.8	−0.7	−0.2	−1.1	+0.5	+2.2	0.3	−0.6	0.2	2.7	0.5	0.1	1.073	0.987	0.912	0.989	1.311	4.5
0.40	0.54	681.3	2.2	+1.1	−0.9	−0.2	−1.5	+0.6	+0.6	0.2	+0.3	0.2	2.7	0.5	0.1	1.072	0.989	0.912	0.991	1.303	6.5
0.54	0.72	423.8	2.3	+0.5	−0.9	−0.2	−1.3	+0.5	−1.6	0.2	+0.2	0.2	2.7	0.5	0.1	1.077	0.987	0.909	0.991	1.268	5.1
0.72	0.86	302	3.1	+0.0	−0.8	−0.2	−1.0	+0.5	−1.4	0.2	+0.1	0.2	2.7	0.5	0.1	1.076	0.989	0.911	0.992	1.243	2.1
0.86	0.98	336.7	2.7	+0.1	−0.9	+0.0	−0.5	+0.5	−0.5	0.2	−0.0	0.2	2.7	0.5	0.1	1.074	0.992	0.913	0.994	1.340	1.6
0.98	1.00	1422	2.2	−1.4	−0.2	−0.2	+0.1	+0.3	−1.1	0.1	−0.0	0.2	2.7	0.5	0.1	1.079	0.988	0.913	0.991	0.763	1.1

6, 7, 8, 9, 10, 11, 12, 13, 14, 15, 16, 17, 18, 19, 20, 21, 22, 23, 24, 25, 26, 27, 28, 29, 30, 31, 32, 33, 34, 35 and 36 and are displayed in Fig. 7. The ratio of the data and predictions to the predictions from Sherpa 3.0 are displayed in Figs. 8, 9, 10, 11 and 12. The triple differential cross sections are presented in the kinematic range $150 < Q^2 < 20{,}000\,\text{GeV}^2$ and $0.05 < y < 0.94$ as a function of τ_1^b. Regions that are kinematically forbidden or experimentally inaccessible are omitted. At highest Q^2 only a single combined y region ($0.2 < y < 0.94$) is presented due to low event counts.

Events with a harder virtuality Q produce more collimated particles, effectively shifting the DIS peak position in the τ_1^b distributions towards lower values. In addition, a reduced phase space for hard radiation at high Q^2 tends to lower the differential cross section in the larger τ_1^b region relative to the peak region. The relative contribution of topologies with τ_1^b close to unity increases with y for fixed Q. Equivalently, that contribution increases as x_{Bj} decreases.

Comparison to exact QCD predictions The fixed order predictions with NLL resummation of large logarithms (NNLO⊗NLL′⊗Had) provide an accurate description of the entire τ_1^b distribution within their uncertainties with the exception of some of the lowest τ_1^b bins of the triple-differential distributions. These predictions include resummation and are matched to the NNLO inclusive DIS cross
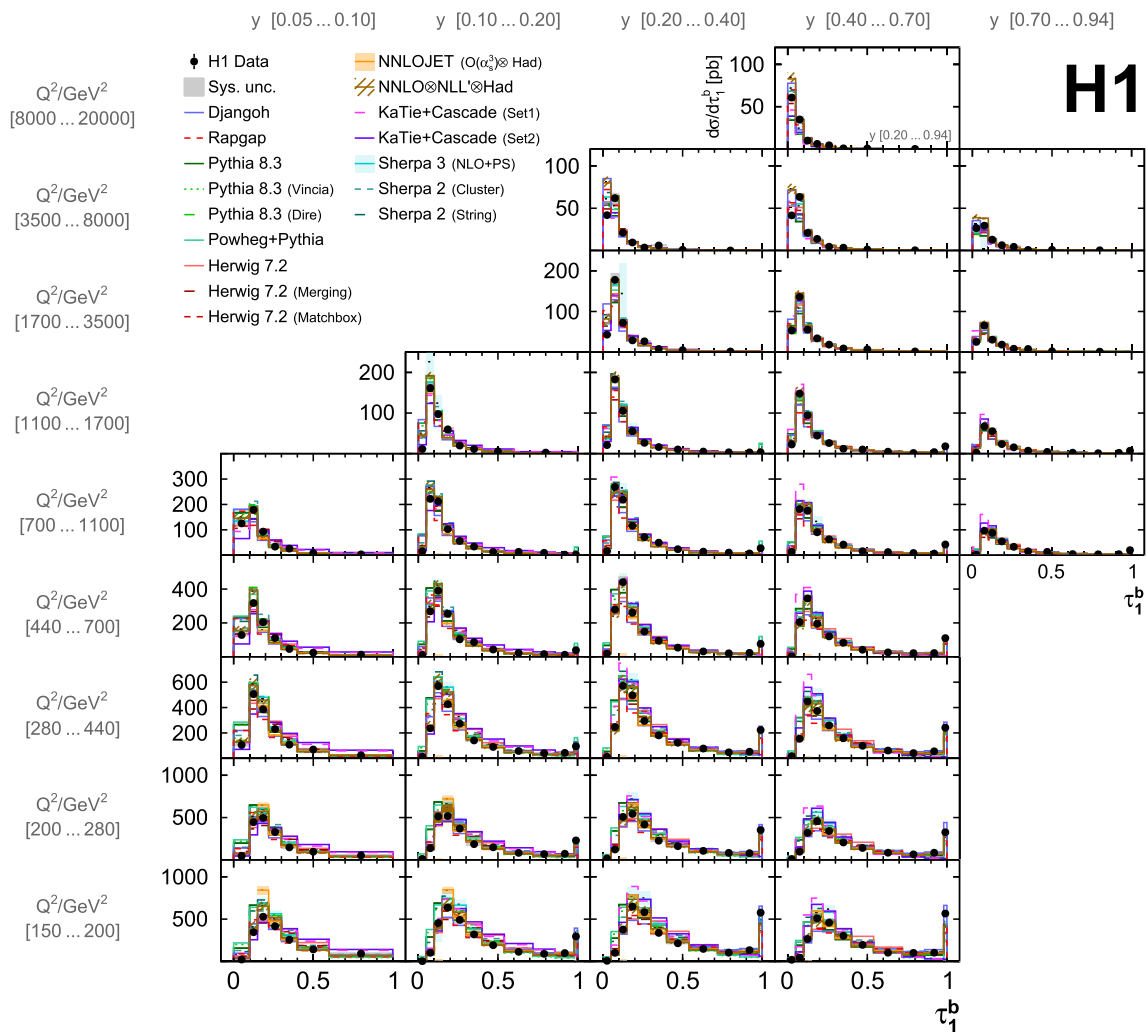
Fig. 7 The triple-differential cross section $\frac{d^3\sigma}{d\tau_1^b dQ^2 dy}$, presented as $\frac{d\sigma}{d\tau_1^b}$ in regions of Q^2 and y. The Q^2 and y ranges are displayed on the left and top, respectively. Each panel displays the differential cross section $d\sigma/d\tau_1^b$ in that phase space. The data are displayed as full circles, the vertical error bars indicate statistical uncertainties, while systematic uncertainties are displayed as shaded area. The data are compared to predictions from NNLOJET, NNLO⊗NLL′⊗Had, Pythia 8.3,Powheg

Box, Herwig 7.2, Sherpa 2.2, Sherpa 3.0, Djangoh, Rapgap, and KaTie+Cascade 3. Selected parameters are varied in the predictions as indicated. The ratios of the data and predictions to the Sherpa 3.0 predictions are displayed in Figs. 8, 9, 10, 11 and 12. At highest Q^2 ($8000 < Q^2/\text{GeV}^2 < 20\,000$) only a single y interval is measured, $0.2 < y < 0.94$

section (α_s^2), such that they are valid over the entire τ_1^b range. Formally, they are one order lower in α_s than the NNLOJET predictions.

The NNLO-dijet predictions from NNLOJET (α_s^3) provide a good description of the data within their uncertainty over their entire range of validity ($0.22 < \tau_1^b < 0.98$). Sizable hadronization corrections of up to +40% hinder quantitative comparisons and an interpretation in terms of underlying parameters of the theory; this point will have to be investigated in the future.

Comparison to recent MC event generators The recent MC event generators Pythia 8.3, Powheg+Pythia, Herwig 7.2,

Sherpa 2.2 and Sherpa 3.0 employ LO, multi-leg or NLO matrix elements matched to parton shower and hadronization models. Those generators generally provide a good description of the data.

The MC predictions from Pythia provide an overall reasonable description of the data, with small but visible differences between the three parton shower models studied. The default Pythia and Pythia+Vincia predictions overestimate the data at low $\tau_1^b < 0.1$, whereas Pythia+Dire provides a better though not perfect description. All three Pythia predictions are similar in the parton-shower region ($0.1 < \tau_1^b < 0.4$), but tend to underestimate the data in the tail region ($\tau_1^b > 0.5$). The latter could be related to the fact
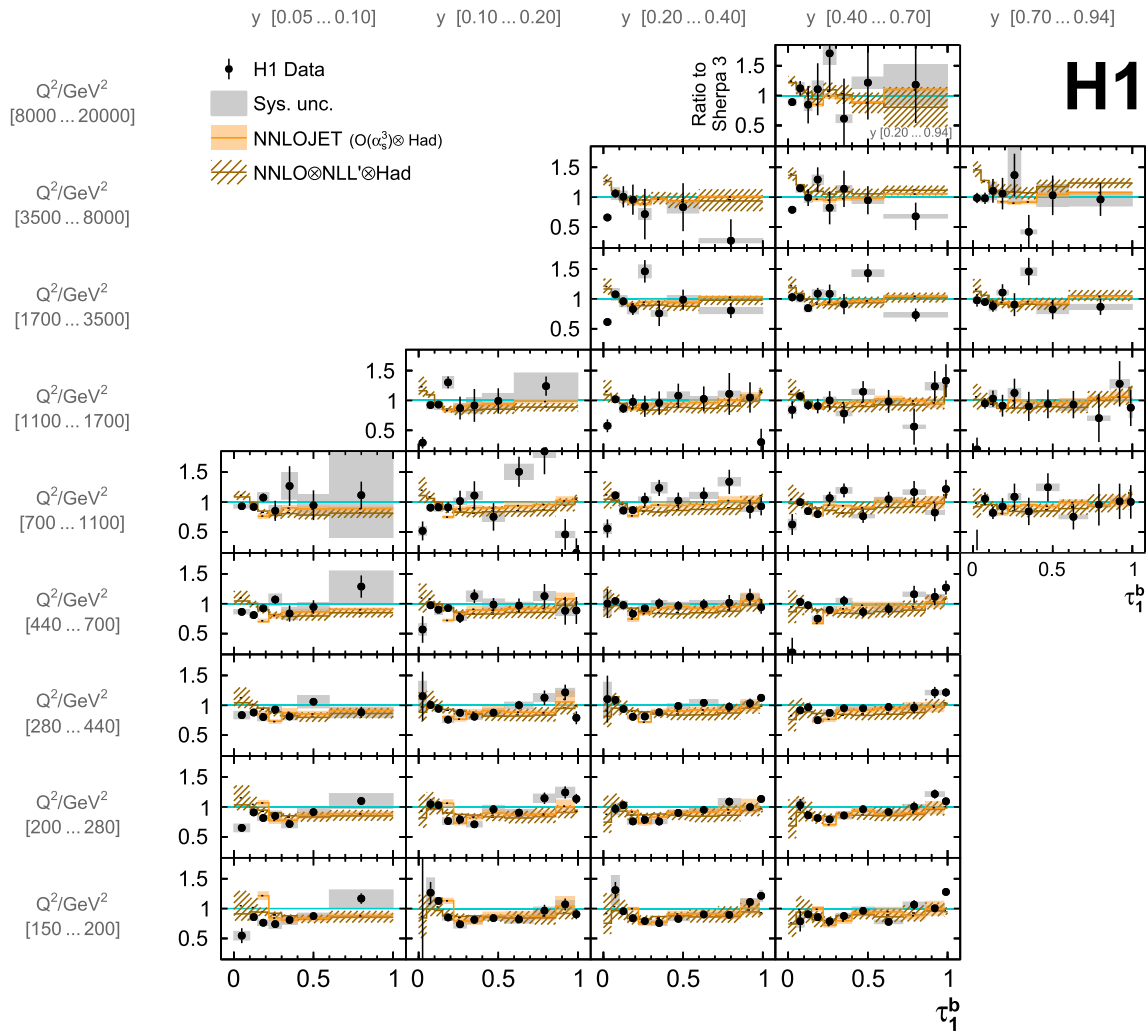
Fig. 8 The ratio of data and NNLOJET ($\mathcal{O}(\alpha_s^3)$) and NNLO⊗NLL′⊗Had predictions to the Sherpa 3.0 predictions for the triple-differential cross section $\frac{d^3\sigma}{d\tau_1^b dQ^2 dy}$. See Fig. 7 caption for further details. The data are displayed as full circles, the vertical error bars indicate statistical uncertainties, while systematic uncer-tainties are displayed as shaded area. The shaded coloured area indicates the theoretical uncertainty associated with the NNLO-dijet predictions by NNLOJET. The hatched area indicates the theoretical uncertainty associated with the NNLO⊗NLL′⊗Had predictions

Table 5 Differential 1-jettiness cross sections for $e^- p$ ($\mathcal{L} = 351.1\,\mathrm{pb}^{-1}$) scattering in the range $150 < Q^2 < 200\,\mathrm{GeV}^2$ and $0.05 < y < 0.10$, $d\sigma/d\tau_1^b$ [pb/$\Delta\tau_1^b$]. Further details are given in the caption of Table 2

Cross sections in $e^- p$ ($\mathcal{L} = 351.1\,\mathrm{pb}^{-1}$) for $150 < Q^2 < 200\,\mathrm{GeV}^2$ and $0.05 < y < 0.10 - d\sigma/d\tau_1^b$ [pb/$\Delta\tau_1^b$]

τ_1^b range		Results	Uncertainties												Correction factors					
Min	Max	$\frac{d\sigma}{d\tau_1^b}$	Stat	RCES	JES	HadTh	ElEn	ElTh	Model	MCstat	Unfold	ElecID	Lumi	Uncor	QED	c_{QED}	c_{NoZ}	c_{Born}	c_{e+p}	c_{Had}	δ_{Had}
		(pb)	(%)	(%)	(%)	(%)	(%)	(%)	(%)	(%)	(%)	(%)	(%)	(%)	(%)						(%)
0.00	0.10	22.81	22.8	+2.7	+1.8	+2.2	+4.4	+0.8	−11.0	2.3	+1.5	0.2	2.7	0.5	0.8	1.063	1.010	0.918	0.992	0.144	1.6
0.10	0.15	345.4	4.0	+2.7	+1.1	+1.1	+3.7	+0.9	−2.9	1.3	+0.4	0.2	2.7	0.5	0.5	1.072	0.996	0.925	1.001	1.068	4.5
0.15	0.22	528.3	2.5	+1.6	+0.4	+0.2	+3.0	+0.9	+4.0	0.9	+0.7	0.2	2.7	0.5	0.4	1.065	1.001	0.922	1.002	2.035	31.9
0.22	0.30	416.3	3.7	+1.4	+0.1	+0.4	+4.6	+1.9	+7.6	1.7	−3.1	0.2	2.7	0.5	0.4	1.068	0.997	0.919	0.995	1.847	12.4
0.30	0.40	256.7	6.0	+4.0	+0.8	+1.2	+3.2	+2.1	+6.4	2.7	−1.1	0.2	2.7	0.5	0.4	1.066	0.998	0.924	1.001	1.517	3.0
0.40	0.60	141.8	7.2	+2.8	−0.0	+0.6	+3.6	+1.1	−1.5	1.6	+1.0	0.2	2.7	0.5	0.3	1.065	1.003	0.925	1.004	1.456	6.1
0.60	1.00	92.52	7.5	+1.0	+1.2	+1.7	+4.8	+1.1	−10.7	1.5	+1.2	0.2	2.7	0.5	0.2	1.073	0.992	0.920	0.997	1.224	1.9

Fig. 9 The ratio of data and Pythia 8.3 predictions to the Sherpa 3.0 predictions for the triple-differential cross section $\frac{d^3\sigma}{d\tau_1^b dQ^2 dy}$. See Fig. 7 caption for further details. The data are displayed as full circles, the vertical error bars indicate statistical uncertainties, while systematic uncertainties are displayed as shaded area. The full dark green line indi- cates predictions from Pythia 8.3 employing the default parton shower adapted for DIS kinematics, the short dashed line indices predictions using the Vincia parton shower, and the long dashed line the Dire parton shower. The green full line shows predictions from Powheg Box interfaced to parton shower and hadronization from Pythia 8.3

that matrix elements for $eg \rightarrow eq\bar{q}$ enter at $\mathcal{O}(\alpha_s)$ only, and are not recovered properly in a parton shower emerging from $eq \rightarrow eq$ alone. The default Pythia predictions are a leading-order MC model and they benefit from a large value of $\alpha_s(m_Z)$ for the parton shower, which is default in Pythia, and thus raises the prediction at larger τ_1^b and brings them closer to the data. Looking only at the single-differential cross sections, Pythia+Dire tends to overshoot the data in the parton-shower region, but from the triple-differential data it is evident that the discrepancy arises from events at lower values of Q^2. At very large values of y ($y > 0.7$), the Pythia+Dire predictions fail to describe the data at large values of τ_1^b. The Pythia+Vincia prediction provides a good description of the data in the range $0.1 \lesssim \tau_1^b \lesssim 0.5$. It has difficulties at larger

values of τ_1^b, presumably related to the fact that Vincia was developed for a symmetric collider setup and is not yet fully validated for the asymmetric beams of ep collisions.

The predictions from Powheg Box are lower than the default Pythia predictions at medium to large τ_1^b, and over-shoot the data at low τ_1^b. Larger values of $\alpha_s(m_Z)$ in the simulation, or corrections beyond NLO DIS, such as NLO dijet matrix elements, may be required to improve the description of the data.

The Herwig variants are able to provide a good description of the data. Although the default predictions from Herwig 7.2 provide the worst description among all recent MC generators, a significant improvement is obtained with NLO matrix elements. The merging technique provides the best descrip-
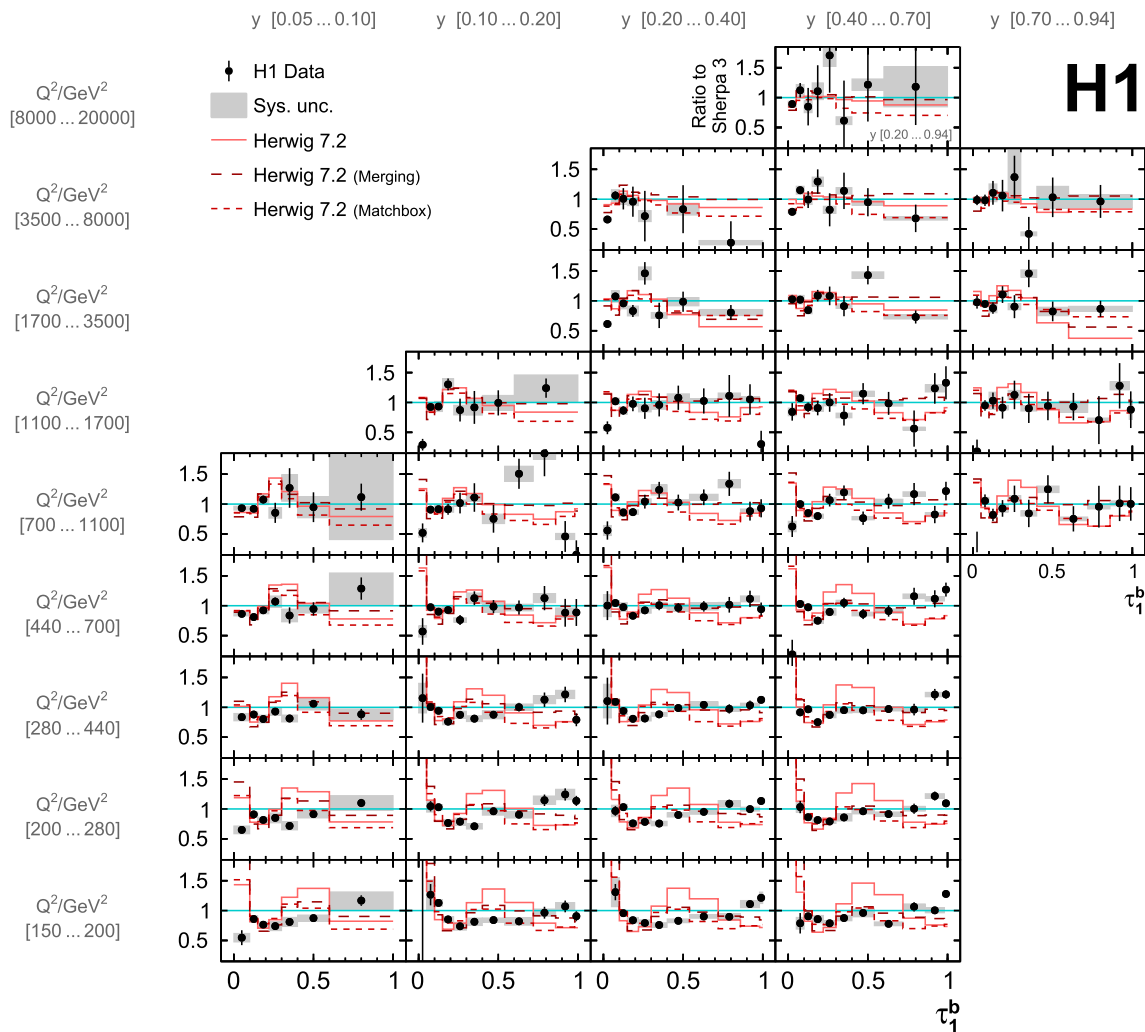
Fig. 10 The ratio of data and Herwig 7.2 predictions to the Sherpa 3.0 predictions for the triple-differential cross section $\frac{d^3\sigma}{d\tau_1^b dQ^2 dy}$. See Fig. 7 caption for further details. The data are displayed as full circles, the vertical error bars indicate statistical uncertainties, while systematic uncertainties are displayed as shaded area. The full line indicates predictions from Sherpa 3.0, and the shaded coloured are associated theoretical uncertainties. The short and long dashed lines indicate predictions from Sherpa 2.2, where two hadronisation models are studies, Cluster and String hadronisation model, respectively

tion among the Herwig predictions, with benefits particularly at larger τ_1^b. All Herwig predictions fail to describe the lowest τ_1^b cross section ($\tau_1^b < 0.05$). The default Herwig predictions exhibit a prominent structure at medium τ_1^b.

The Sherpa 2.2 predictions provide a good description of the data, in particular at larger τ_1^b. The two different hadronization models (String vs. Cluster) provide very similar predictions, which do not differ by more than the data uncertainties, albeit the string model is a bit closer to the data at medium τ_1^b. Both Sherpa 2.2 predictions overshoot the data at lowest τ_1^b ($\tau_1^b < 0.1$), and undershoot the data at $\tau_1^b \simeq 1$. The underprediction at high τ_1^b and overprediction at low τ_1^b seems to be a common feature of NLO+PS models, c.f. Powheg Box and Herwig.

The Sherpa 3.0 predictions with NLO matrix elements, improved parton shower and cluster hadronization model provide a better description of the data than those from Sherpa 2.2, and the predictions provide an accurate description of the data within the uncertainties. Only at lower Q^2 and values of $\tau_1^b \sim 0.3$ the Sherpa 3.0 predictions overestimate the data. A noteworthy improvement over other MC predictions is observed in the lowest τ_1^b region, where also good agreement with data is observed. This could be related to the modeling of an intrisic k_t in Sherpa 3.0.

Comparison to MC event generators from the HERA era and dedicated DIS models The DIS MC event generators Djangoh and Rapgap provide an overall satisfactory description of the data, although both have difficulties to describe the shape in the region $\tau_1^b < 0.3$ accurately and both models underesti-
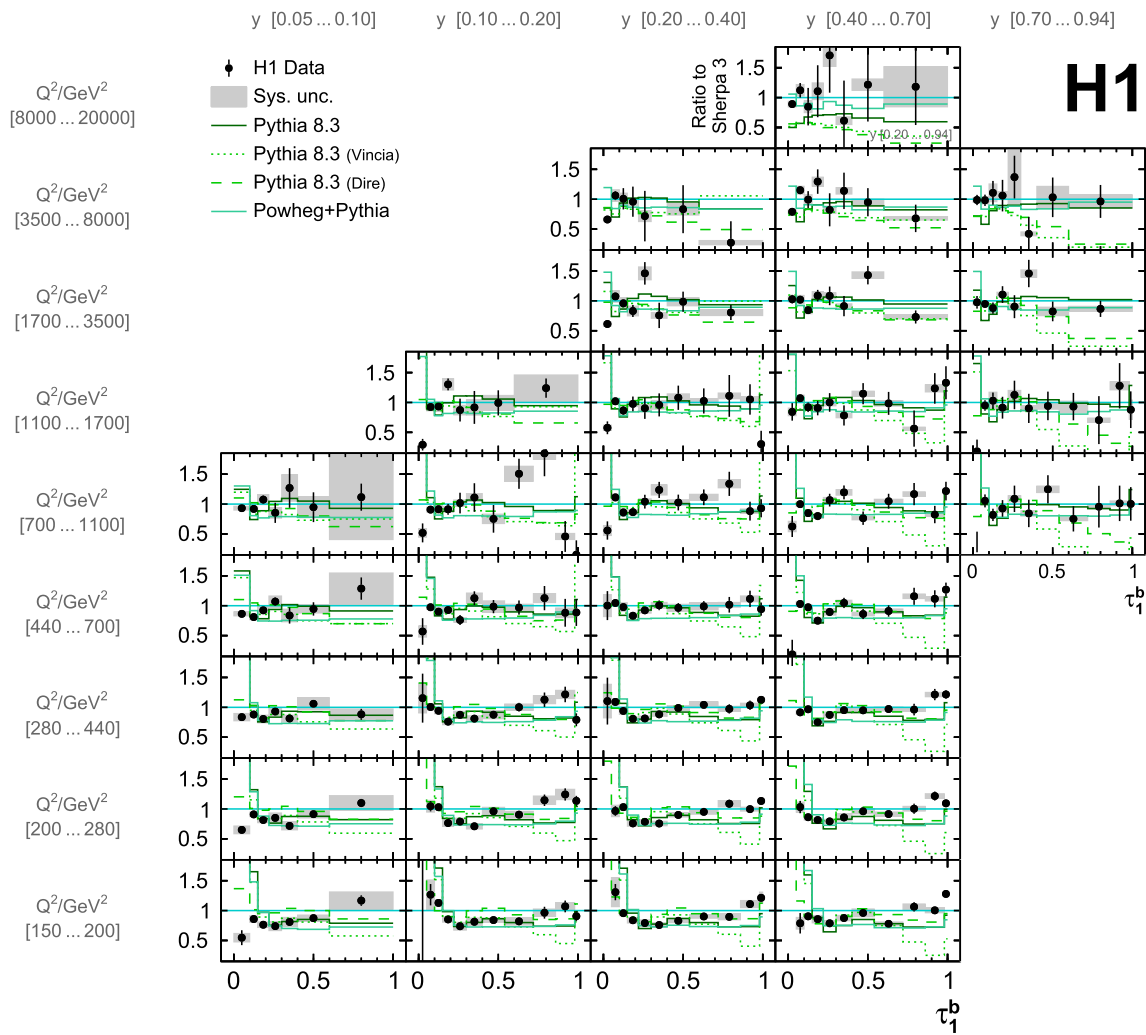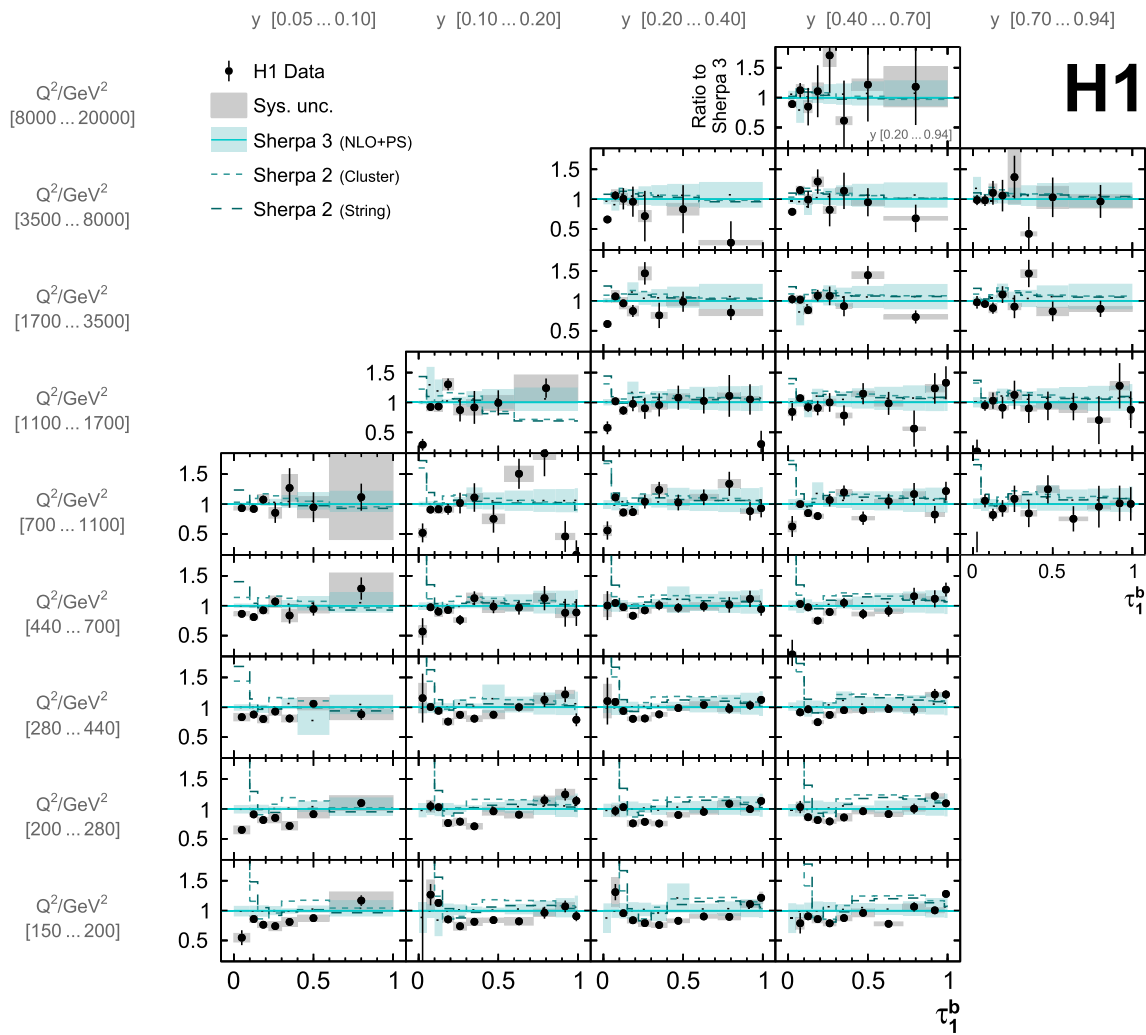
Fig. 11 The ratio of data and Sherpa 2 predictions to Sherpa 3.0 predictions for the triple-differential cross section $\frac{d^3\sigma}{d\tau_1^b dQ^2 dy}$. See Fig. 7 caption for further details. The data are displayed as full circles, the vertical error bars indicate statistical uncertainties, while systematic uncertainties are displayed as shaded area. The full dark green line indicates predictions from Pythia 8.3 employing the default parton shower adapted for DIS kinematics, the short dashed line indices predictions using the Vincia parton shower, and the long dashed line the Dire parton shower. The green full line shows predictions from Powheg Box interfaced to parton shower and hadronization from Pythia 8.3

mate the data in the range $0.1 < \tau_1^b < 0.3$. The high τ_1^b region is well described. Djangoh is somewhat higher than Rapgap in that region, which is consistent with the observation of a harder P_T-spectrum of jets [186]. The triple-differential cross sections are well described by Djangoh and Rapgap. At low y, Rapgap underestimates the high τ_1^b region more than Djangoh. Both models fail to describe the region $\tau_1^b < 0.05$.

The KaTie+Cascade 3 predictions, employing TMD-sensitive PDF sets with two different choices for the QCD evolution scale, provide a reasonable description of the data. TMD PDF Set 2 provides one of the best descriptions at the low τ_1^b region, whereas the predictions with TMD PDF Set 1 are a bit higher. However, at lowest Q^2 and large y, also predictions from Set 2 overshoot the data significantly. In the region of larger τ_1^b, the KaTie+Cascade 3 predictions fail to

describe the data, likely related to the absence of $eg \rightarrow eq\bar{(q)}$ processes in the hard matrix elements.

Double-differential cross sections for inclusive neutral-current DIS as a function of Q^2 and y The inclusive NC DIS cross sections $\frac{d^2\sigma_{NC\,DIS}}{dQ^2 dy}$ are presented in Tables 37 and 38 and are displayed in Fig. 13, where NNLO and aN3LO predictions for inclusive DIS are compared with the data. For comparisons with the NC DIS predictions, the data are corrected to the DIS Born level by applying the factor c_{Born}. These cross sections are measured for $e^+ p$ and $e^- p$ scattering by analyzing the data from the two lepton charges separately, including dedicated unfolding matrices and QED correction factors. The inclusive NC DIS cross sections $\frac{d^2\sigma_{NC\,DIS}}{dQ^2 dy}$ are obtained by integrating over τ_1^b in every (Q^2, y) range.
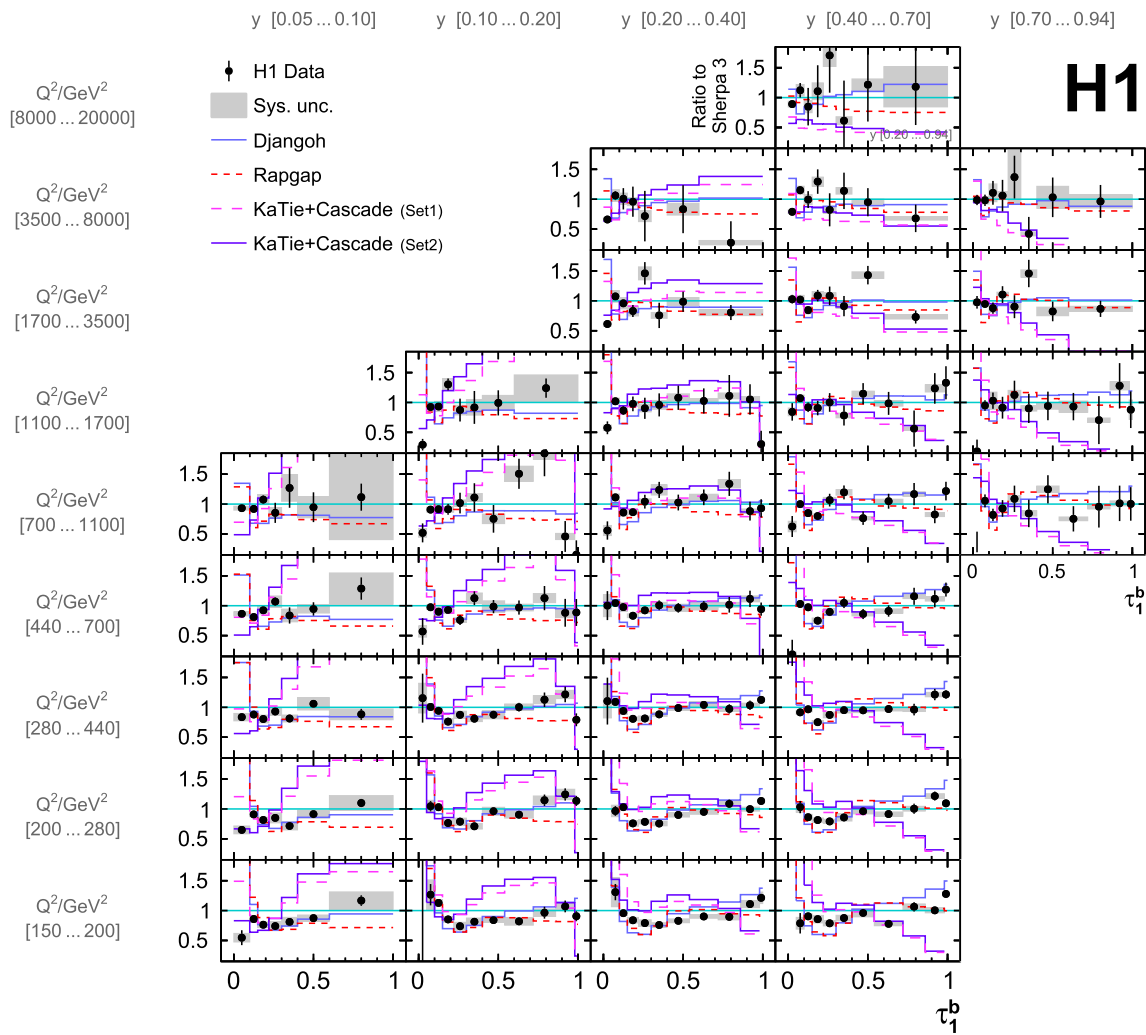
Fig. 12 The ratio of data and predictions from dedicated DIS MC event generators to the Sherpa 3.0 predictions for the triple-differential cross section $\frac{d^3\sigma}{d\tau_1^b dQ^2 dy}$ for adjacent regions in Q^2 and y. See Fig. 7 caption for further details. The data are displayed as full circles, the vertical error bars indicate statistical uncertainties, while systematic uncertainties are displayed as shaded area. The full blue line indicates predictions from Djangoh, the red dashed line from Rapgap, and the pink dashed and violet line line show predictions from KaTie+Cascade 3 for two different TMD PDFs and scale choices

Hence, kinematic migrations due to limited resolution of the detector are corrected with high accuracy, since different configurations of the hadronic final state, represented by τ_1^b, are considered in the unfolding. The inclusive NC DIS cross sections can be compared with predictions from structure function calculations, and serve as an important validation of the absolute size of the τ_1^b cross sections. These data constitute the first bin integrated inclusive NC DIS cross section measurements at HERA in Q^2 and y, employing proper regularized unfolding of detector effects. The results can be compared with predictions based on structure functions and serve as a crosscheck in the determination of the absolute normalization of the triple-differential cross section measurements. The NC DIS measurements are also used together with

the triple-differential cross sections to obtain normalized 1-jettiness event shape distributions [180].

Predictions for inclusive NC DIS cross sections The double-differential inclusive DIS $\frac{d^2\sigma_{NC\ DIS}}{dQ^2 dy}$ are compared to predictions in NNLO and a3NLO accuracy. It is observed that both the NNLO and the a3NLO predictions provide a very good description of the $e^+ p$ and $e^- p$ data in the entire kinematic range, and small discrepancies are observed only at lowest values of y or largest values of Q^2. One can note that the H1 data [74, 187] are already included in the PDF determination, which is the basis of the predictions. Differences between the H1PDF2017NNLO PDF set and the NNPDF3.1 PDF set are small.

Table 6 Differential 1-jettiness cross sections for e^-p ($\mathcal{L} = 351.1\,\mathrm{pb}^{-1}$) scattering in the range $150 < Q^2 < 200\,\mathrm{GeV}^2$ and $0.10 < y < 0.20$, $d\sigma/d\tau_1^b$ [pb/$\Delta\tau_1^b$]. Further details are given in the caption of Table 2

τ_1^b range		Results	Uncertainties													Correction factors					
Min	Max	$\frac{d\sigma}{d\tau_1^b}$	Stat	RCES	JES	HadTh	ElEn	ElTh	Model	MCstat	Unfold	ElecID	Lumi	Uncor	QED	c_{QED}	c_{NoZ}	c_{Born}	$c_{\mathrm{e+p}}$	c_{Had}	δ_{Had}
		(pb)	(%)	(%)	(%)	(%)	(%)	(%)	(%)	(%)	(%)	(%)	(%)	(%)	(%)						(%)
0.00	0.05	3.299	153.8	−3.4	+2.9	+1.9	+0.1	+0.9	−38.8	10.6	−2.5	0.2	2.7	0.5	2.3	1.107	1.010	0.967	0.990	0.019	0.2
0.05	0.10	102.2	14.1	+1.6	+1.5	+1.4	+4.3	−1.1	−18.5	2.6	+1.1	0.2	2.7	0.5	0.7	1.079	0.994	0.904	0.985	0.248	5.2
0.10	0.15	454.1	4.6	+2.4	+1.6	+0.7	+0.3	+1.0	+0.0	2.0	−0.8	0.2	2.7	0.5	0.4	1.077	0.986	0.914	1.000	0.869	3.0
0.15	0.22	636.8	2.9	+0.9	+0.6	+0.3	+2.3	+0.2	+3.7	1.4	−0.1	0.2	2.7	0.5	0.3	1.072	0.995	0.921	0.997	1.665	22.6
0.22	0.30	491.1	4.2	+1.6	−0.3	−0.2	+2.2	+1.5	+7.6	1.9	+1.0	0.2	2.7	0.5	0.3	1.075	0.991	0.918	0.990	1.621	7.6
0.30	0.40	318.8	5.9	+2.3	+0.2	+0.0	+1.7	+0.3	+6.1	1.8	−1.9	0.2	2.7	0.5	0.3	1.069	0.996	0.919	1.001	1.420	1.0
0.40	0.54	191.9	6.9	+2.0	+0.3	+0.2	+1.3	+1.4	+0.7	1.3	+0.0	0.2	2.7	0.5	0.3	1.069	0.996	0.923	1.001	1.420	6.7
0.54	0.72	114	7.8	+1.4	+0.6	+0.3	+1.4	+1.0	−6.8	1.0	+1.2	0.2	2.7	0.5	0.3	1.074	0.999	0.915	0.998	1.396	6.3
0.72	0.86	90.26	10.3	+0.5	+0.3	−0.1	+1.4	+1.4	−5.3	1.2	+0.6	0.2	2.7	0.5	0.3	1.079	0.993	0.917	0.997	1.355	2.9
0.86	0.98	98.86	9.2	+0.3	−0.1	−0.1	+2.3	+1.0	−4.6	1.1	−0.1	0.2	2.7	0.5	0.3	1.069	1.000	0.929	1.003	1.451	2.7
0.98	1.00	295.5	9.2	−1.0	−0.6	−0.4	+2.7	+0.4	−4.3	0.8	−0.0	0.2	2.7	0.5	0.3	1.075	0.997	0.921	0.998	0.679	1.7

Table 7 Differential 1-jettiness cross sections for e^-p ($\mathcal{L} = 351.1\,\mathrm{pb}^{-1}$) scattering in the range $150 < Q^2 < 200\,\mathrm{GeV}^2$ and $0.20 < y < 0.40$, $d\sigma/d\tau_1^b$ [pb/$\Delta\tau_1^b$]. Further details are given in the caption of Table 2

τ_1^b range		Results	Uncertainties													Correction factors					
Min	Max	$\frac{d\sigma}{d\tau_1^b}$	Stat	RCES	JES	HadTh	ElEn	ElTh	Model	MCstat	Unfold	ElecID	Lumi	Uncor	QED	c_{QED}	c_{NoZ}	c_{Born}	$c_{\mathrm{e+p}}$	c_{Had}	δ_{Had}
		(pb)	(%)	(%)	(%)	(%)	(%)	(%)	(%)	(%)	(%)	(%)	(%)	(%)	(%)						(%)
0.00	0.05	7.584	48.1	−0.6	+1.1	+1.0	+1.3	+0.6	−34.2	7.2	+6.3	0.2	2.7	0.5	1.9	1.047	1.015	0.954	0.979	0.018	0.2
0.05	0.10	101.9	10.4	+1.3	+1.6	+0.2	−1.7	−0.2	−18.1	2.4	+0.5	0.2	2.7	0.5	0.6	1.085	0.994	0.911	0.980	0.209	3.4
0.10	0.15	376.1	4.5	+1.3	+2.3	+1.0	+0.5	+0.7	+0.2	1.7	−0.5	0.2	2.7	0.5	0.3	1.067	1.002	0.926	0.998	0.714	1.6
0.15	0.22	647.2	2.5	+1.1	+0.3	−0.1	+0.3	+0.3	+4.6	1.1	+0.2	0.2	2.7	0.5	0.2	1.072	0.996	0.920	0.998	1.402	13.4
0.22	0.30	581.7	3.0	+0.8	−0.0	−0.4	−1.2	+0.8	+6.1	1.1	−0.3	0.2	2.7	0.5	0.2	1.081	0.991	0.914	0.995	1.447	1.1
0.30	0.40	337.6	4.7	+1.0	+0.4	+0.2	−0.1	+0.8	+4.0	0.9	+0.2	0.2	2.7	0.5	0.2	1.073	1.000	0.917	0.990	1.341	0.8
0.40	0.54	214.6	4.8	+1.3	+0.3	+0.0	−0.5	+0.8	+2.1	0.6	+0.3	0.2	2.7	0.5	0.2	1.065	0.997	0.920	1.003	1.379	6.4
0.54	0.72	148.1	4.7	+0.9	−0.2	−0.2	−1.0	+0.7	−1.0	0.5	−0.3	0.2	2.7	0.5	0.2	1.074	0.995	0.917	0.995	1.375	7.4
0.72	0.86	103.6	6.6	+0.2	−0.2	−0.0	−0.4	+0.8	−4.8	0.6	−0.1	0.2	2.7	0.5	0.2	1.073	0.997	0.916	0.999	1.349	4.0
0.86	0.98	133.4	5.1	+0.2	−0.5	−0.0	+0.3	+0.7	−4.6	0.5	−0.0	0.2	2.7	0.5	0.2	1.079	0.992	0.918	0.994	1.461	3.2
0.98	1.00	576.5	3.8	−1.1	−0.3	−0.2	+1.4	+0.5	−7.2	0.3	−0.0	0.2	2.7	0.5	0.2	1.079	0.996	0.915	0.995	0.707	1.8

7 Summary

The first measurement of the 1-jettiness event shape observable in neutral-current deep-inelastic electron–proton scattering is presented. The measured 1-jettiness observable τ_1^b is equivalent to the classical event shape observable Thrust normalized with $\frac{Q}{2}$, τ_{zQ}. It quantities the degree to which the hadronic final state in the current hemisphere is collimated along the exchanged bosons four-vector.

The data were recorded with the H1 experiment at the HERA collider operating with a center-of-mass energy of $\sqrt{s} = 319\,\mathrm{GeV}$. A single-differential cross section is measured as a function of τ_1^b in the kinematic region $200 \leq Q^2 < 1700\,\mathrm{GeV}^2$ and $0.2 \leq y < 0.7$. A triple-differential cross section as a function of τ_1^b, Q^2, and y is reported in the kinematic range $0 \leq \tau_1^b \leq 1$, $150 \leq Q^2 < 20\,000\,\mathrm{GeV}^2$, and $0.05 \leq y < 0.94$. The data are unfolded to the particle level and corrected for higher-order QED radiative effects.

Given typical accuracies of 4–20% (single differential) and 6–30% (triple-differentials), the data are discriminary to the modeling of the hard interaction, as well as to the parton shower and hadronization models in MC event generators. The unfolded data are compared to a variety of predictions. Most of the models studied provide a satisfactory description

Table 8 Differential 1-jettiness cross sections for $e^- p$ ($\mathcal{L} = 351.1\,\mathrm{pb}^{-1}$) scattering in the range $150 < Q^2 < 200\,\mathrm{GeV}^2$ and $0.40 < y < 0.70$, $\mathrm{d}\sigma/\mathrm{d}\tau_1^b$ [pb/$\Delta\tau_1^b$]. Further details are given in the caption of Table 2

Cross sections in $e^- p$ ($\mathcal{L} = 351.1\,\mathrm{pb}^{-1}$) for $150 < Q^2 < 200\,\mathrm{GeV}^2$ and $0.40 < y < 0.70 - \mathrm{d}\sigma/\mathrm{d}\tau_1^b$ [pb/$\Delta\tau_1^b$]

τ_1^b range		Results $\frac{\mathrm{d}\sigma}{\mathrm{d}\tau_1^b}$	Uncertainties													Correction factors					
Min	Max		Stat	RCES	JES	HadTh	ElEn	ElTh	Model	MCstat	Unfold	ElecID	Lumi	Uncor	QED	c_{QED}	c_{NoZ}	c_{Born}	$c_{\mathrm{e+p}}$	c_{Had}	δ_{Had}
		(pb)	(%)	(%)	(%)	(%)	(%)	(%)	(%)	(%)	(%)	(%)	(%)	(%)	(%)						(%)
0.00	0.05	19.92	23.3	+0.4	+2.1	+1.9	+0.5	+0.8	−23.5	8.7	−7.8	0.2	2.7	0.5	1.8	1.111	0.970	0.850	0.933	0.017	0.2
0.05	0.10	45.17	21.7	−2.7	−0.4	+0.3	+1.3	+0.5	−11.3	3.0	−1.6	0.2	2.7	0.5	0.5	1.054	1.012	0.918	1.006	0.180	2.1
0.10	0.15	265.3	6.0	−0.1	+1.2	−0.3	+0.1	−0.2	+2.0	1.9	+2.4	0.2	2.7	0.5	0.3	1.066	0.992	0.914	0.994	0.630	1.4
0.15	0.22	509	3.1	−0.6	+0.8	+0.4	−0.6	+0.7	+6.3	1.2	−1.6	0.2	2.7	0.5	0.2	1.074	0.991	0.917	0.991	1.252	9.0
0.22	0.30	457.6	3.7	−1.5	−1.1	−0.3	−0.6	+0.5	+3.9	1.1	+1.3	0.2	2.7	0.5	0.2	1.074	0.994	0.918	0.995	1.357	2.4
0.30	0.40	302.5	5.1	−0.9	−2.1	−0.4	−0.4	+0.3	+3.2	0.9	−1.9	0.2	2.7	0.5	0.2	1.077	0.991	0.919	0.996	1.302	2.5
0.40	0.54	195.5	5.5	+0.3	−2.3	−0.3	−1.2	+0.4	+5.7	0.7	+0.5	0.2	2.7	0.5	0.2	1.079	0.989	0.916	0.990	1.363	5.9
0.54	0.72	103.4	6.9	+0.3	−2.1	−0.2	−1.2	+0.6	+1.5	0.5	+0.8	0.2	2.7	0.5	0.2	1.073	0.997	0.922	0.997	1.368	7.8
0.72	0.86	101	7.4	−0.6	−1.7	−0.2	−0.9	+0.5	+2.8	0.9	−0.2	0.2	2.7	0.5	0.2	1.077	0.993	0.918	0.997	1.343	4.8
0.86	0.98	103.1	6.4	−0.8	−1.5	−0.0	−0.4	+0.5	−2.5	0.5	−0.1	0.2	2.7	0.5	0.2	1.078	0.996	0.917	0.993	1.471	3.4
0.98	1.00	566.2	4.2	−1.9	−0.3	−0.1	+0.7	+0.2	−1.8	0.3	−0.0	0.2	2.7	0.5	0.2	1.079	0.993	0.917	0.993	0.727	1.7

Table 9 Differential 1-jettiness cross sections for $e^- p$ ($\mathcal{L} = 351.1\,\mathrm{pb}^{-1}$) scattering in the range $200 < Q^2 < 280\,\mathrm{GeV}^2$ and $0.05 < y < 0.10$, $\mathrm{d}\sigma/\mathrm{d}\tau_1^b$ [pb/$\Delta\tau_1^b$]. Further details are given in the caption of Table 2

Cross sections in $e^- p$ ($\mathcal{L} = 351.1\,\mathrm{pb}^{-1}$) for $200 < Q^2 < 280\,\mathrm{GeV}^2$ and $0.05 < y < 0.10 - \mathrm{d}\sigma/\mathrm{d}\tau_1^b$ [pb/$\Delta\tau_1^b$]

τ_1^b range		Results $\frac{\mathrm{d}\sigma}{\mathrm{d}\tau_1^b}$	Uncertainties													Correction factors					
Min	Max		Stat	RCES	JES	HadTh	ElEn	ElTh	Model	MCstat	Unfold	ElecID	Lumi	Uncor	QED	c_{QED}	c_{NoZ}	c_{Born}	$c_{\mathrm{e+p}}$	c_{Had}	δ_{Had}
		(pb)	(%)	(%)	(%)	(%)	(%)	(%)	(%)	(%)	(%)	(%)	(%)	(%)	(%)						(%)
0.00	0.10	45.03	8.0	+1.8	+1.4	+1.1	−1.4	+0.5	−8.9	0.9	+2.3	0.2	2.7	0.5	0.6	1.062	0.993	0.929	0.997	0.220	2.2
0.10	0.15	445.6	2.1	+2.2	+0.7	+0.6	−1.6	+0.6	−0.4	0.8	−0.6	0.2	2.7	0.5	0.4	1.083	0.989	0.907	0.992	1.767	24.8
0.15	0.22	495.6	1.7	+0.6	+0.1	−0.2	−0.9	+0.5	+4.7	0.8	−0.8	0.2	2.7	0.5	0.4	1.068	0.991	0.909	0.998	2.198	28.3
0.22	0.30	328.5	3.0	+0.2	+0.1	−0.6	−1.2	+0.4	+8.9	1.5	−2.1	0.2	2.7	0.5	0.4	1.067	0.991	0.913	1.003	1.617	1.6
0.30	0.40	147.8	6.5	+4.0	−0.4	+0.3	−3.3	+1.2	+1.2	1.9	+6.8	0.2	2.7	0.5	0.4	1.064	0.998	0.911	0.998	1.447	2.5
0.40	0.60	96.42	4.9	+2.8	+0.1	+0.7	−2.3	+1.5	−3.9	1.1	−3.0	0.2	2.7	0.5	0.4	1.078	0.987	0.903	0.987	1.407	5.6
0.60	1.00	53.08	6.2	+0.8	+0.4	+0.7	−1.4	+0.3	−10.7	1.1	−1.0	0.2	2.7	0.5	0.3	1.079	0.994	0.913	0.990	1.189	1.2

of the data. The classical MC event generators Djangoh and Rapgap, which were optimised for HERA physics, provide an overall good description. The more recent general purpose MC event generators Herwig 7.2, Pythia 8.3, Sherpa 2.2 and Sherpa 3.0 provide a good description of the data, although some problems remain to be resolved in regions of the phase-space specific for each model. When studying different parton shower or hadronization models, the potential of these data for the optimization of event generators is demonstrated.

Fixed order pQCD predictions provide a good description of the data, but sizeable non-perturbative corrections for hadronization effects have to be applied. When incorporating NLL resummation, such predictions are seen to be in good agreement with the data over the full range of τ_1^b. Future pQCD analyses may be able to constrain parton distribution functions of the proton (PDFs) or the strong coupling constant from the data.

The τ_1^b-integrated triple-differential cross sections are found to be in agreement with the previously measured double-differential inclusive NC DIS cross section. This provides an important consistency test of the data, but also a consistency check with the HERA legacy measurements of inclusive NC DIS. The inclusive NC DIS cross section is described by structure function calculations which are available up to aN3LO and which are free of hadronization effects. The 1-jettiness measurement as a function of τ_1^b, Q^2, and y can be viewed as a generalised NC DIS cross section, and is the first triple-differential measurement of this kind.

In summary, it is believed that these data will be highly valuable to improve MC event generators, which are of importance to achieve the physics goals of the HL-LHC physics program [188,189]. Further improvements can be achieved when complemented with recent jet substructure measurements [190]. With an improved understanding of soft

Table 10 Differential 1-jettiness cross sections for $e^- p$ ($\mathcal{L} = 351.1\,\text{pb}^{-1}$) scattering in the range $200 < Q^2 < 280\,\text{GeV}^2$ and $0.10 < y < 0.20$, $d\sigma/d\tau_1^b$ [pb/$\Delta\tau_1^b$]. Further details are given in the caption of Table 2

Cross sections in $e^- p$ ($\mathcal{L} = 351.1\,\text{pb}^{-1}$) for $200 < Q^2 < 280\,\text{GeV}^2$ and $0.10 < y < 0.20$ – $d\sigma/d\tau_1^b$ [pb/$\Delta\tau_1^b$]

τ_1^b range		Results	Uncertainties													Correction factors					
Min	Max	$\frac{d\sigma}{d\tau_1^b}$	Stat	RCES	JES	HadTh	ElEn	ElTh	Model	MCstat	Unfold	ElecID	Lumi	Uncor	QED	c_{QED}	c_{NoZ}	c_{Born}	c_{e+p}	c_{Had}	δ_{Had}
		(pb)	(%)	(%)	(%)	(%)	(%)	(%)	(%)	(%)	(%)	(%)	(%)	(%)	(%)						(%)
0.00	0.05	11.36	35.5	+0.2	+1.2	+1.8	−0.6	+0.9	−26.9	4.7	−2.2	0.2	2.7	0.5	1.6	1.097	0.961	0.918	0.999	0.031	0.4
0.05	0.10	137.6	8.2	+1.3	+1.9	+1.0	−2.1	+0.7	−8.2	1.5	+1.1	0.2	2.7	0.5	0.5	1.089	0.996	0.910	1.000	0.402	7.2
0.10	0.15	513.3	3.3	+1.7	+0.8	+0.6	−0.3	+0.6	−0.6	1.5	−1.7	0.2	2.7	0.5	0.3	1.077	0.988	0.908	0.995	1.398	18.7
0.15	0.22	518	2.9	−0.5	−0.0	−0.5	−2.0	+0.2	+6.2	1.3	+1.8	0.2	2.7	0.5	0.3	1.067	0.992	0.915	0.990	1.848	20.7
0.22	0.30	369.6	4.3	+0.6	+0.2	+0.1	−0.6	+0.9	+6.1	1.7	−2.5	0.2	2.7	0.5	0.3	1.073	0.994	0.915	0.990	1.476	1.2
0.30	0.40	185.9	7.5	+2.0	−0.7	−0.5	−1.8	+1.1	+2.7	1.4	+4.0	0.2	2.7	0.5	0.3	1.073	0.991	0.919	0.989	1.389	2.7
0.40	0.54	148.9	5.8	+2.0	−0.4	+0.1	−2.0	+1.2	−5.2	1.1	−1.5	0.2	2.7	0.5	0.3	1.074	0.989	0.912	0.992	1.385	7.5
0.54	0.72	82.71	6.6	+1.0	−0.0	+0.1	−2.1	+1.0	−4.8	0.7	−1.3	0.2	2.7	0.5	0.3	1.069	1.002	0.919	0.999	1.335	5.1
0.72	0.86	68.07	8.3	+0.2	−0.4	−0.3	−1.1	+0.6	−5.3	1.0	−0.4	0.2	2.7	0.5	0.3	1.071	0.995	0.920	0.998	1.297	2.0
0.86	0.98	72.56	8.2	−0.7	−1.0	−0.4	+0.2	+0.8	−6.2	1.0	+0.0	0.2	2.7	0.5	0.3	1.071	1.003	0.920	0.993	1.383	1.9
0.98	1.00	230.1	7.4	−1.8	−0.6	−0.6	−0.2	+0.6	−2.5	0.7	+0.2	0.2	2.7	0.5	0.4	1.069	0.998	0.919	1.007	0.696	1.6

Table 11 Differential 1-jettiness cross sections for $e^- p$ ($\mathcal{L} = 351.1\,\text{pb}^{-1}$) scattering in the range $200 < Q^2 < 280\,\text{GeV}^2$ and $0.20 < y < 0.40$, $d\sigma/d\tau_1^b$ [pb/$\Delta\tau_1^b$]. Further details are given in the caption of Table 2

Cross sections in $e^- p$ ($\mathcal{L} = 351.1\,\text{pb}^{-1}$) for $200 < Q^2 < 280\,\text{GeV}^2$ and $0.20 < y < 0.40$ – $d\sigma/d\tau_1^b$ [pb/$\Delta\tau_1^b$]

τ_1^b range		Results	Uncertainties													Correction factors					
Min	Max	$\frac{d\sigma}{d\tau_1^b}$	Stat	RCES	JES	HadTh	ElEn	ElTh	Model	MCstat	Unfold	ElecID	Lumi	Uncor	QED	c_{QED}	c_{NoZ}	c_{Born}	c_{e+p}	c_{Had}	δ_{Had}
		(pb)	(%)	(%)	(%)	(%)	(%)	(%)	(%)	(%)	(%)	(%)	(%)	(%)	(%)						(%)
0.00	0.05	16.71	23.2	+0.3	+1.7	+1.8	−1.5	+0.3	−30.4	3.9	−9.2	0.2	2.7	0.5	1.3	1.044	1.002	0.940	1.023	0.027	0.3
0.05	0.10	122.6	8.4	+1.2	+1.6	+1.0	−0.9	+0.3	−8.8	1.5	+2.4	0.2	2.7	0.5	0.4	1.068	0.997	0.917	0.992	0.332	4.7
0.10	0.15	507.5	3.1	−0.0	+1.1	−0.1	−0.4	+0.3	+2.4	1.2	−2.3	0.2	2.7	0.5	0.3	1.070	0.996	0.921	0.992	1.145	12.5
0.15	0.22	543.5	2.7	+0.8	+0.3	+0.2	−1.3	+1.1	+4.8	1.0	+2.1	0.2	2.7	0.5	0.2	1.067	0.998	0.921	1.000	1.563	10.5
0.22	0.30	418.1	3.5	+0.5	+0.1	+0.0	−0.5	+0.7	+2.1	1.0	−2.2	0.2	2.7	0.5	0.2	1.071	0.993	0.917	0.994	1.347	4.6
0.30	0.40	226.8	5.6	+0.9	−0.4	−0.2	−1.3	+0.5	+3.5	0.7	+1.5	0.2	2.7	0.5	0.2	1.074	0.991	0.916	0.992	1.343	3.1
0.40	0.54	162.3	4.9	+1.4	−0.4	−0.2	−1.7	+0.6	+1.4	0.6	+0.1	0.2	2.7	0.5	0.2	1.072	0.992	0.913	0.991	1.357	7.0
0.54	0.72	106.6	5.0	+0.9	−0.3	−0.2	−1.3	+0.7	−2.8	0.4	−0.4	0.2	2.7	0.5	0.2	1.078	0.990	0.912	0.992	1.321	5.9
0.72	0.86	82.38	6.5	+0.2	−0.4	−0.2	−0.9	+0.7	−3.9	0.5	−0.6	0.2	2.7	0.5	0.2	1.076	0.994	0.914	0.998	1.291	2.8
0.86	0.98	79.12	6.6	+0.2	−0.9	+0.0	−0.5	+0.5	−1.4	0.5	−0.2	0.2	2.7	0.5	0.2	1.074	0.996	0.915	0.996	1.390	2.1
0.98	1.00	353.2	4.8	−1.1	−0.3	−0.2	−0.2	+0.5	−2.0	0.3	+0.0	0.2	2.7	0.5	0.3	1.081	0.991	0.919	0.992	0.729	1.5

and non-perturbative effects, these data will become useful for the determination of PDFs or the value of the strong coupling constant $\alpha_s(m_Z)$. The presented measurement at HERA can be complemented in the future with measurements in electron–proton collisions at lower center-of-mass energies at the electron–ion collider in Brookhaven (EIC) [191] or at higher energies at the LHeC or FCC-eh at CERN [191–193], or with measurements in pp at the LHC.

Table 12 Differential 1-jettiness cross sections for $e^- p$ ($\mathcal{L} = 351.1\,\text{pb}^{-1}$) scattering in the range $200 < Q^2 < 280\,\text{GeV}^2$ and $0.40 < y < 0.70$, $d\sigma/d\tau_1^b$ [pb/$\Delta\tau_1^b$]. Further details are given in the caption of Table 2

Cross sections in $e^- p$ ($\mathcal{L} = 351.1\,\text{pb}^{-1}$) for $200 < Q^2 < 280\,\text{GeV}^2$ and $0.40 < y < 0.70$ – $d\sigma/d\tau_1^b$ [pb/$\Delta\tau_1^b$]

τ_1^b range		Results	Uncertainties													Correction factors					
Min	Max	$\frac{d\sigma}{d\tau_1^b}$	Stat	RCES	JES	HadTh	ElEn	ElTh	Model	MCstat	Unfold	ElecID	Lumi	Uncor	QED	c_{QED}	c_{NoZ}	c_{Born}	c_{e+p}	c_{Had}	δ_{Had}
		(pb)	(%)	(%)	(%)	(%)	(%)	(%)	(%)	(%)	(%)	(%)	(%)	(%)	(%)						(%)
0.00	0.05	9.507	39.2	−0.9	+2.6	+0.6	+1.1	−0.0	−24.6	3.8	−2.2	0.2	2.7	0.5	1.3	1.076	1.015	0.912	0.989	0.026	0.3
0.05	0.10	96.74	10.0	−0.7	+2.4	+0.6	+1.3	+0.2	−6.6	1.8	−2.0	0.2	2.7	0.5	0.4	1.069	0.999	0.920	0.994	0.287	3.3
0.10	0.15	319.3	4.7	−1.0	+0.9	+0.1	−0.1	+0.7	+3.7	1.3	+2.2	0.2	2.7	0.5	0.2	1.076	0.988	0.911	0.982	0.985	8.4
0.15	0.22	458.5	3.1	−0.8	−0.4	−0.2	−0.5	−0.0	+2.6	1.1	−1.4	0.2	2.7	0.5	0.2	1.068	0.994	0.917	0.999	1.395	3.9
0.22	0.30	341.5	4.2	−0.9	−0.3	−0.1	−0.6	+0.5	+2.5	1.0	+1.7	0.2	2.7	0.5	0.2	1.077	0.988	0.909	0.992	1.297	6.8
0.30	0.40	205.8	6.1	+0.0	−0.7	−0.2	−0.7	+0.5	+5.1	0.7	−3.6	0.2	2.7	0.5	0.2	1.068	0.993	0.920	0.995	1.307	1.5
0.40	0.54	140.8	5.7	+0.4	−1.5	−0.2	−1.0	+0.6	+3.0	0.6	+0.9	0.2	2.7	0.5	0.2	1.073	0.991	0.915	0.991	1.344	7.2
0.54	0.72	84.76	6.4	+0.0	−1.9	−0.1	−0.9	+0.5	+1.1	0.5	+1.1	0.2	2.7	0.5	0.2	1.074	0.995	0.912	0.998	1.313	6.7
0.72	0.86	64.95	8.4	−0.3	−1.5	−0.2	−0.9	+0.4	+1.9	0.7	+1.0	0.2	2.7	0.5	0.2	1.076	0.990	0.916	0.991	1.287	2.9
0.86	0.98	84.47	6.2	−0.3	−1.1	+0.0	−0.4	+0.5	+1.0	0.5	+0.1	0.2	2.7	0.5	0.2	1.075	0.997	0.912	0.994	1.402	2.5
0.98	1.00	326.4	5.3	−1.7	−0.2	−0.1	+0.5	+0.2	−0.4	0.3	−0.0	0.2	2.7	0.5	0.3	1.078	0.992	0.913	0.989	0.750	1.4

Table 13 Differential 1-jettiness cross sections for $e^- p$ ($\mathcal{L} = 351.1\,\text{pb}^{-1}$) scattering in the range $280 < Q^2 < 440\,\text{GeV}^2$ and $0.05 < y < 0.10$, $d\sigma/d\tau_1^b$ [pb/$\Delta\tau_1^b$]. Further details are given in the caption of Table 2

Cross sections in $e^- p$ ($\mathcal{L} = 351.1\,\text{pb}^{-1}$) for $280 < Q^2 < 440\,\text{GeV}^2$ and $0.05 < y < 0.10$ – $d\sigma/d\tau_1^b$ [pb/$\Delta\tau_1^b$]

τ_1^b range		Results	Uncertainties													Correction factors					
Min	Max	$\frac{d\sigma}{d\tau_1^b}$	Stat	RCES	JES	HadTh	ElEn	ElTh	Model	MCstat	Unfold	ElecID	Lumi	Uncor	QED	c_{QED}	c_{NoZ}	c_{Born}	c_{e+p}	c_{Had}	δ_{Had}
		(pb)	(%)	(%)	(%)	(%)	(%)	(%)	(%)	(%)	(%)	(%)	(%)	(%)	(%)						(%)
0.00	0.10	104.9	3.9	+1.7	+1.1	+0.8	−1.3	+0.4	−5.8	0.5	+2.6	0.2	2.7	0.5	0.4	1.071	0.985	0.911	0.992	0.367	1.9
0.10	0.15	506	1.8	+1.5	+0.3	+0.1	−1.4	+0.6	+3.3	0.7	−1.2	0.2	2.7	0.5	0.4	1.066	1.002	0.914	0.997	2.570	56.1
0.15	0.22	386.6	2.1	+0.2	+0.0	−0.3	−1.3	+0.7	+6.6	1.0	−3.4	0.2	2.7	0.5	0.4	1.060	0.997	0.916	0.993	1.878	4.7
0.22	0.30	231	3.8	+0.3	−0.4	−0.7	−0.1	+0.8	+4.7	1.9	+4.1	0.2	2.7	0.5	0.4	1.073	0.983	0.909	0.991	1.465	2.3
0.30	0.40	107.9	8.2	+4.6	−0.0	+1.5	−3.4	+1.1	−1.8	2.0	−0.1	0.2	2.7	0.5	0.4	1.073	0.993	0.906	0.978	1.402	4.9
0.40	0.60	69.51	5.6	+3.8	+0.1	+0.8	−4.0	+1.1	−7.3	1.2	−0.4	0.2	2.7	0.5	0.4	1.077	0.997	0.910	0.989	1.336	4.8
0.60	1.00	24.5	10.4	+0.5	−0.7	+0.3	−0.6	+0.4	−9.7	1.5	−0.3	0.2	2.7	0.5	0.3	1.067	0.986	0.914	0.997	1.154	0.2

Table 14 Differential 1-jettiness cross sections for $e^- p$ ($\mathcal{L} = 351.1\,\text{pb}^{-1}$) scattering in the range $280 < Q^2 < 440\,\text{GeV}^2$ and $0.10 < y < 0.20$, $d\sigma/d\tau_1^b$ [pb/$\Delta\tau_1^b$]. Further details are given in the caption of Table 2

Cross sections in $e^- p$ ($\mathcal{L} = 351.1\,\text{pb}^{-1}$) for $280 < Q^2 < 440\,\text{GeV}^2$ and $0.10 < y < 0.20 - d\sigma/d\tau_1^b$ [pb/$\Delta\tau_1^b$]

τ_1^b range		Results	Uncertainties												Correction factors					
Min	Max	$\frac{d\sigma}{d\tau_1^b}$	Stat	RCES	JES	HadTh	ElEn	ElTh	Model	MCstat	Unfold	ElecID	Lumi	Uncor	QED	c_{QED}	c_{NoZ}	c_{Born}	c_{e+p}	c_{Had}	δ_{Had}
		(pb)	(%)	(%)	(%)	(%)	(%)	(%)	(%)	(%)	(%)	(%)	(%)	(%)	(%)						(%)
0.00	0.05	11.91	35.5	+0.1	+1.5	+0.8	−0.4	+0.5	−20.6	2.1	−4.8	0.2	2.7	0.5	0.9	1.087	1.004	0.896	0.991	0.054	1.0
0.05	0.10	236.8	4.9	+1.7	+1.3	+0.7	−1.3	+0.2	−3.9	0.9	+0.3	0.2	2.7	0.5	0.3	1.066	0.996	0.917	0.991	0.769	0.5
0.10	0.15	569.4	2.8	+1.4	+0.3	+0.2	−1.6	+0.6	+3.8	1.2	−0.7	0.2	2.7	0.5	0.3	1.066	0.990	0.915	0.996	2.037	38.7
0.15	0.22	426.9	3.3	−0.5	−0.0	−0.0	+0.7	+0.6	+5.8	1.4	+1.9	0.2	2.7	0.5	0.2	1.066	0.989	0.909	0.990	1.639	0.8
0.22	0.30	273.2	5.0	+0.7	−0.2	−0.8	−1.8	+0.4	+5.2	1.5	−2.5	0.2	2.7	0.5	0.3	1.071	0.984	0.908	0.987	1.388	2.1
0.30	0.40	141.1	8.3	+2.7	−0.0	+0.1	−2.6	+0.9	−3.3	1.3	−1.3	0.2	2.7	0.5	0.3	1.069	0.990	0.908	0.988	1.368	6.2
0.40	0.54	89.72	7.4	+2.8	−0.7	−0.0	−1.8	+0.7	−5.9	1.0	+2.5	0.2	2.7	0.5	0.3	1.071	0.990	0.912	0.997	1.333	6.5
0.54	0.72	57.96	7.3	+1.0	−0.1	+0.2	−1.2	+0.6	−4.2	0.7	+0.6	0.2	2.7	0.5	0.3	1.068	0.999	0.913	1.003	1.263	3.3
0.72	0.86	40.8	10.7	+0.5	−0.1	+0.2	−0.2	+0.5	−5.1	1.1	+0.5	0.2	2.7	0.5	0.4	1.065	1.001	0.915	0.998	1.232	0.6
0.86	0.98	43.06	10.7	−0.3	−1.3	−0.2	+1.2	+0.3	−4.5	1.2	+0.1	0.2	2.7	0.5	0.4	1.083	0.985	0.907	0.985	1.324	2.1
0.98	1.00	94.78	13.6	−1.6	−0.4	−0.2	−0.2	+0.3	−4.9	1.0	+0.0	0.2	2.7	0.5	0.5	1.070	0.994	0.916	0.993	0.716	1.7

Table 15 Differential 1-jettiness cross sections for $e^- p$ ($\mathcal{L} = 351.1\,\text{pb}^{-1}$) scattering in the range $280 < Q^2 < 440\,\text{GeV}^2$ and $0.20 < y < 0.40$, $d\sigma/d\tau_1^b$ [pb/$\Delta\tau_1^b$]. Further details are given in the caption of Table 2

Cross sections in $e^- p$ ($\mathcal{L} = 351.1\,\text{pb}^{-1}$) for $280 < Q^2 < 440\,\text{GeV}^2$ and $0.20 < y < 0.40 - d\sigma/d\tau_1^b$ [pb/$\Delta\tau_1^b$]

τ_1^b range		Results	Uncertainties												Correction factors					
Min	Max	$\frac{d\sigma}{d\tau_1^b}$	Stat	RCES	JES	HadTh	ElEn	ElTh	Model	MCstat	Unfold	ElecID	Lumi	Uncor	QED	c_{QED}	c_{NoZ}	c_{Born}	c_{e+p}	c_{Had}	δ_{Had}
		(pb)	(%)	(%)	(%)	(%)	(%)	(%)	(%)	(%)	(%)	(%)	(%)	(%)	(%)						(%)
0.00	0.05	11.35	35.5	−0.4	+1.5	+1.4	−0.0	+0.4	−25.2	1.9	+0.2	0.2	2.7	0.5	0.8	1.065	1.006	0.941	0.998	0.048	0.8
0.05	0.10	247.2	4.5	+0.7	+1.4	+0.6	−1.1	+0.4	−3.5	0.9	−0.1	0.2	2.7	0.5	0.3	1.075	0.989	0.910	0.986	0.634	0.1
0.10	0.15	571.6	2.7	+0.9	+0.5	+0.1	−1.0	+0.4	+5.5	0.9	+0.9	0.2	2.7	0.5	0.2	1.068	0.998	0.916	0.994	1.645	23.9
0.15	0.22	495.9	2.7	+0.0	+0.0	−0.2	−0.8	+0.3	+1.6	1.0	−1.7	0.2	2.7	0.5	0.2	1.073	0.989	0.912	0.988	1.455	5.1
0.22	0.30	294.9	4.3	+0.7	+0.3	−0.2	−1.0	+0.6	+3.4	0.9	+2.1	0.2	2.7	0.5	0.2	1.071	0.992	0.915	0.996	1.317	2.1
0.30	0.40	180.7	5.8	+1.4	−0.5	−0.1	−1.1	+0.7	+1.5	0.6	−0.1	0.2	2.7	0.5	0.2	1.073	0.992	0.910	0.990	1.338	6.0
0.40	0.54	123.4	5.0	+1.8	−0.5	−0.1	−1.7	+0.8	−0.8	0.5	−1.0	0.2	2.7	0.5	0.2	1.069	0.993	0.915	0.991	1.305	7.0
0.54	0.72	77.16	5.2	+1.0	−0.3	−0.2	−1.7	+0.6	−3.4	0.4	−0.1	0.2	2.7	0.5	0.2	1.077	0.989	0.904	0.992	1.261	4.6
0.72	0.86	47.36	8.0	+0.3	−0.4	−0.1	−1.2	+0.6	−3.2	0.5	+0.2	0.2	2.7	0.5	0.3	1.073	0.994	0.911	0.996	1.233	1.5
0.86	0.98	52	7.6	+0.4	−0.7	+0.0	−0.7	+0.6	−1.6	0.5	+0.1	0.2	2.7	0.5	0.3	1.068	0.998	0.915	0.998	1.322	0.9
0.98	1.00	223.1	5.8	−1.3	−0.3	−0.3	+0.0	+0.2	−2.8	0.4	−0.0	0.2	2.7	0.5	0.3	1.071	0.995	0.918	0.998	0.757	0.9

Table 16 Differential 1-jettiness cross sections for $e^- p$ ($\mathcal{L} = 351.1\,\text{pb}^{-1}$) scattering in the range $280 < Q^2 < 440\,\text{GeV}^2$ and $0.40 < y < 0.70$, $d\sigma/d\tau_1^b$ [pb/$\Delta\tau_1^b$]. Further details are given in the caption of Table 2

Cross sections in $e^- p$ ($\mathcal{L} = 351.1\,\text{pb}^{-1}$) for $280 < Q^2 < 440\,\text{GeV}^2$ and $0.40 < y < 0.70$ – $d\sigma/d\tau_1^b$ [pb/$\Delta\tau_1^b$]

τ_1^b range		Results	Uncertainties												Correction factors					
Min	Max	$\frac{d\sigma}{d\tau_1^b}$	Stat	RCES	JES	HadTh	ElEn	ElTh	Model	MCstat	Unfold	ElecID	Lumi	Uncor	QED	c_{QED}	c_{NoZ}	c_{Born}	$c_{\text{e+p}}$	c_{Had}	δ_{Had}
		(pb)	(%)	(%)	(%)	(%)	(%)	(%)	(%)	(%)	(%)	(%)	(%)	(%)	(%)						(%)
0.00	0.05	17	23.3	−0.3	+1.8	+0.4	−2.2	+0.5	−26.2	2.2	−9.6	0.2	2.7	0.5	0.8	1.081	0.976	0.902	0.994	0.044	0.8
0.05	0.10	154	6.5	−0.2	+1.9	+0.3	−0.4	+0.6	−0.1	1.1	+0.8	0.2	2.7	0.5	0.3	1.073	0.992	0.914	0.992	0.543	0.3
0.10	0.15	448.9	3.3	−0.9	+0.6	+0.2	+0.3	+0.3	+3.0	1.0	−0.8	0.2	2.7	0.5	0.2	1.076	0.985	0.908	0.984	1.398	13.1
0.15	0.22	373.1	3.4	−1.0	−0.1	−0.2	−0.4	+0.3	+1.2	0.9	+0.8	0.2	2.7	0.5	0.2	1.068	0.992	0.912	0.991	1.334	8.4
0.22	0.30	259.3	4.7	+0.1	−0.5	−0.2	−0.9	+0.5	+4.6	0.8	−0.2	0.2	2.7	0.5	0.2	1.067	0.993	0.911	0.990	1.276	3.5
0.30	0.40	158.8	6.5	+0.1	−1.0	−0.3	−1.0	+0.4	+3.8	0.6	−0.4	0.2	2.7	0.5	0.2	1.078	0.984	0.908	0.990	1.320	5.7
0.40	0.54	98.91	6.4	+0.4	−1.4	−0.3	−1.4	+0.5	+2.0	0.5	+0.3	0.2	2.7	0.5	0.2	1.074	0.992	0.912	0.992	1.297	7.0
0.54	0.72	61.33	6.8	+0.1	−1.4	−0.1	−1.1	+0.4	+0.3	0.5	+0.0	0.2	2.7	0.5	0.2	1.076	0.985	0.908	0.990	1.259	5.0
0.72	0.86	41.18	10.1	−0.1	−0.9	−0.1	−1.1	+0.5	−1.0	0.7	−0.1	0.2	2.7	0.5	0.3	1.079	0.988	0.910	0.989	1.224	2.1
0.86	0.98	55.33	7.8	−0.0	−1.0	−0.0	−0.5	+0.4	−0.1	0.6	−0.1	0.2	2.7	0.5	0.3	1.070	0.987	0.913	0.996	1.329	1.7
0.98	1.00	241.8	6.1	−1.5	−0.0	−0.1	+0.4	+0.4	+1.0	0.4	−0.0	0.2	2.7	0.5	0.3	1.083	0.982	0.908	0.987	0.781	0.9

Table 17 Differential 1-jettiness cross sections for $e^- p$ ($\mathcal{L} = 351.1\,\text{pb}^{-1}$) scattering in the range $440 < Q^2 < 700\,\text{GeV}^2$ and $0.05 < y < 0.10$, $d\sigma/d\tau_1^b$ [pb/$\Delta\tau_1^b$]. Further details are given in the caption of Table 2

Cross sections in $e^- p$ ($\mathcal{L} = 351.1\,\text{pb}^{-1}$) for $440 < Q^2 < 700\,\text{GeV}^2$ and $0.05 < y < 0.10$ – $d\sigma/d\tau_1^b$ [pb/$\Delta\tau_1^b$]

τ_1^b range		Results	Uncertainties												Correction factors					
Min	Max	$\frac{d\sigma}{d\tau_1^b}$	Stat	RCES	JES	HadTh	ElEn	ElTh	Model	MCstat	Unfold	ElecID	Lumi	Uncor	QED	c_{QED}	c_{NoZ}	c_{Born}	$c_{\text{e+p}}$	c_{Had}	δ_{Had}
		(pb)	(%)	(%)	(%)	(%)	(%)	(%)	(%)	(%)	(%)	(%)	(%)	(%)	(%)						(%)
0.00	0.10	128.7	3.1	+1.0	+0.8	+0.0	−1.4	+0.2	−0.5	0.4	+2.0	0.2	2.7	0.5	0.3	1.073	0.993	0.911	0.998	0.584	0.1
0.10	0.15	317.4	2.6	+1.2	−0.0	+0.2	−1.4	+0.7	+2.7	1.0	−3.2	0.2	2.7	0.5	0.4	1.067	0.983	0.905	0.979	2.321	16.2
0.15	0.22	204.5	3.5	−0.4	−0.1	−1.5	−1.4	+0.0	+4.3	1.8	−2.7	0.2	2.7	0.5	0.4	1.061	0.993	0.910	0.987	1.556	5.6
0.22	0.30	111	6.8	+0.6	−0.0	+0.1	−0.4	+0.6	+0.1	3.2	+7.7	0.2	2.7	0.5	0.5	1.052	0.997	0.913	0.993	1.407	4.1
0.30	0.40	46.09	16.2	+8.4	−0.4	+3.1	−4.6	+1.6	−3.4	3.0	−5.4	0.2	2.7	0.5	0.5	1.064	0.990	0.908	0.993	1.333	3.7
0.40	0.60	24.56	11.8	+1.7	−0.2	+0.3	−5.1	+0.1	−3.3	2.0	+1.2	0.2	2.7	0.5	0.5	1.070	0.986	0.911	0.996	1.255	2.8
0.60	1.00	12.81	14.5	−0.3	+0.2	+0.4	−7.3	+0.3	−18.6	2.5	+0.5	0.2	2.7	0.5	0.5	1.059	0.999	0.917	1.004	1.116	0.3

Table 18 Differential 1-jettiness cross sections for $e^- p$ ($\mathcal{L} = 351.1\,\text{pb}^{-1}$) scattering in the range $440 < Q^2 < 700\,\text{GeV}^2$ and $0.10 < y < 0.20$, $d\sigma/d\tau_1^b$ [pb/$\Delta\tau_1^b$]. Further details are given in the caption of Table 2

Cross sections in $e^- p$ ($\mathcal{L} = 351.1\,\text{pb}^{-1}$) for $440 < Q^2 < 700\,\text{GeV}^2$ and $0.10 < y < 0.20$ – $d\sigma/d\tau_1^b$ [pb/$\Delta\tau_1^b$]

τ_1^b range		Results	Uncertainties													Correction factors					
Min	Max	$\frac{d\sigma}{d\tau_1^b}$	Stat	RCES	JES	HadTh	ElEn	ElTh	Model	MCstat	Unfold	ElecID	Lumi	Uncor	QED	c_{QED}	c_{NoZ}	c_{Born}	c_{e+p}	c_{Had}	δ_{Had}
		(pb)	(%)	(%)	(%)	(%)	(%)	(%)	(%)	(%)	(%)	(%)	(%)	(%)	(%)						(%)
0.00	0.05	11.17	39.1	+0.7	+1.3	+1.2	−0.6	+0.1	−15.9	1.3	−2.8	0.2	2.7	0.5	0.6	1.087	0.989	0.907	0.982	0.107	1.8
0.05	0.10	268.4	4.3	+1.5	+0.8	+0.3	−1.6	+0.4	−0.4	0.7	+0.2	0.2	2.7	0.5	0.3	1.083	0.986	0.906	0.987	1.679	38.7
0.10	0.15	389.6	3.7	+0.7	−0.0	−0.3	−1.2	+0.2	+7.6	1.6	+0.7	0.2	2.7	0.5	0.3	1.063	0.994	0.913	0.991	1.918	8.2
0.15	0.22	253.9	4.8	+1.3	+0.2	+0.6	−1.9	+0.9	+4.2	2.1	−1.8	0.2	2.7	0.5	0.3	1.073	0.986	0.904	0.981	1.436	7.1
0.22	0.30	103.1	10.9	+0.2	−0.4	−0.9	−1.4	+0.2	−1.0	1.9	+3.0	0.2	2.7	0.5	0.3	1.071	0.981	0.904	0.990	1.358	3.5
0.30	0.40	86.4	10.2	+3.0	−0.8	−0.0	−2.3	+0.8	−5.1	1.6	−2.7	0.2	2.7	0.5	0.3	1.071	0.983	0.908	0.989	1.324	6.8
0.40	0.54	42.77	11.2	+3.0	−0.5	−0.0	−2.9	+0.7	−8.4	1.2	+0.8	0.2	2.7	0.5	0.4	1.078	0.985	0.902	0.985	1.255	4.2
0.54	0.72	22.96	12.2	+0.8	−0.5	+0.2	−2.1	+0.6	−4.3	1.0	+0.8	0.2	2.7	0.5	0.4	1.068	0.984	0.902	0.990	1.204	1.9
0.72	0.86	15.99	18.0	+0.2	−0.4	+0.2	−0.7	+0.4	−5.8	1.7	+0.4	0.2	2.7	0.5	0.6	1.078	0.991	0.899	0.995	1.169	0.2
0.86	0.98	12.09	26.4	−0.4	−1.5	−0.4	+1.7	+0.2	−8.2	2.1	+0.1	0.2	2.7	0.5	0.6	1.087	0.979	0.885	0.977	1.261	0.7
0.98	1.00	38.79	25.4	−0.9	−0.1	+0.4	−2.5	+0.2	−0.2	2.2	−0.0	0.2	2.7	0.5	0.8	1.073	0.980	0.922	0.987	0.740	0.9

Table 19 Differential 1-jettiness cross sections for $e^- p$ ($\mathcal{L} = 351.1\,\text{pb}^{-1}$) scattering in the range $440 < Q^2 < 700\,\text{GeV}^2$ and $0.20 < y < 0.40$, $d\sigma/d\tau_1^b$ [pb/$\Delta\tau_1^b$]. Further details are given in the caption of Table 2

Cross sections in $e^- p$ ($\mathcal{L} = 351.1\,\text{pb}^{-1}$) for $440 < Q^2 < 700\,\text{GeV}^2$ and $0.20 < y < 0.40$ – $d\sigma/d\tau_1^b$ [pb/$\Delta\tau_1^b$]

τ_1^b range		Results	Uncertainties													Correction factors					
Min	Max	$\frac{d\sigma}{d\tau_1^b}$	Stat	RCES	JES	HadTh	ElEn	ElTh	Model	MCstat	Unfold	ElecID	Lumi	Uncor	QED	c_{QED}	c_{NoZ}	c_{Born}	c_{e+p}	c_{Had}	δ_{Had}
		(pb)	(%)	(%)	(%)	(%)	(%)	(%)	(%)	(%)	(%)	(%)	(%)	(%)	(%)						(%)
0.00	0.05	18.95	24.2	+0.2	+1.7	+1.1	−1.3	+0.3	−17.9	1.2	−2.2	0.2	2.7	0.5	0.5	1.086	0.980	0.913	0.960	0.097	1.6
0.05	0.10	279.5	4.1	+1.2	+0.9	+0.5	−1.4	+0.6	+1.1	0.7	+1.2	0.2	2.7	0.5	0.2	1.077	0.993	0.912	0.989	1.328	26.0
0.10	0.15	440.9	3.2	+0.2	+0.2	−0.3	−1.2	+0.4	+6.7	1.1	−1.6	0.2	2.7	0.5	0.2	1.073	0.987	0.908	0.984	1.631	0.2
0.15	0.22	260.5	4.3	+0.4	−0.0	−0.3	−0.4	+0.3	+1.8	1.2	+1.1	0.2	2.7	0.5	0.2	1.073	0.983	0.909	0.986	1.339	7.6
0.22	0.30	149	7.0	+1.2	−0.5	−0.0	−1.6	+0.6	+2.4	1.1	−2.9	0.2	2.7	0.5	0.2	1.070	0.985	0.907	0.988	1.317	4.6
0.30	0.40	94.93	8.1	+2.0	−0.4	−0.2	−1.8	+0.4	−2.6	0.8	+1.3	0.2	2.7	0.5	0.3	1.077	0.981	0.906	0.987	1.297	6.3
0.40	0.54	53.97	8.3	+2.3	−0.7	−0.1	−2.3	+0.4	−4.1	0.7	+1.7	0.2	2.7	0.5	0.3	1.072	0.991	0.906	0.990	1.245	5.2
0.54	0.72	31.57	8.8	+1.1	−0.2	−0.2	−2.0	+0.5	−4.9	0.6	+0.5	0.2	2.7	0.5	0.3	1.071	0.990	0.910	0.993	1.198	3.1
0.72	0.86	20.45	12.9	+0.6	−0.4	+0.1	−1.6	+0.4	−2.0	0.9	+0.2	0.2	2.7	0.5	0.4	1.077	0.987	0.901	0.983	1.183	0.7
0.86	0.98	23.25	12.3	+0.2	−1.0	−0.2	−1.4	+0.4	−2.8	1.0	+0.0	0.2	2.7	0.5	0.5	1.078	0.982	0.911	0.983	1.254	0.9
0.98	1.00	76.32	11.7	−1.4	−0.2	−0.3	−0.7	+0.6	−2.8	0.8	+0.0	0.2	2.7	0.5	0.6	1.072	0.989	0.903	0.992	0.789	0.7

Table 20 Differential 1-jettiness cross sections for $e^- p$ ($\mathcal{L} = 351.1\,\text{pb}^{-1}$) scattering in the range $440 < Q^2 < 700\,\text{GeV}^2$ and $0.40 < y < 0.70$, $d\sigma/d\tau_1^b$ [pb/$\Delta\tau_1^b$]. Further details are given in the caption of Table 2

Cross sections in $e^- p$ ($\mathcal{L} = 351.1\,\text{pb}^{-1}$) for $440 < Q^2 < 700\,\text{GeV}^2$ and $0.40 < y < 0.70$ – $d\sigma/d\tau_1^b$ [pb/$\Delta\tau_1^b$]

τ_1^b range		Results	Uncertainties												Correction factors					
Min	Max	$\frac{d\sigma}{d\tau_1^b}$	Stat	RCES	JES	HadTh	ElEn	ElTh	Model	MCstat	Unfold	ElecID	Lumi	Uncor	QED	c_{QED}	c_{NoZ}	c_{Born}	c_{e+p}	c_{Had}	δ_{Had}
		(pb)	(%)	(%)	(%)	(%)	(%)	(%)	(%)	(%)	(%)	(%)	(%)	(%)	(%)						(%)
0.00	0.05	2.629	131.4	+0.0	+2.0	+0.8	+0.1	+0.8	−21.0	2.3	−3.0	0.2	2.7	0.5	0.7	1.085	0.997	0.916	0.989	0.088	1.4
0.05	0.10	205.5	4.6	+0.5	+1.4	+0.2	−0.5	+0.3	+2.2	0.9	+1.4	0.2	2.7	0.5	0.2	1.084	0.984	0.910	0.973	1.098	17.7
0.10	0.15	344.8	3.7	−0.1	+0.2	+0.1	+0.1	+0.5	−0.7	1.1	−2.5	0.2	2.7	0.5	0.2	1.075	0.987	0.909	0.987	1.431	6.1
0.15	0.22	194.6	5.1	+0.0	+0.3	−0.1	−0.6	+0.2	+4.7	1.0	+2.3	0.2	2.7	0.5	0.2	1.068	0.991	0.911	0.989	1.274	9.1
0.22	0.30	120.5	7.6	+0.3	−0.7	−0.4	−1.2	+0.1	+4.9	1.0	−0.6	0.2	2.7	0.5	0.3	1.074	0.987	0.909	0.989	1.299	3.6
0.30	0.40	83.33	8.2	+0.6	−1.2	−0.3	−1.1	+0.4	+2.1	0.7	−1.8	0.2	2.7	0.5	0.3	1.073	0.983	0.910	0.984	1.287	6.7
0.40	0.54	41.72	9.8	+1.0	−1.0	−0.3	−1.5	+0.3	+0.1	0.7	+0.9	0.2	2.7	0.5	0.3	1.074	0.987	0.908	0.997	1.242	5.6
0.54	0.72	25.87	10.4	+0.6	−1.0	−0.2	−1.6	+0.3	−1.6	0.6	+0.6	0.2	2.7	0.5	0.3	1.083	0.979	0.905	0.983	1.196	3.6
0.72	0.86	21.48	12.3	−0.7	−0.9	−0.3	−1.1	+0.1	+0.4	0.9	+0.2	0.2	2.7	0.5	0.4	1.075	0.987	0.902	0.991	1.176	1.3
0.86	0.98	22.04	12.8	−0.0	−0.8	−0.0	−0.4	+0.3	−1.5	0.9	+0.0	0.2	2.7	0.5	0.4	1.089	0.971	0.901	0.980	1.254	1.4
0.98	1.00	110.2	9.2	−1.4	+0.1	−0.0	+0.0	+0.1	−1.6	0.7	−0.0	0.2	2.7	0.5	0.5	1.085	0.986	0.909	0.993	0.819	0.8

Table 21 Differential 1-jettiness cross sections for $e^- p$ ($\mathcal{L} = 351.1\,\text{pb}^{-1}$) scattering in the range $700 < Q^2 < 1100\,\text{GeV}^2$ and $0.05 < y < 0.10$, $d\sigma/d\tau_1^b$ [pb/$\Delta\tau_1^b$]. Further details are given in the caption of Table 2

Cross sections in $e^- p$ ($\mathcal{L} = 351.1\,\text{pb}^{-1}$) for $700 < Q^2 < 1100\,\text{GeV}^2$ and $0.05 < y < 0.10$ – $d\sigma/d\tau_1^b$ [pb/$\Delta\tau_1^b$]

τ_1^b range		Results	Uncertainties												Correction factors					
Min	Max	$\frac{d\sigma}{d\tau_1^b}$	Stat	RCES	JES	HadTh	ElEn	ElTh	Model	MCstat	Unfold	ElecID	Lumi	Uncor	QED	c_{QED}	c_{NoZ}	c_{Born}	c_{e+p}	c_{Had}	δ_{Had}
		(pb)	(%)	(%)	(%)	(%)	(%)	(%)	(%)	(%)	(%)	(%)	(%)	(%)	(%)						(%)
0.00	0.10	125.3	3.2	+1.1	+0.6	+0.0	−1.3	+0.2	+1.1	0.4	−0.1	0.2	2.7	0.5	0.3	1.096	0.974	0.899	0.978	0.765	0.3
0.10	0.15	178.5	4.1	+0.7	−0.5	−0.8	−1.0	+1.1	+1.2	1.9	−1.9	0.2	2.7	0.5	0.4	1.050	0.996	0.909	1.001	1.821	5.8
0.15	0.22	93	6.7	+0.7	+0.6	−0.0	−2.2	−0.6	+5.7	3.3	+1.9	0.2	2.7	0.5	0.5	1.061	0.984	0.898	0.983	1.462	2.5
0.22	0.30	33.92	19.7	+1.2	−0.1	+0.0	−1.5	+1.5	−5.0	5.9	+6.1	0.2	2.7	0.5	0.6	1.052	0.984	0.901	0.982	1.337	5.4
0.30	0.40	26.09	26.1	−1.1	−1.3	−1.0	+0.1	+0.0	+0.7	6.0	−16.1	0.2	2.7	0.5	0.7	1.080	0.961	0.892	0.973	1.267	3.8
0.40	0.60	8.686	26.3	−1.4	−1.0	−2.3	−1.4	−0.6	−15.2	4.4	+9.0	0.2	2.7	0.5	0.7	1.056	0.992	0.908	0.984	1.193	1.7
0.60	1.00	3.362	20.3	−5.7	−4.1	−3.3	+1.5	+0.1	−63.0	3.1	+1.8	0.2	2.7	0.5	0.9	1.078	1.014	0.920	0.981	1.086	0.2

Table 22 Differential 1-jettiness cross sections for e^-p ($\mathcal{L} = 351.1$ pb^{-1}) scattering in the range $700 < Q^2 < 1100$ GeV^2 and $0.10 < y < 0.20$, $d\sigma/d\tau_1^b$ [pb/$\Delta\tau_1^b$]. Further details are given in the caption of Table 2

Cross sections in e^-p ($\mathcal{L} = 351.1$ pb^{-1}) for $700 < Q^2 < 1100$ GeV^2 and $0.10 < y < 0.20$ – $d\sigma/d\tau_1^b$ [pb/$\Delta\tau_1^b$]																				
τ_1^b range		Results	Uncertainties												Correction factors					
Min	Max	$\frac{d\sigma}{d\tau_1^b}$	Stat	RCES	JES	HadTh	ElEn	ElTh	Model	MCstat	Unfold	ElecID	Lumi	Uncor	QED	c_{QED}	c_{NoZ}	c_{Born}	c_{e+p}	c_{Had}	δ_{Had}
		(pb)	(%)	(%)	(%)	(%)	(%)	(%)	(%)	(%)	(%)	(%)	(%)	(%)	(%)						(%)
0.00	0.05	15.7	30.6	−0.2	+1.3	+0.7	−0.4	+0.0	−13.2	0.9	−3.1	0.2	2.7	0.5	0.4	1.095	0.970	0.911	0.975	0.214	1.8
0.05	0.10	222	4.9	+1.5	+0.2	−0.1	−1.0	+0.4	+2.6	0.8	+1.1	0.2	2.7	0.5	0.2	1.077	0.981	0.905	0.979	2.237	43.4
0.10	0.15	211.6	6.1	+2.2	+0.2	−0.2	−1.6	+0.6	+5.9	2.3	−0.3	0.2	2.7	0.5	0.3	1.067	0.975	0.904	0.972	1.622	11.3
0.15	0.22	102.7	9.9	+1.1	−0.4	+0.9	−1.4	+0.8	+3.0	2.8	−0.7	0.2	2.7	0.5	0.3	1.060	0.984	0.910	0.986	1.369	0.7
0.22	0.30	56.49	17.0	+1.9	−0.5	−0.4	−2.2	−0.0	+0.3	3.1	−0.5	0.2	2.7	0.5	0.4	1.068	0.978	0.904	0.984	1.315	5.4
0.30	0.40	34.25	21.5	−0.1	−0.6	−1.0	−0.6	−0.2	−3.8	2.6	+2.1	0.2	2.7	0.5	0.5	1.080	0.978	0.906	0.973	1.254	4.7
0.40	0.54	12.81	30.7	+0.9	−0.4	+0.2	−0.4	+0.1	−9.9	2.2	+0.4	0.2	2.7	0.5	0.5	1.071	0.966	0.913	0.990	1.195	2.6
0.54	0.72	13.37	16.7	+0.1	−0.6	+0.0	−0.0	+0.7	−7.6	2.0	−0.6	0.2	2.7	0.5	0.6	1.057	0.985	0.927	0.984	1.154	1.4
0.72	0.86	9.534	20.7	+0.2	−1.2	+0.8	+0.6	+1.1	−2.6	2.9	−1.1	0.2	2.7	0.5	1.0	1.078	0.970	0.879	0.962	1.131	0.6
0.86	0.98	2.186	56.3	−0.8	−1.2	−0.3	+1.0	+0.8	−10.4	2.6	−0.3	0.2	2.7	0.5	1.1	1.068	0.982	0.925	0.977	1.208	0.7
0.98	1.00	2.081	154.8	−1.8	+0.2	−1.4	−1.8	+0.3	+10.0	2.7	+0.0	0.2	2.7	0.5	1.6	1.063	0.988	0.919	1.012	0.749	1.0

Table 23 Differential 1-jettiness cross sections for e^-p ($\mathcal{L} = 351.1$ pb^{-1}) scattering in the range $700 < Q^2 < 1100$ GeV^2 and $0.20 < y < 0.40$, $d\sigma/d\tau_1^b$ [pb/$\Delta\tau_1^b$]. Further details are given in the caption of Table 2

Cross sections in e^-p ($\mathcal{L} = 351.1$ pb^{-1}) for $700 < Q^2 < 1100$ GeV^2 and $0.20 < y < 0.40$ – $d\sigma/d\tau_1^b$ [pb/$\Delta\tau_1^b$]																				
τ_1^b range		Results	Uncertainties												Correction factors					
Min	Max	$\frac{d\sigma}{d\tau_1^b}$	Stat	RCES	JES	HadTh	ElEn	ElTh	Model	MCstat	Unfold	ElecID	Lumi	Uncor	QED	c_{QED}	c_{NoZ}	c_{Born}	c_{e+p}	c_{Had}	δ_{Had}
		(pb)	(%)	(%)	(%)	(%)	(%)	(%)	(%)	(%)	(%)	(%)	(%)	(%)	(%)						(%)
0.00	0.05	15.95	27.4	+0.3	+1.7	+1.0	−0.6	−0.0	−14.7	0.8	−0.1	0.2	2.7	0.5	0.4	1.103	0.973	0.909	0.973	0.195	1.5
0.05	0.10	269.2	3.7	+1.0	+0.4	−0.0	−1.3	+0.2	+4.0	0.7	+0.6	0.2	2.7	0.5	0.2	1.090	0.975	0.904	0.964	1.803	26.2
0.10	0.15	219.1	5.2	+0.5	−0.0	−0.3	−1.1	+0.3	+6.0	1.4	−2.4	0.2	2.7	0.5	0.3	1.077	0.980	0.910	0.973	1.456	12.3
0.15	0.22	115.6	7.5	+1.1	−0.2	−0.2	−0.5	+0.7	+2.1	1.5	+2.0	0.2	2.7	0.5	0.3	1.071	0.981	0.908	0.979	1.309	0.3
0.22	0.30	71.41	11.1	+1.6	−0.4	+0.1	−0.4	+0.2	−1.7	1.6	+2.3	0.2	2.7	0.5	0.4	1.078	0.969	0.898	0.973	1.292	6.3
0.30	0.40	49.4	10.9	+1.5	−0.7	−0.1	−0.8	+0.5	−5.3	1.2	−2.6	0.2	2.7	0.5	0.4	1.077	0.969	0.897	0.977	1.246	5.0
0.40	0.54	23.64	12.9	+1.1	−0.6	−0.0	−1.1	+0.5	−3.0	1.0	−1.1	0.2	2.7	0.5	0.4	1.065	0.976	0.915	0.992	1.189	3.7
0.54	0.72	14.15	11.8	+0.5	−0.3	−0.1	−1.4	+0.3	−3.2	0.8	−0.2	0.2	2.7	0.5	0.5	1.079	0.967	0.905	0.977	1.153	1.5
0.72	0.86	10.46	15.1	−0.2	−0.7	−0.4	−0.5	+0.1	−3.8	1.3	−0.2	0.2	2.7	0.5	0.7	1.076	0.974	0.896	0.983	1.133	0.9
0.86	0.98	6.976	17.9	+0.3	−0.4	+0.0	−0.5	+0.5	+2.6	1.1	+0.0	0.2	2.7	0.5	0.8	1.085	0.976	0.904	0.980	1.208	0.7
0.98	1.00	27.64	16.3	−1.1	−0.1	−0.4	−1.1	+0.0	−1.9	1.1	−0.0	0.2	2.7	0.5	1.0	1.088	0.984	0.918	0.982	0.816	0.6

Table 24 Differential 1-jettiness cross sections for e^-p ($\mathcal{L} = 351.1\,\mathrm{pb}^{-1}$) scattering in the range $700 < Q^2 < 1100\,\mathrm{GeV}^2$ and $0.40 < y < 0.70$, $\mathrm{d}\sigma/\mathrm{d}\tau_1^b$ [pb/$\Delta\tau_1^b$]. Further details are given in the caption of Table 2

Cross sections in e^-p ($\mathcal{L} = 351.1\,\mathrm{pb}^{-1}$) for $700 < Q^2 < 1100\,\mathrm{GeV}^2$ and $0.40 < y < 0.70$ – $\mathrm{d}\sigma/\mathrm{d}\tau_1^b$ [pb/$\Delta\tau_1^b$]

τ_1^b range		Results $\frac{\mathrm{d}\sigma}{\mathrm{d}\tau_1^b}$	Uncertainties													Correction factors					
Min	Max		Stat	RCES	JES	HadTh	ElEn	ElTh	Model	MCstat	Unfold	ElecID	Lumi	Uncor	QED	c_{QED}	c_{NoZ}	c_{Born}	c_{e+p}	c_{Had}	δ_{Had}
		(pb)	(%)	(%)	(%)	(%)	(%)	(%)	(%)	(%)	(%)	(%)	(%)	(%)	(%)						(%)
0.00	0.05	13.16	28.1	−0.5	+1.8	+0.8	−0.3	+0.1	−13.5	1.0	+0.8	0.2	2.7	0.5	0.6	1.123	0.977	0.905	0.940	0.180	1.3
0.05	0.10	182.1	4.5	+0.5	+0.6	+0.1	−0.5	+0.3	+2.5	0.7	+0.2	0.2	2.7	0.5	0.3	1.095	0.970	0.906	0.958	1.503	16.0
0.10	0.15	175.6	5.6	+0.5	−0.0	−0.1	−1.3	+0.1	+5.7	1.1	−0.7	0.2	2.7	0.5	0.3	1.073	0.979	0.905	0.964	1.339	14.4
0.15	0.22	90.41	8.4	+0.3	−0.3	−0.3	−0.4	+0.4	+1.4	1.1	+2.7	0.2	2.7	0.5	0.3	1.079	0.978	0.906	0.972	1.284	1.1
0.22	0.30	62.72	10.0	+0.9	−0.4	−0.2	−0.8	+0.5	+0.1	1.1	−2.8	0.2	2.7	0.5	0.4	1.074	0.971	0.903	0.984	1.271	5.9
0.30	0.40	42.14	9.7	+0.9	−0.5	−0.3	−1.3	+0.1	−1.7	0.9	−1.1	0.2	2.7	0.5	0.4	1.069	0.981	0.903	0.981	1.237	6.2
0.40	0.54	15.84	14.6	+0.2	−0.7	−0.2	−0.6	+0.3	−2.0	0.7	+0.4	0.2	2.7	0.5	0.4	1.078	0.980	0.912	0.985	1.195	4.1
0.54	0.72	12.36	11.9	−0.2	−0.8	−0.3	−0.3	+0.3	−1.0	0.8	+0.2	0.2	2.7	0.5	0.5	1.094	0.965	0.893	0.970	1.152	2.6
0.72	0.86	8.715	15.9	−0.1	−0.6	−0.3	−0.9	+0.2	−0.5	1.2	+0.1	0.2	2.7	0.5	0.7	1.089	0.971	0.895	0.979	1.137	1.0
0.86	0.98	6.527	17.6	−0.4	−0.4	+0.1	−0.4	+0.3	+2.7	1.0	−0.0	0.2	2.7	0.5	0.7	1.064	0.989	0.922	1.010	1.190	0.3
0.98	1.00	42.34	12.8	−1.2	+0.0	−0.2	−0.3	+0.1	+0.1	0.8	−0.0	0.2	2.7	0.5	0.8	1.084	0.977	0.903	0.983	0.855	0.3

Table 25 Differential 1-jettiness cross sections for e^-p ($\mathcal{L} = 351.1\,\mathrm{pb}^{-1}$) scattering in the range $700 < Q^2 < 1100\,\mathrm{GeV}^2$ and $0.70 < y < 0.94$, $\mathrm{d}\sigma/\mathrm{d}\tau_1^b$ [pb/$\Delta\tau_1^b$]. Further details are given in the caption of Table 2

Cross sections in e^-p ($\mathcal{L} = 351.1\,\mathrm{pb}^{-1}$) for $700 < Q^2 < 1100\,\mathrm{GeV}^2$ and $0.70 < y < 0.94$ – $\mathrm{d}\sigma/\mathrm{d}\tau_1^b$ [pb/$\Delta\tau_1^b$]

τ_1^b range		Results $\frac{\mathrm{d}\sigma}{\mathrm{d}\tau_1^b}$	Uncertainties													Correction factors					
Min	Max		Stat	RCES	JES	HadTh	ElEn	ElTh	Model	MCstat	Unfold	ElecID	Lumi	Uncor	QED	c_{QED}	c_{NoZ}	c_{Born}	c_{e+p}	c_{Had}	δ_{Had}
		(pb)	(%)	(%)	(%)	(%)	(%)	(%)	(%)	(%)	(%)	(%)	(%)	(%)	(%)						(%)
0.00	0.05	1.341	319.0	−1.4	+2.8	+0.4	+0.4	+0.2	−20.8	3.1	+0.2	0.2	2.7	0.5	0.8	1.119	0.977	0.917	0.948	0.171	0.9
0.05	0.10	96.52	10.3	−1.9	+1.1	−0.6	+0.6	+0.2	+3.8	1.6	−1.1	0.2	2.7	0.5	0.4	1.102	0.981	0.906	0.958	1.418	18.8
0.10	0.15	87.85	12.6	−3.0	−0.5	+0.1	+1.3	−0.6	+3.9	2.1	+2.2	0.2	2.7	0.5	0.4	1.091	0.966	0.898	0.966	1.307	15.9
0.15	0.22	54.39	15.0	−1.7	−0.6	+0.1	−0.1	−0.1	+5.2	2.0	−2.9	0.2	2.7	0.5	0.4	1.084	0.973	0.903	0.966	1.273	0.5
0.22	0.30	33.11	20.3	−1.5	−2.1	+0.3	+0.3	+0.7	−0.5	2.5	−1.3	0.2	2.7	0.5	0.5	1.088	0.972	0.908	0.967	1.294	5.2
0.30	0.40	15.38	27.2	−1.3	−1.8	−0.2	+0.7	+0.4	−2.5	1.7	+2.4	0.2	2.7	0.5	0.5	1.078	0.967	0.901	0.980	1.241	5.4
0.40	0.54	13.33	18.9	−1.6	−1.5	−0.3	−0.3	+0.2	+0.3	1.7	+1.9	0.2	2.7	0.5	0.6	1.079	0.975	0.904	0.989	1.200	4.5
0.54	0.72	4.491	28.1	−1.5	−1.0	+0.1	−1.2	+0.1	−1.4	1.6	+0.5	0.2	2.7	0.5	0.7	1.073	0.964	0.895	0.995	1.157	2.6
0.72	0.86	3.584	36.5	−0.9	−0.9	−0.2	+0.5	−0.1	−0.3	2.4	+0.4	0.2	2.7	0.5	1.0	1.062	0.958	0.903	0.998	1.125	0.5
0.86	0.98	4.102	29.3	−0.8	−0.3	+0.3	−0.7	−0.3	−1.7	1.9	+0.0	0.2	2.7	0.5	1.0	1.070	0.984	0.905	0.992	1.197	0.7
0.98	1.00	19.88	28.0	−0.9	+0.1	−0.2	+0.4	+0.2	−0.3	1.6	+0.0	0.2	2.7	0.5	1.1	1.075	0.969	0.913	0.972	0.868	0.0

Table 26 Differential 1-jettiness cross sections for $e^- p$ ($\mathcal{L} = 351.1\,\mathrm{pb}^{-1}$) scattering in the range $1100 < Q^2 < 1700\,\mathrm{GeV}^2$ and $0.10 < y < 0.20$, $d\sigma/d\tau_1^b$ [pb/$\Delta\tau_1^b$]. Further details are given in the caption of Table 2

Cross sections in $e^- p$ ($\mathcal{L} = 351.1\,\mathrm{pb}^{-1}$) for $1100 < Q^2 < 1700\,\mathrm{GeV}^2$ and $0.10 < y < 0.20$ – $d\sigma/d\tau_1^b$ [pb/$\Delta\tau_1^b$]

τ_1^b range		Results	Uncertainties													Correction factors					
Min	Max	$\frac{d\sigma}{d\tau_1^b}$	Stat	RCES	JES	HadTh	ElEn	ElTh	Model	MCstat	Unfold	ElecID	Lumi	Uncor	QED	c_{QED}	c_{NoZ}	c_{Born}	$c_{\mathrm{e+p}}$	c_{Had}	δ_{Had}
		(pb)	(%)	(%)	(%)	(%)	(%)	(%)	(%)	(%)	(%)	(%)	(%)	(%)	(%)						(%)
0.00	0.05	11.5	33.1	+0.5	+1.4	+0.7	−0.9	+0.1	−7.9	0.7	+2.0	0.2	2.7	0.5	0.4	1.107	0.971	0.900	0.970	0.382	0.8
0.05	0.10	161.6	4.3	+2.6	+0.0	−0.2	−2.0	+0.3	+4.7	0.6	−3.0	0.2	2.7	0.5	0.3	1.093	0.963	0.899	0.963	2.097	3.3
0.10	0.15	97.38	5.8	+0.8	+0.2	+0.7	−2.1	−0.3	+5.7	2.1	+5.7	0.2	2.7	0.5	0.4	1.062	0.981	0.912	0.977	1.472	2.1
0.15	0.22	59.87	7.6	+1.6	−0.4	−0.7	−1.5	+0.7	−2.0	2.7	−5.3	0.2	2.7	0.5	0.5	1.068	0.972	0.907	0.971	1.338	4.7
0.22	0.30	19.89	21.9	+1.0	−1.4	−1.8	−0.0	+0.3	−2.6	3.3	+7.4	0.2	2.7	0.5	0.6	1.072	0.974	0.901	0.970	1.264	5.4
0.30	0.40	11.46	30.0	+3.0	−0.3	+2.0	−2.4	+0.2	−11.2	3.3	−5.9	0.2	2.7	0.5	0.7	1.084	0.954	0.903	0.999	1.197	3.0
0.40	0.60	5.774	21.2	+0.5	−0.0	−0.5	−1.5	−0.0	−12.0	2.0	+0.9	0.2	2.7	0.5	0.8	1.084	0.946	0.899	0.961	1.145	1.3
0.60	1.00	2.633	13.0	−2.2	−1.7	−1.0	+1.9	+0.4	−17.2	1.3	+0.1	0.2	2.7	0.5	0.9	1.072	0.973	0.901	0.978	1.066	0.1

Table 27 Differential 1-jettiness cross sections for $e^- p$ ($\mathcal{L} = 351.1\,\mathrm{pb}^{-1}$) scattering in the range $1100 < Q^2 < 1700\,\mathrm{GeV}^2$ and $0.20 < y < 0.40$, $d\sigma/d\tau_1^b$ [pb/$\Delta\tau_1^b$]. Further details are given in the caption of Table 2

Cross sections in $e^- p$ ($\mathcal{L} = 351.1\,\mathrm{pb}^{-1}$) for $1100 < Q^2 < 1700\,\mathrm{GeV}^2$ and $0.20 < y < 0.40$ – $d\sigma/d\tau_1^b$ [pb/$\Delta\tau_1^b$]

τ_1^b range		Results	Uncertainties													Correction factors					
Min	Max	$\frac{d\sigma}{d\tau_1^b}$	Stat	RCES	JES	HadTh	ElEn	ElTh	Model	MCstat	Unfold	ElecID	Lumi	Uncor	QED	c_{QED}	c_{NoZ}	c_{Born}	$c_{\mathrm{e+p}}$	c_{Had}	δ_{Had}
		(pb)	(%)	(%)	(%)	(%)	(%)	(%)	(%)	(%)	(%)	(%)	(%)	(%)	(%)						(%)
0.00	0.05	21.13	18.6	+0.2	+1.4	+0.6	−0.6	+0.1	−7.2	0.6	+0.3	0.2	2.7	0.5	0.4	1.115	0.955	0.909	0.939	0.355	0.7
0.05	0.10	182.9	4.4	+0.8	+0.0	−0.3	−0.8	+0.4	+4.0	0.7	+0.9	0.2	2.7	0.5	0.3	1.101	0.956	0.904	0.949	1.813	2.1
0.10	0.15	105.3	8.7	+1.9	+0.3	+0.1	−1.8	+0.3	+5.7	1.7	−2.3	0.2	2.7	0.5	0.4	1.080	0.960	0.904	0.956	1.362	6.4
0.15	0.22	55.2	12.6	+2.4	+0.1	−0.1	−2.1	+0.3	−0.0	1.8	−0.5	0.2	2.7	0.5	0.4	1.080	0.950	0.894	0.946	1.297	4.3
0.22	0.30	26.72	19.6	+1.8	−1.5	+0.2	−1.4	+0.3	−4.6	2.1	+2.0	0.2	2.7	0.5	0.5	1.071	0.960	0.903	0.949	1.250	5.9
0.30	0.40	16.28	20.1	+2.0	−1.1	−0.1	−2.2	+0.4	−6.3	1.6	+0.2	0.2	2.7	0.5	0.6	1.073	0.961	0.904	0.972	1.200	3.5
0.40	0.54	10.34	18.8	+1.5	−0.5	+0.1	−1.5	+0.3	−4.7	1.4	−0.6	0.2	2.7	0.5	0.7	1.082	0.942	0.904	0.970	1.143	2.5
0.54	0.72	5.197	20.5	+0.2	−0.5	−0.6	−0.1	+0.2	−1.6	1.4	−0.3	0.2	2.7	0.5	0.8	1.084	0.967	0.899	0.976	1.123	1.3
0.72	0.86	3.323	31.5	+0.8	−0.0	−0.3	−1.1	+0.3	−1.6	2.4	−0.4	0.2	2.7	0.5	1.2	1.084	0.947	0.915	0.998	1.089	0.4
0.86	0.98	3.105	24.2	+2.0	−0.6	+0.3	−1.4	+0.8	+0.5	2.0	+0.0	0.2	2.7	0.5	1.3	1.080	0.962	0.912	0.979	1.159	0.8
0.98	1.00	3.105	73.5	−1.4	+0.4	−0.2	−1.4	−0.3	+3.5	2.3	−0.1	0.2	2.7	0.5	1.8	1.098	0.950	0.896	0.946	0.844	1.4

Table 28 Differential 1-jettiness cross sections for $e^- p$ ($\mathcal{L} = 351.1\,\text{pb}^{-1}$) scattering in the range $1100 < Q^2 < 1700\,\text{GeV}^2$ and $0.40 < y < 0.70$, $d\sigma/d\tau_1^b$ [pb/$\Delta\tau_1^b$]. Further details are given in the caption of Table 2

Cross sections in $e^- p$ ($\mathcal{L} = 351.1\,\text{pb}^{-1}$) for $1100 < Q^2 < 1700\,\text{GeV}^2$ and $0.40 < y < 0.70$ – $d\sigma/d\tau_1^b$ [pb/$\Delta\tau_1^b$]

τ_1^b range		Results	Uncertainties													Correction factors					
Min	Max	$\frac{d\sigma}{d\tau_1^b}$	Stat	RCES	JES	HadTh	ElEn	ElTh	Model	MCstat	Unfold	ElecID	Lumi	Uncor	QED	c_{QED}	c_{NoZ}	c_{Born}	$c_{\text{e+p}}$	c_{Had}	δ_{Had}
		(pb)	(%)	(%)	(%)	(%)	(%)	(%)	(%)	(%)	(%)	(%)	(%)	(%)	(%)						(%)
0.00	0.05	22.63	17.4	−0.0	+1.7	+0.7	−0.8	+0.1	−6.8	0.8	+0.4	0.2	2.7	0.5	0.5	1.141	0.947	0.896	0.907	0.332	0.2
0.05	0.10	148	5.1	+0.7	−0.2	−0.1	−0.6	+0.2	+3.8	0.7	+1.1	0.2	2.7	0.5	0.3	1.119	0.945	0.899	0.925	1.568	3.8
0.10	0.15	94.38	8.7	+0.5	−0.2	−0.5	−1.3	+0.1	+3.2	1.3	−3.2	0.2	2.7	0.5	0.4	1.078	0.967	0.901	0.957	1.300	7.6
0.15	0.22	44.35	13.4	+2.0	+0.0	−0.1	−1.5	+0.3	+3.0	1.4	−2.9	0.2	2.7	0.5	0.5	1.083	0.955	0.899	0.946	1.273	3.9
0.22	0.30	26.23	15.6	+0.9	−0.1	−0.1	−1.6	+0.2	−3.1	1.5	+3.2	0.2	2.7	0.5	0.5	1.092	0.941	0.890	0.938	1.242	5.7
0.30	0.40	12.07	21.5	+1.4	−0.5	−0.2	−1.1	+0.2	−2.7	1.2	+2.3	0.2	2.7	0.5	0.6	1.084	0.961	0.904	0.971	1.196	5.5
0.40	0.54	10.26	15.4	+0.4	−0.6	−0.4	−0.5	+0.3	−1.8	1.1	+0.7	0.2	2.7	0.5	0.7	1.084	0.957	0.903	0.962	1.147	2.9
0.54	0.72	4.849	19.5	+0.5	−0.5	−0.2	−1.2	+0.1	−3.2	1.2	+0.2	0.2	2.7	0.5	0.8	1.096	0.948	0.901	0.963	1.115	0.9
0.72	0.86	1.712	53.8	+0.7	−0.7	+0.4	−0.1	+0.6	−2.3	2.1	+0.1	0.2	2.7	0.5	1.1	1.083	0.972	0.923	1.002	1.105	1.7
0.86	0.98	3.884	20.7	−0.8	−0.2	+0.1	+0.1	+0.3	+3.2	1.8	−0.0	0.2	2.7	0.5	1.2	1.069	1.012	0.901	0.995	1.156	0.0
0.98	1.00	18.09	20.8	−0.8	−0.0	−0.4	−0.4	+0.5	−0.7	1.5	+0.0	0.2	2.7	0.5	1.4	1.107	0.910	0.900	0.971	0.886	1.0

Table 29 Differential 1-jettiness cross sections for $e^- p$ ($\mathcal{L} = 351.1\,\text{pb}^{-1}$) scattering in the range $1100 < Q^2 < 1700\,\text{GeV}^2$ and $0.70 < y < 0.94$, $d\sigma/d\tau_1^b$ [pb/$\Delta\tau_1^b$]. Further details are given in the caption of Table 2

Cross sections in $e^- p$ ($\mathcal{L} = 351.1\,\text{pb}^{-1}$) for $1100 < Q^2 < 1700\,\text{GeV}^2$ and $0.70 < y < 0.94$ – $d\sigma/d\tau_1^b$ [pb/$\Delta\tau_1^b$]

τ_1^b range		Results	Uncertainties													Correction factors					
Min	Max	$\frac{d\sigma}{d\tau_1^b}$	Stat	RCES	JES	HadTh	ElEn	ElTh	Model	MCstat	Unfold	ElecID	Lumi	Uncor	QED	c_{QED}	c_{NoZ}	c_{Born}	$c_{\text{e+p}}$	c_{Had}	δ_{Had}
		(pb)	(%)	(%)	(%)	(%)	(%)	(%)	(%)	(%)	(%)	(%)	(%)	(%)	(%)						(%)
0.00	0.05	2.415	108.7	−0.7	+2.2	+0.6	+0.4	+0.0	−3.6	1.3	+2.1	0.2	2.7	0.5	0.8	1.146	0.956	0.908	0.919	0.317	0.4
0.05	0.10	66.87	9.2	−0.6	−0.1	+0.2	+0.1	+0.1	+2.3	1.1	+3.3	0.2	2.7	0.5	0.4	1.109	0.954	0.915	0.931	1.490	2.7
0.10	0.15	55.26	13.2	−0.6	−0.2	−0.3	−0.1	−0.0	+8.2	1.9	−10.6	0.2	2.7	0.5	0.6	1.083	0.956	0.903	0.955	1.277	9.1
0.15	0.22	23.6	20.0	−0.1	−0.7	−0.3	+0.5	+0.5	+1.3	1.9	−2.1	0.2	2.7	0.5	0.6	1.079	0.968	0.904	0.965	1.272	3.7
0.22	0.30	15.63	21.2	+0.4	−0.6	+0.0	−0.2	+0.1	+1.3	2.1	+5.6	0.2	2.7	0.5	0.7	1.091	0.938	0.908	0.950	1.249	6.5
0.30	0.40	7.329	27.1	−0.6	−0.6	+0.4	+0.1	+0.3	−1.9	1.8	+3.0	0.2	2.7	0.5	0.8	1.096	0.949	0.892	0.959	1.204	4.4
0.40	0.54	4.424	25.4	+0.6	−0.4	−0.1	−1.1	+0.4	+4.5	2.1	+0.9	0.2	2.7	0.5	0.9	1.100	0.933	0.884	0.984	1.144	2.4
0.54	0.72	2.391	24.6	+0.4	−0.5	−0.4	+0.2	−0.2	+9.3	1.9	+0.1	0.2	2.7	0.5	1.1	1.048	0.972	0.922	0.980	1.118	1.3
0.72	0.86	1.123	56.9	−0.2	−1.0	+0.4	−0.1	+0.5	+2.2	3.0	+0.2	0.2	2.7	0.5	1.5	1.117	0.906	0.894	0.963	1.115	1.3
0.86	0.98	2.133	29.7	−0.7	−0.5	+0.4	+0.7	−0.0	−3.5	2.2	+0.1	0.2	2.7	0.5	1.6	1.099	0.926	0.910	0.953	1.144	2.0
0.98	1.00	7.173	34.9	+1.7	+1.1	+0.5	−1.4	+0.2	+17.8	2.4	−0.2	0.2	2.7	0.5	1.8	1.099	0.953	0.925	0.939	0.899	1.9

Table 30 Differential 1-jettiness cross sections for $e^- p$ ($\mathcal{L} = 351.1\,\text{pb}^{-1}$) scattering in the range $1700 < Q^2 < 3500\,\text{GeV}^2$ and $0.20 < y < 0.40$, $d\sigma/d\tau_1^b$ [pb/$\Delta\tau_1^b$]. Further details are given in the caption of Table 2

Cross sections in $e^- p$ ($\mathcal{L} = 351.1\,\text{pb}^{-1}$) for $1700 < Q^2 < 3500\,\text{GeV}^2$ and $0.20 < y < 0.40$ – $d\sigma/d\tau_1^b$ [pb/$\Delta\tau_1^b$]

τ_1^b range		Results	Uncertainties													Correction factors					
Min	Max	$\frac{d\sigma}{d\tau_1^b}$	Stat	RCES	JES	HadTh	ElEn	ElTh	Model	MCstat	Unfold	ElecID	Lumi	Uncor	QED	c_{QED}	c_{NoZ}	c_{Born}	c_{e+p}	c_{Had}	δ_{Had}
		(pb)	(%)	(%)	(%)	(%)	(%)	(%)	(%)	(%)	(%)	(%)	(%)	(%)	(%)						(%)
0.00	0.05	42.95	9.1	+1.3	+1.1	+0.7	−1.4	−0.0	−2.9	0.4	+3.0	0.2	2.7	0.5	0.3	1.147	0.924	0.905	0.896	0.581	1.2
0.05	0.10	177.8	3.7	+3.1	−0.2	−0.1	−2.5	+0.1	+3.5	0.6	−6.8	0.2	2.7	0.5	0.3	1.132	0.916	0.891	0.897	1.644	11.1
0.10	0.15	71.91	6.8	+2.9	−0.1	+0.3	−3.0	+0.3	+3.4	1.5	+7.4	0.2	2.7	0.5	0.5	1.097	0.915	0.905	0.923	1.338	3.2
0.15	0.22	28.89	12.1	+2.2	−0.6	−0.3	−1.3	+0.1	−8.9	1.8	−1.4	0.2	2.7	0.5	0.5	1.089	0.912	0.907	0.918	1.248	5.6
0.22	0.30	26.55	12.9	+2.5	−0.3	−0.3	−1.9	+0.0	−5.3	2.3	+2.0	0.2	2.7	0.5	0.7	1.103	0.916	0.906	0.933	1.194	4.8
0.30	0.40	7.71	28.0	+2.9	−0.8	+0.1	−2.1	−0.3	−0.7	2.0	−4.0	0.2	2.7	0.5	0.8	1.089	0.905	0.900	0.916	1.145	1.4
0.40	0.60	4.787	17.1	+2.1	−0.7	−0.6	−2.1	+0.2	−5.4	1.3	−1.0	0.2	2.7	0.5	0.8	1.068	0.937	0.919	0.951	1.108	1.8
0.60	1.00	1.517	15.6	+0.8	−0.6	−0.1	−1.2	+0.2	−5.4	0.9	−0.0	0.2	2.7	0.5	0.9	1.123	0.917	0.886	0.907	1.055	0.1

Table 31 Differential 1-jettiness cross sections for $e^- p$ ($\mathcal{L} = 351.1\,\text{pb}^{-1}$) scattering in the range $1700 < Q^2 < 3500\,\text{GeV}^2$ and $0.40 < y < 0.70$, $d\sigma/d\tau_1^b$ [pb/$\Delta\tau_1^b$]. Further details are given in the caption of Table 2

Cross sections in $e^- p$ ($\mathcal{L} = 351.1\,\text{pb}^{-1}$) for $1700 < Q^2 < 3500\,\text{GeV}^2$ and $0.40 < y < 0.70$ – $d\sigma/d\tau_1^b$ [pb/$\Delta\tau_1^b$]

τ_1^b range		Results	Uncertainties													Correction factors					
Min	Max	$\frac{d\sigma}{d\tau_1^b}$	Stat	RCES	JES	HadTh	ElEn	ElTh	Model	MCstat	Unfold	ElecID	Lumi	Uncor	QED	c_{QED}	c_{NoZ}	c_{Born}	c_{e+p}	c_{Had}	δ_{Had}
		(pb)	(%)	(%)	(%)	(%)	(%)	(%)	(%)	(%)	(%)	(%)	(%)	(%)	(%)						(%)
0.00	0.05	53.27	7.1	+0.6	+1.3	+0.5	−0.6	+0.1	−0.4	0.4	+2.9	0.2	2.7	0.5	0.4	1.182	0.894	0.904	0.846	0.554	1.1
0.05	0.10	135.8	4.3	+2.0	−0.1	−0.2	−1.7	+0.0	+2.7	0.6	−5.2	0.2	2.7	0.5	0.3	1.139	0.911	0.899	0.882	1.515	9.8
0.10	0.15	55.25	7.8	+1.7	−0.4	−0.1	−0.7	+0.1	+0.8	1.1	+6.2	0.2	2.7	0.5	0.5	1.134	0.892	0.887	0.881	1.292	0.0
0.15	0.22	33.89	8.9	+1.9	−0.6	−0.1	−1.0	+0.2	−1.4	1.2	−4.7	0.2	2.7	0.5	0.6	1.110	0.910	0.912	0.913	1.236	5.2
0.22	0.30	18.45	14.4	+2.0	−0.8	−0.5	−1.4	−0.1	−1.2	1.6	+1.8	0.2	2.7	0.5	0.7	1.099	0.919	0.906	0.928	1.187	5.2
0.30	0.40	8.945	18.6	+1.9	−0.3	+0.1	−1.4	−0.1	−1.4	1.3	+1.1	0.2	2.7	0.5	0.8	1.109	0.907	0.901	0.938	1.139	3.1
0.40	0.60	6.976	10.8	+1.2	−0.5	−0.0	−1.0	+0.2	−1.8	0.9	−0.3	0.2	2.7	0.5	0.8	1.103	0.918	0.903	0.920	1.110	1.8
0.60	1.00	1.636	15.0	+0.9	−0.1	−0.0	−0.8	+0.1	+3.4	0.8	+0.0	0.2	2.7	0.5	0.8	1.093	0.912	0.919	0.949	1.056	0.1

Table 32 Differential 1-jettiness cross sections for $e^- p$ ($\mathcal{L} = 351.1\,\text{pb}^{-1}$) scattering in the range $1700 < Q^2 < 3500\,\text{GeV}^2$ and $0.70 < y < 0.94$, $d\sigma/d\tau_1^b$ [pb/$\Delta\tau_1^b$]. Further details are given in the caption of Table 2

Cross sections in $e^- p$ ($\mathcal{L} = 351.1\,\text{pb}^{-1}$) for $1700 < Q^2 < 3500\,\text{GeV}^2$ and $0.70 < y < 0.94$ – $d\sigma/d\tau_1^b$ [pb/$\Delta\tau_1^b$]

τ_1^b range		Results	Uncertainties													Correction factors					
Min	Max	$\frac{d\sigma}{d\tau_1^b}$	Stat	RCES	JES	HadTh	ElEn	ElTh	Model	MCstat	Unfold	ElecID	Lumi	Uncor	QED	c_{QED}	c_{NoZ}	c_{Born}	c_{e+p}	c_{Had}	δ_{Had}
		(pb)	(%)	(%)	(%)	(%)	(%)	(%)	(%)	(%)	(%)	(%)	(%)	(%)	(%)						(%)
0.00	0.05	25.11	10.8	−0.4	+1.4	+0.4	+0.1	+0.3	+2.7	0.8	+1.3	0.2	2.7	0.5	0.6	1.198	0.896	0.903	0.823	0.542	0.0
0.05	0.10	65.45	6.4	−0.1	−0.2	−0.2	−0.0	+0.3	+1.9	0.8	−1.1	0.2	2.7	0.5	0.5	1.144	0.900	0.901	0.869	1.440	11.7
0.10	0.15	30.58	10.7	+0.5	+0.1	+0.0	−1.1	+0.3	+8.1	1.4	−0.4	0.2	2.7	0.5	0.7	1.107	0.903	0.905	0.897	1.271	0.5
0.15	0.22	18.43	12.7	+0.4	−0.9	−0.5	−0.3	+0.1	−1.2	1.5	−0.2	0.2	2.7	0.5	0.7	1.113	0.905	0.889	0.896	1.242	5.7
0.22	0.30	8.302	21.3	+0.9	−0.9	+0.4	+0.3	+0.0	−4.0	2.1	+1.3	0.2	2.7	0.5	0.9	1.101	0.927	0.920	0.904	1.194	3.7
0.30	0.40	7.743	15.7	+0.6	−0.9	−0.1	+0.4	+0.2	−1.7	2.0	−0.8	0.2	2.7	0.5	1.0	1.089	0.905	0.926	0.937	1.137	2.8
0.40	0.60	2.171	20.0	+1.1	−0.3	−0.3	−1.3	+0.1	+7.9	1.4	−0.2	0.2	2.7	0.5	1.0	1.090	0.941	0.903	0.943	1.121	1.7
0.60	1.00	1.109	15.6	+0.8	−0.2	+0.1	−0.7	−0.0	+3.7	1.0	−0.0	0.2	2.7	0.5	1.1	1.104	0.905	0.891	0.935	1.050	0.4

Table 33 Differential 1-jettiness cross sections for e^-p ($\mathcal{L} = 351.1\,\text{pb}^{-1}$) scattering in the range $3500 < Q^2 < 8000\,\text{GeV}^2$ and $0.20 < y < 0.40$, $d\sigma/d\tau_1^b$ [pb/$\Delta\tau_1^b$]. Further details are given in the caption of Table 2

Cross sections in e^-p ($\mathcal{L} = 351.1\,\text{pb}^{-1}$) for $3500 < Q^2 < 8000\,\text{GeV}^2$ and $0.20 < y < 0.40$ – $d\sigma/d\tau_1^b$ [pb/$\Delta\tau_1^b$]

τ_1^b range		Results $\frac{d\sigma}{d\tau_1^b}$	Uncertainties													Correction factors					
Min	Max		Stat	RCES	JES	HadTh	ElEn	ElTh	Model	MCstat	Unfold	ElecID	Lumi	Uncor	QED	c_{QED}	c_{NoZ}	c_{Born}	c_{e+p}	c_{Had}	δ_{Had}
		(pb)	(%)	(%)	(%)	(%)	(%)	(%)	(%)	(%)	(%)	(%)	(%)	(%)	(%)						(%)
0.00	0.05	41.83	7.5	+3.1	+0.7	+0.8	−2.2	−0.1	+0.1	0.4	+1.8	1.0	2.7	0.5	0.4	1.207	0.839	0.914	0.816	0.796	3.1
0.05	0.10	61.94	7.2	+5.6	−0.2	+0.9	−2.5	+0.1	+3.4	1.1	−5.1	1.0	2.7	0.5	0.6	1.178	0.839	0.906	0.810	1.428	2.1
0.10	0.15	20.99	17.7	+5.7	−0.7	+0.8	−3.1	+0.3	−2.6	2.8	+4.7	1.0	2.7	0.5	0.9	1.164	0.839	0.900	0.795	1.263	6.1
0.15	0.22	9.517	26.3	+3.1	−1.0	−0.7	−3.1	−0.2	−2.5	3.3	+0.7	1.0	2.7	0.5	1.0	1.136	0.843	0.913	0.824	1.187	5.6
0.22	0.30	3.569	58.9	+3.1	−0.4	−1.6	−2.9	+0.3	−7.0	4.6	−8.0	1.0	2.7	0.5	1.3	1.149	0.827	0.892	0.826	1.123	3.1
0.30	0.40	5.991	22.9	+2.1	−1.9	+0.1	−0.3	−0.1	−9.5	4.3	−1.0	1.0	2.7	0.5	1.6	1.125	0.821	0.876	0.794	1.105	2.2
0.40	0.60	0.8913	48.2	+2.4	−0.7	+0.9	−2.2	+0.1	−10.5	2.7	+1.1	1.0	2.7	0.5	1.7	1.103	0.841	0.882	0.815	1.073	0.7
0.60	1.00	0.08044	130.8	+0.1	−0.7	−0.1	−1.0	−0.3	−12.5	2.3	+0.3	1.0	2.7	0.5	2.3	1.161	0.861	0.928	0.799	1.040	0.2

Table 34 Differential 1-jettiness cross sections for e^-p ($\mathcal{L} = 351.1\,\text{pb}^{-1}$) scattering in the range $3500 < Q^2 < 8000\,\text{GeV}^2$ and $0.40 < y < 0.70$, $d\sigma/d\tau_1^b$ [pb/$\Delta\tau_1^b$]. Further details are given in the caption of Table 2

Cross sections in e^-p ($\mathcal{L} = 351.1\,\text{pb}^{-1}$) for $3500 < Q^2 < 8000\,\text{GeV}^2$ and $0.40 < y < 0.70$ – $d\sigma/d\tau_1^b$ [pb/$\Delta\tau_1^b$]

τ_1^b range		Results $\frac{d\sigma}{d\tau_1^b}$	Uncertainties													Correction factors					
Min	Max		Stat	RCES	JES	HadTh	ElEn	ElTh	Model	MCstat	Unfold	ElecID	Lumi	Uncor	QED	c_{QED}	c_{NoZ}	c_{Born}	c_{e+p}	c_{Had}	δ_{Had}
		(pb)	(%)	(%)	(%)	(%)	(%)	(%)	(%)	(%)	(%)	(%)	(%)	(%)	(%)						(%)
0.00	0.05	41.57	6.7	+1.3	+0.7	+0.3	−1.2	+0.1	+0.4	0.3	+1.5	1.0	2.7	0.5	0.4	1.289	0.783	0.900	0.704	0.772	4.2
0.05	0.10	63.31	5.9	+3.0	−0.6	−0.3	−2.0	−0.0	+2.3	0.7	−2.3	1.0	2.7	0.5	0.6	1.244	0.790	0.904	0.729	1.386	0.8
0.10	0.15	20.92	14.2	+3.5	−0.7	−0.3	−2.6	−0.1	−5.6	1.5	−2.7	1.0	2.7	0.5	0.9	1.209	0.776	0.907	0.736	1.243	5.9
0.15	0.22	13.82	15.8	+3.2	+0.2	+0.5	−2.1	−0.1	−2.4	1.8	−0.6	1.0	2.7	0.5	1.0	1.250	0.754	0.890	0.725	1.169	4.4
0.22	0.30	4.551	33.6	+1.4	−1.2	−0.4	−1.7	−0.4	−4.7	2.5	+2.7	1.0	2.7	0.5	1.3	1.177	0.783	0.903	0.753	1.125	1.8
0.30	0.40	3.43	26.7	+2.3	−0.4	+0.2	−1.1	−0.3	−0.4	2.2	+0.7	1.0	2.7	0.5	1.5	1.171	0.767	0.901	0.768	1.094	1.4
0.40	0.60	1.331	24.8	+2.4	−0.3	+0.2	−2.5	−0.0	−1.8	1.6	−0.3	1.0	2.7	0.5	1.6	1.147	0.790	0.955	0.798	1.070	1.3
0.60	1.00	0.353	33.8	+1.7	−0.0	+0.2	−1.2	+0.2	−0.2	1.6	+0.1	1.0	2.7	0.5	1.8	1.212	0.794	0.914	0.794	1.037	0.1

Table 35 Differential 1-jettiness cross sections for e^-p ($\mathcal{L} = 351.1\,\text{pb}^{-1}$) scattering in the range $3500 < Q^2 < 8000\,\text{GeV}^2$ and $0.70 < y < 0.94$, $d\sigma/d\tau_1^b$ [pb/$\Delta\tau_1^b$]. Further details are given in the caption of Table 2

Cross sections in e^-p ($\mathcal{L} = 351.1\,\text{pb}^{-1}$) for $3500 < Q^2 < 8000\,\text{GeV}^2$ and $0.70 < y < 0.94$ – $d\sigma/d\tau_1^b$ [pb/$\Delta\tau_1^b$]

τ_1^b range		Results $\frac{d\sigma}{d\tau_1^b}$	Uncertainties													Correction factors					
Min	Max		Stat	RCES	JES	HadTh	ElEn	ElTh	Model	MCstat	Unfold	ElecID	Lumi	Uncor	QED	c_{QED}	c_{NoZ}	c_{Born}	c_{e+p}	c_{Had}	δ_{Had}
		(pb)	(%)	(%)	(%)	(%)	(%)	(%)	(%)	(%)	(%)	(%)	(%)	(%)	(%)						(%)
0.00	0.05	26.39	8.7	+0.6	+0.9	+0.1	−1.0	−0.0	+2.2	0.6	+0.5	1.0	2.7	0.5	0.6	1.318	0.749	0.908	0.650	0.758	3.8
0.05	0.10	29.39	9.6	+1.6	−0.3	−0.2	−0.7	−0.0	+5.2	0.9	−0.5	1.0	2.7	0.5	0.8	1.276	0.768	0.911	0.691	1.367	2.2
0.10	0.15	12.89	18.0	+2.4	−0.2	−0.3	−1.6	−0.0	+11.3	1.9	−5.7	1.0	2.7	0.5	1.2	1.210	0.796	0.922	0.755	1.229	5.2
0.15	0.22	6.352	24.9	+2.0	−0.4	−0.6	−1.1	−0.3	+4.4	2.2	−0.0	1.0	2.7	0.5	1.3	1.204	0.782	0.924	0.723	1.173	5.4
0.22	0.30	4.442	26.1	+2.7	+1.1	−0.3	−1.9	+0.6	+31.7	3.7	+5.7	1.0	2.7	0.5	1.6	1.226	0.779	0.884	0.712	1.122	0.3
0.30	0.40	0.7486	67.3	+1.2	+0.5	+1.0	−1.4	+0.3	+5.7	3.1	+1.9	1.0	2.7	0.5	2.0	1.166	0.785	0.941	0.750	1.092	3.0
0.40	0.60	0.8548	32.1	+3.3	+0.0	+0.0	−1.4	−0.3	+16.9	2.6	+0.9	1.0	2.7	0.5	2.0	1.218	0.736	0.907	0.739	1.078	0.4
0.60	1.00	0.3377	28.6	+0.4	+0.2	+0.9	−0.9	+0.3	+10.2	3.6	−0.4	1.0	2.7	0.5	2.3	1.258	0.751	0.853	0.735	1.040	0.6

Table 36 Differential 1-jettiness cross sections for e^-p ($\mathcal{L} = 351.1\,\text{pb}^{-1}$) scattering in the range $8000 < Q^2 < 20000\,\text{GeV}^2$ and $0.20 < y < 0.94$, $d\sigma/d\tau_1^b$ [pb/$\Delta\tau_1^b$]. Further details are given in the caption of Table 2

Cross sections in e^-p ($\mathcal{L} = 351.1\,\text{pb}^{-1}$) for $8000 < Q^2 < 20000\,\text{GeV}^2$ and $0.20 < y < 0.94$ – $d\sigma/d\tau_1^b$ [pb/$\Delta\tau_1^b$]

τ_1^b range		Results	Uncertainties												Correction factors					
Min	Max	$\frac{d\sigma}{d\tau_1^b}$	Stat	RCES	JES	HadTh	ElEn	ElTh	Model	MCstat	Unfold	ElecID	Lumi	Uncor	QED	c_QED	c_NoZ	c_Born	$c_\text{e+p}$	c_Had	δ_Had
		(pb)	(%)	(%)	(%)	(%)	(%)	(%)	(%)	(%)	(%)	(%)	(%)	(%)	(%)						(%)
0.00	0.05	60.77	5.8	+3.4	+0.5	+0.6	−2.8	−0.4	−0.1	0.3	+0.6	1.0	2.7	0.5	0.6	1.464	0.630	0.905	0.525	0.894	3.2
0.05	0.10	34.91	10.8	+5.1	−0.6	+0.7	−3.3	−0.2	+4.0	1.2	+3.1	1.0	2.7	0.5	1.2	1.400	0.639	0.945	0.510	1.271	6.0
0.10	0.15	9.962	37.0	+4.9	−0.5	−0.0	−3.4	−1.3	−0.8	3.3	−9.0	1.0	2.7	0.5	1.8	1.440	0.618	0.906	0.515	1.179	5.6
0.15	0.22	6.054	39.3	+2.6	−0.9	−0.6	−4.2	−0.3	+0.4	4.1	−10.3	1.0	2.7	0.5	2.1	1.340	0.681	0.977	0.546	1.124	2.4
0.22	0.30	4.378	36.6	+7.0	+0.3	+2.4	−3.3	−1.1	−0.0	4.8	−3.6	1.0	2.7	0.5	2.7	1.464	0.591	0.820	0.516	1.075	2.2
0.30	0.40	0.7655	109.2	+2.9	−0.3	+0.3	+0.4	−0.1	−5.8	5.0	+5.4	1.0	2.7	0.5	3.4	1.414	0.627	0.934	0.522	1.058	1.8
0.40	0.60	0.5905	50.7	+1.4	−0.1	+1.6	−1.8	+0.1	−0.1	4.6	+3.4	1.0	2.7	0.5	3.7	1.355	0.687	0.988	0.618	1.020	0.2
0.60	1.00	0.1414	54.2	+3.7	+1.1	−1.6	−3.9	−0.7	+27.0	3.9	−1.6	1.0	2.7	0.5	5.0	1.480	0.652	0.917	0.467	1.071	1.5
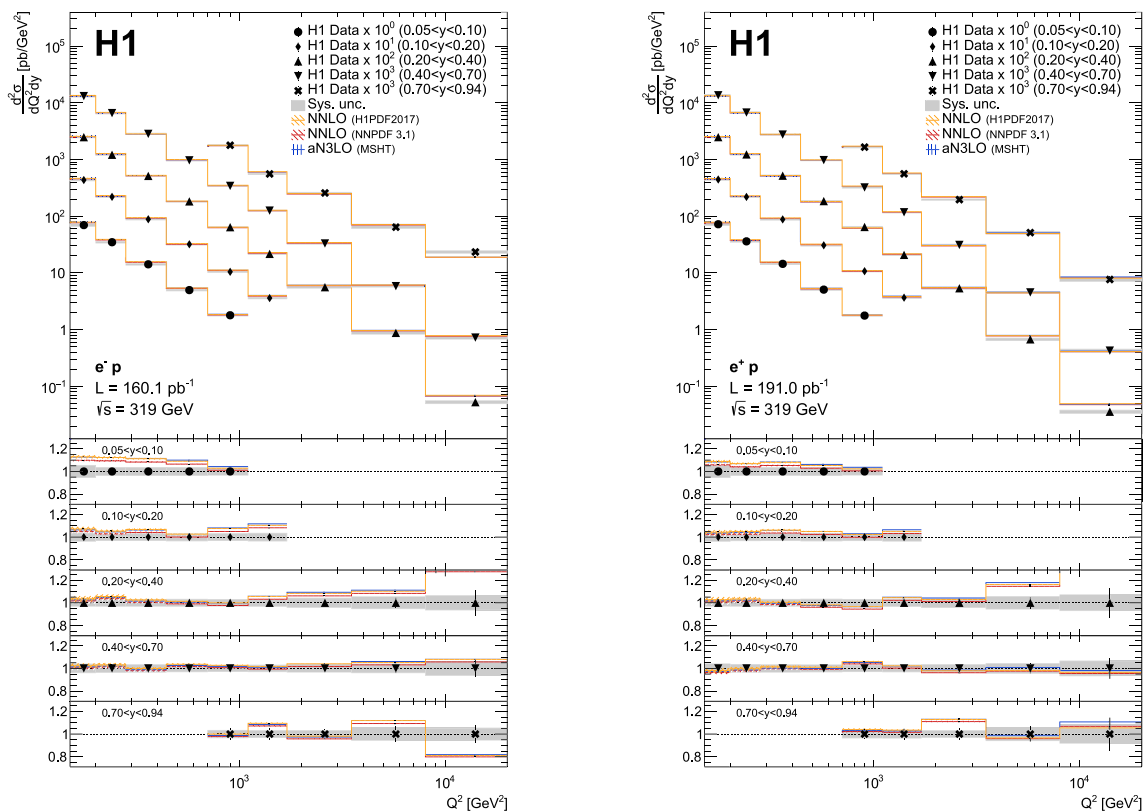
Fig. 13 The double-differential inclusive neutral current DIS cross section $\frac{d^2\sigma_{\text{NC DIS}}}{dQ^2\,dy}$ for e^-p (left) and e^+p (right) scattering in the kinematic region $150 \leq Q^2 < 20\,000\,\text{GeV}^2$ and $0.05 \leq y < 0.94$. The data are displayed as full circles, the vertical error bars indicate statistical uncertainties, while systematic uncertainties are displayed as shaded area. Different y ranges are indicated by different markers, and are displaced vertically by a constant factor as indicated in the legend. The vertical error bars indicate statistical uncertainties, whereas systematic experimental uncertainties are displayed as shaded area. The data are compared to NNLO and a3NLO predictions. The orange line indicates NNLO predictions using the H1PDF2017NNLO PDF set, the red line NNLO predictions using the NNPDF 3.1 PDF set, and the blue line indicates predictions in aN3LO accuracy using the MSHT PDF set. The hatched area indicates associated theoretical uncertainties from scale variations and PDF uncertainties

Table 37 Double-differential neutral current DIS cross sections for $e^- p$ scattering, $\mathrm{d}^2\sigma/\mathrm{d}Q^2\mathrm{d}y$ [pb]. The lower bin edges in y and Q^2 are indicated. Further details are given in the caption of Table 2

2D neutral current DIS in $e^- p$ cross sections $\mathrm{d}^2\sigma/\mathrm{d}Q^2\mathrm{d}y$ [pb/GeV^2]

y	Q^2	Results	Uncertainties													Correction factors					
Min	Min	$\frac{\mathrm{d}^2\sigma}{\mathrm{d}Q^2\mathrm{d}y}$	Stat	RCES	JES	HadTh	ElEn	ElTh	Model	MCstat	Unfold	ElecID	Lumi	Uncor	QED	c_{QED}	c_{NoZ}	c_{Born}	$c_{\mathrm{e+p}}$	c_{Had}	δ_{Had}
	(GeV)	(pb/GeV^2)	(%)	(%)	(%)	(%)	(%)	(%)	(%)	(%)	(%)	(%)	(%)	(%)	(%)						(%)
0.05	150	174.3	2.9	+2.1	+0.7	+0.8	+3.8	+1.3	+0.9	0.5	−0.0	0.2	2.7	0.5	0.2	1.067	0.999	0.922	0.999	1.000	0.0
0.05	200	139.3	1.6	+1.6	+0.3	+0.3	−1.6	+0.7	−0.3	0.2	−0.1	0.2	2.7	0.5	0.2	1.071	0.992	0.911	0.995	1.000	0.0
0.05	280	113.6	1.7	+1.6	+0.2	+0.3	−1.7	+0.7	−0.2	0.2	+0.0	0.2	2.7	0.5	0.2	1.066	0.993	0.912	0.992	1.000	0.0
0.05	440	64.84	2.2	+1.3	+0.2	+0.1	−2.0	+0.4	+0.3	0.2	−0.1	0.2	2.7	0.5	0.2	1.064	0.991	0.910	0.991	1.000	0.0
0.05	700	35.93	2.4	+0.7	+0.1	−0.3	−1.3	+0.3	−1.1	0.2	−0.0	0.2	2.7	0.5	0.3	1.069	0.981	0.902	0.983	1.000	0.0
0.10	150	217.3	1.5	+1.4	+0.4	+0.2	+1.8	+0.8	+0.5	0.2	−0.0	0.2	2.7	0.5	0.2	1.073	0.994	0.919	0.997	1.000	0.0
0.10	200	175.6	1.2	+0.8	+0.1	−0.0	−1.3	+0.7	+0.2	0.1	−0.0	0.2	2.7	0.5	0.2	1.073	0.993	0.915	0.993	1.000	0.0
0.10	280	141.5	1.2	+1.0	+0.1	+0.0	−1.1	+0.6	+0.1	0.1	−0.0	0.2	2.7	0.5	0.1	1.067	0.991	0.911	0.992	1.000	0.0
0.10	440	83.26	1.6	+1.2	+0.1	+0.1	−1.6	+0.5	−0.0	0.1	−0.0	0.2	2.7	0.5	0.2	1.070	0.987	0.906	0.987	1.000	0.0
0.10	700	41.88	2.1	+1.2	−0.0	+0.0	−1.1	+0.4	+0.2	0.1	−0.0	0.2	2.7	0.5	0.2	1.063	0.978	0.907	0.979	1.000	0.0
0.10	1100	21.64	2.8	+1.5	+0.1	+0.0	−1.4	+0.2	−0.8	0.1	−0.1	0.2	2.7	0.5	0.2	1.068	0.968	0.902	0.970	1.000	0.0
0.20	150	247.6	1.0	+0.8	+0.3	+0.0	−0.3	+0.7	+0.9	0.1	+0.0	0.2	2.7	0.5	0.1	1.072	0.996	0.918	0.996	1.000	0.0
0.20	200	193.9	1.1	+0.6	+0.0	−0.0	−1.0	+0.7	+1.0	0.1	−0.0	0.2	2.7	0.5	0.1	1.071	0.994	0.916	0.994	1.000	0.0
0.20	280	164.4	1.1	+0.7	+0.1	−0.0	−1.1	+0.5	+0.6	0.1	−0.0	0.2	2.7	0.5	0.1	1.069	0.993	0.913	0.992	1.000	0.0
0.20	440	94.95	1.5	+0.9	+0.0	−0.1	−1.3	+0.4	+0.3	0.1	−0.0	0.2	2.7	0.5	0.1	1.069	0.987	0.908	0.986	1.000	0.0
0.20	700	51.29	1.8	+0.8	−0.0	−0.1	−0.9	+0.3	+0.3	0.1	−0.0	0.2	2.7	0.5	0.2	1.068	0.975	0.906	0.974	1.000	0.0
0.20	1100	26.03	2.5	+1.2	−0.0	−0.0	−1.3	+0.3	+0.1	0.1	−0.0	0.2	2.7	0.5	0.2	1.066	0.956	0.903	0.953	1.000	0.0
0.20	1700	20.2	3.0	+2.3	+0.0	+0.1	−1.9	+0.0	−1.1	0.2	−0.2	0.2	2.7	0.5	0.2	1.066	0.918	0.900	0.908	1.000	0.0
0.20	3500	7.902	4.4	+3.8	+0.0	+0.6	−2.3	−0.0	−0.3	0.2	−0.3	1.0	2.7	0.5	0.4	1.060	0.838	0.908	0.812	1.000	0.0
0.20	8000	1.266	11.4	+4.2	−0.0	+1.1	−3.6	−0.3	+0.2	0.5	−0.7	1.0	2.7	0.5	0.8	1.059	0.741	0.917	0.689	1.000	0.0
0.40	150	196.5	1.3	−0.6	−1.2	−0.1	−0.6	+0.5	+2.4	0.1	−0.0	0.2	2.7	0.5	0.1	1.074	0.993	0.918	0.994	1.000	0.0
0.40	200	157.7	1.3	−0.4	−0.7	−0.1	−0.5	+0.4	+2.2	0.1	−0.0	0.2	2.7	0.5	0.1	1.072	0.992	0.914	0.993	1.000	0.0
0.40	280	135.7	1.4	−0.3	−0.4	−0.1	−0.7	+0.4	+1.8	0.1	−0.0	0.2	2.7	0.5	0.1	1.071	0.989	0.910	0.990	1.000	0.0
0.40	440	75.34	1.8	+0.2	−0.2	−0.1	−0.8	+0.3	+1.1	0.1	−0.0	0.2	2.7	0.5	0.1	1.069	0.986	0.909	0.986	1.000	0.0
0.40	700	41.08	2.1	+0.3	−0.1	−0.1	−0.7	+0.3	+0.6	0.1	−0.0	0.2	2.7	0.5	0.2	1.068	0.975	0.905	0.971	1.000	0.0
0.40	1100	22.59	2.9	+0.7	−0.1	−0.1	−0.9	+0.2	+0.5	0.2	−0.0	0.2	2.7	0.5	0.2	1.071	0.953	0.900	0.943	1.000	0.0
0.40	1700	17.86	3.1	+1.4	−0.0	−0.0	−1.0	+0.1	+0.6	0.2	−0.2	0.2	2.7	0.5	0.3	1.065	0.905	0.902	0.889	1.000	0.0
0.40	3500	7.9	4.1	+2.1	−0.0	+0.0	−1.6	−0.0	−0.1	0.2	−0.0	1.0	2.7	0.5	0.4	1.066	0.782	0.903	0.725	1.000	0.0
0.40	8000	2.612	7.5	+4.4	+0.0	+0.5	−3.2	−0.6	−1.2	0.3	−0.1	1.0	2.7	0.5	0.7	1.069	0.633	0.915	0.523	1.000	0.0
0.70	700	21.4	4.8	−1.7	−0.5	−0.1	+0.3	+0.1	+0.9	0.3	−0.1	0.2	2.7	0.5	0.2	1.072	0.972	0.904	0.970	1.000	0.0
0.70	1100	10.68	5.1	−0.3	−0.2	+0.1	+0.1	+0.2	+1.6	0.3	−0.2	0.2	2.7	0.5	0.3	1.067	0.952	0.906	0.949	1.000	0.0
0.70	1700	9.873	4.3	+0.3	−0.1	−0.1	−0.2	+0.2	+1.6	0.3	−0.1	0.2	2.7	0.5	0.4	1.061	0.905	0.903	0.881	1.000	0.0
0.70	3500	4.002	6.4	+1.3	+0.0	−0.1	−0.9	−0.0	+4.5	0.4	−0.2	1.0	2.7	0.5	0.5	1.061	0.764	0.910	0.690	1.000	0.0
0.70	8000	2.249	8.0	+1.9	+0.1	−0.0	−1.3	−0.3	+3.7	0.5	−0.8	1.0	2.7	0.5	0.8	1.057	0.600	0.911	0.440	1.000	0.0

Table 38 Double-differential neutral current DIS cross sections for $e^+ p$ scattering, $d^2\sigma/dQ^2dy$ [pb]. The lower bin edges in y and Q^2 are indicated. Further details are given in the caption of Table 2

2D neutral current DIS in $e^+ p$ cross sections $d^2\sigma/dQ^2dy$ [pb/GeV^2]

y Min	Q^2 Min (GeV)	Results $\frac{d^2\sigma}{dQ^2dy}$ (pb/GeV^2)	Uncertainties Stat (%)	RCES (%)	JES (%)	HadTh (%)	ElEn (%)	ElTh (%)	Model (%)	MCstat (%)	SysTauData (%)	ElecID (%)	Lumi (%)	Uncor (%)	QED (%)	Correction factors c_{QED}	c_{NoZ}	c_{Born}	c_{e+p}	c_{Had}	δ_{Had} (%)
0.05	150	180.5	2.7	+2.2	+0.6	+0.9	+3.9	+1.3	−0.3	0.4	+0.0	0.2	2.7	0.5	0.2	1.070	0.996	0.924	1.000	1.000	0.0
0.05	200	144.3	1.5	+1.7	+0.4	+0.3	−1.6	+0.7	+0.1	0.2	−0.1	0.2	2.7	0.5	0.2	1.070	0.994	0.923	1.000	1.000	0.0
0.05	280	115.7	1.5	+1.6	+0.2	+0.3	−1.5	+0.7	+0.1	0.2	−0.0	0.2	2.7	0.5	0.2	1.064	0.998	0.919	1.000	1.000	0.0
0.05	440	66.09	1.9	+1.3	+0.2	+0.1	−2.1	+0.4	−0.4	0.2	+0.1	0.2	2.7	0.5	0.2	1.063	0.997	0.919	1.000	1.000	0.0
0.05	700	35.45	2.1	+0.5	+0.1	−0.4	−1.2	+0.3	−1.0	0.2	−0.1	0.2	2.7	0.5	0.3	1.069	0.995	0.909	1.000	1.000	0.0
0.10	150	222	1.4	+1.5	+0.4	+0.2	+1.8	+0.8	+0.8	0.2	−0.0	0.2	2.7	0.5	0.1	1.073	0.994	0.923	1.000	1.000	0.0
0.10	200	175	1.1	+0.9	+0.1	−0.0	−1.4	+0.8	−0.0	0.1	+0.0	0.2	2.7	0.5	0.1	1.069	0.997	0.920	1.000	1.000	0.0
0.10	280	140.6	1.2	+1.1	+0.1	+0.1	−1.2	+0.5	+0.1	0.1	−0.0	0.2	2.7	0.5	0.1	1.064	0.996	0.918	1.000	1.000	0.0
0.10	440	79.87	1.5	+1.3	+0.0	+0.0	−1.6	+0.5	−0.1	0.1	−0.0	0.2	2.7	0.5	0.2	1.066	0.997	0.916	1.000	1.000	0.0
0.10	700	42.95	1.9	+1.3	−0.0	+0.0	−1.1	+0.4	+0.0	0.1	+0.0	0.2	2.7	0.5	0.2	1.062	0.996	0.915	1.000	1.000	0.0
0.10	1100	22	2.5	+1.5	+0.1	−0.0	−1.6	+0.2	−0.9	0.1	−0.1	0.2	2.7	0.5	0.2	1.070	0.995	0.904	1.000	1.000	0.0
0.20	150	248	0.9	+0.8	+0.3	+0.0	−0.3	+0.7	+0.8	0.1	−0.0	0.2	2.7	0.5	0.1	1.074	0.997	0.923	1.000	1.000	0.0
0.20	200	196.6	1.0	+0.7	+0.0	−0.0	−1.0	+0.6	+0.7	0.1	−0.0	0.2	2.7	0.5	0.1	1.070	0.997	0.921	1.000	1.000	0.0
0.20	280	165.9	1.0	+0.8	+0.0	−0.0	−1.1	+0.5	+0.6	0.1	−0.0	0.2	2.7	0.5	0.1	1.068	0.998	0.919	1.000	1.000	0.0
0.20	440	96.09	1.3	+1.0	+0.0	−0.1	−1.4	+0.5	+0.4	0.1	−0.0	0.2	2.7	0.5	0.1	1.067	0.998	0.917	1.000	1.000	0.0
0.20	700	51.72	1.6	+1.0	+0.0	−0.0	−0.9	+0.3	+0.6	0.1	−0.0	0.2	2.7	0.5	0.2	1.066	0.999	0.911	1.000	1.000	0.0
0.20	1100	24.99	2.3	+1.4	−0.0	−0.0	−1.3	+0.3	−0.1	0.1	−0.0	0.2	2.7	0.5	0.2	1.062	1.000	0.912	1.000	1.000	0.0
0.20	1700	19.34	2.7	+2.4	+0.0	+0.1	−2.1	+0.1	−0.9	0.1	−0.3	0.2	2.7	0.5	0.2	1.066	1.009	0.902	1.000	1.000	0.0
0.20	3500	6.077	4.7	+4.0	−0.0	+0.6	−2.5	−0.0	−0.7	0.2	−0.3	1.0	2.7	0.5	0.4	1.068	1.029	0.905	1.000	1.000	0.0
0.20	8000	0.8582	13.1	+4.7	+0.1	+1.1	−4.1	−0.5	−0.5	0.5	−0.1	1.0	2.7	0.5	1.0	1.076	1.072	0.889	1.000	1.000	0.0
0.40	150	203.2	1.2	−0.6	−1.2	−0.1	−0.6	+0.5	+2.6	0.1	−0.0	0.2	2.7	0.5	0.1	1.073	0.996	0.924	1.000	1.000	0.0
0.40	200	161.4	1.2	−0.4	−0.7	−0.1	−0.5	+0.4	+2.1	0.1	−0.0	0.2	2.7	0.5	0.1	1.069	0.996	0.922	1.000	1.000	0.0
0.40	280	132	1.3	−0.2	−0.4	−0.1	−0.7	+0.4	+1.7	0.1	−0.0	0.2	2.7	0.5	0.1	1.068	0.996	0.918	1.000	1.000	0.0
0.40	440	76.04	1.6	+0.3	−0.2	−0.1	−0.8	+0.3	+1.3	0.1	−0.0	0.2	2.7	0.5	0.1	1.071	0.997	0.914	1.000	1.000	0.0
0.40	700	38.58	1.9	+0.4	−0.1	−0.1	−0.8	+0.3	+0.7	0.1	−0.0	0.2	2.7	0.5	0.2	1.066	1.002	0.912	1.000	1.000	0.0
0.40	1100	21.12	2.7	+0.9	−0.0	−0.1	−1.1	+0.2	+0.5	0.2	−0.1	0.2	2.7	0.5	0.2	1.064	1.007	0.909	1.000	1.000	0.0
0.40	1700	16.83	3.0	+1.7	−0.0	−0.0	−1.2	+0.1	+0.4	0.2	−0.1	0.2	2.7	0.5	0.3	1.072	1.016	0.899	1.000	1.000	0.0
0.40	3500	6.128	4.3	+2.5	−0.0	+0.0	−1.9	−0.1	−0.9	0.2	−0.5	1.0	2.7	0.5	0.4	1.062	1.076	0.898	1.000	1.000	0.0
0.40	8000	1.538	9.2	+4.7	−0.1	+0.4	−3.2	−0.3	−1.2	0.5	−0.8	1.0	2.7	0.5	0.9	1.066	1.206	0.898	1.000	1.000	0.0
0.70	700	19.83	4.5	−1.8	−0.5	−0.1	+0.3	+0.1	+1.1	0.3	−0.0	0.2	2.7	0.5	0.2	1.071	0.999	0.913	1.000	1.000	0.0
0.70	1100	10.73	4.7	−0.3	−0.2	−0.0	+0.1	+0.1	+2.3	0.3	−0.0	0.2	2.7	0.5	0.3	1.070	1.000	0.904	1.000	1.000	0.0
0.70	1700	7.528	4.6	+0.3	−0.2	−0.1	−0.3	+0.2	+1.3	0.3	−0.3	0.2	2.7	0.5	0.4	1.063	1.024	0.900	1.000	1.000	0.0
0.70	3500	3.205	6.6	+1.4	+0.3	−0.0	−1.1	+0.1	+4.8	0.5	−0.3	1.0	2.7	0.5	0.6	1.050	1.104	0.901	1.000	1.000	0.0
0.70	8000	0.7364	14.5	+2.8	+0.4	+0.0	−2.3	−0.7	+6.3	1.1	−1.4	1.0	2.7	0.5	1.2	1.090	1.360	0.896	1.000	1.000	0.0

References

1. H. Abramowicz, A. Caldwell, Rev. Mod. Phys. **71**, 1275–1410 (1999). https://doi.org/10.1103/RevModPhys.71.1275. arXiv:hep-ex/9903037

2. M. Klein, R. Yoshida, Prog. Part. Nucl. Phys. **61**, 343–393 (2008). https://doi.org/10.1016/j.ppnp.2008.05.002. arXiv:0805.3334

3. P. Newman, M. Wing, Rev. Mod. Phys. **86**, 1037 (2014). https://doi.org/10.1103/RevModPhys.86.1037. arXiv:1308.3368

4. F. Gross et al., Eur. Phys. J. C **83**, 1125 (2023). https://doi.org/10.1140/epjc/s10052-023-11949-2. arXiv:2212.11107

5. ALEPH Collaboration, D. Buskulic et al., Z. Phys. C **73**, 409–420 (1997). https://doi.org/10.1007/s002880050330

6. ALEPH Collaboration, A. Heister et al., Eur. Phys. J. C 35, 457–486 (2004). https://doi.org/10.1140/epjc/s2004-01891-4

7. L3 Collaboration, M. Acciarri et al., Phys. Lett. B **371**, 137–148 (1996). https://doi.org/10.1016/0370-2693(96)00096-2

8. L3 Collaboration, M. Acciarri et al., Phys. Lett. B **404**, 390–402 (1997). https://doi.org/10.1016/S0370-2693(97)00647-3

9. L3 Collaboration, M. Acciarri et al., Phys. Lett. B **444**, 569–582 (1998). https://doi.org/10.1016/S0370-2693(98)01404-X

10. L3 Collaboration, P. Achard et al., Phys. Lett. B **536**, 217–228 (2002). https://doi.org/10.1016/S0370-2693(02)01814-2. arXiv:hep-ex/0206052

11. L3 Collaboration, P. Achard et al., Phys. Rep. **399**, 71–174 (2004). https://doi.org/10.1016/j.physrep.2004.07.002. arXiv:hep-ex/0406049

12. DELPHI Collaboration, P. Abreu et al., Phys. Lett. B **456**, 322–340 (1999). https://doi.org/10.1016/S0370-2693(99)00472-4

13. DELPHI Collaboration, J. Abdallah et al., Eur. Phys. J. C **29**, 285–312 (2003). https://doi.org/10.1140/epjc/s2003-01198-0. arXiv:hep-ex/0307048

14. DELPHI Collaboration, J. Abdallah et al., Eur. Phys. J. C **37**, 1–23 (2004). https://doi.org/10.1140/epjc/s2004-01889-x. arXiv:hep-ex/0406011

15. S.L.D. Collaboration, K. Abe et al., Phys. Rev. D **51**, 962–984 (1995). https://doi.org/10.1103/PhysRevD.51.962. arXiv:hep-ex/9501003

16. JADE Collaboration, P.A. Movilla Fernandez, O. Biebel, S. Bethke, S. Kluth, P. Pfeifenschneider, Eur. Phys. J. C **1**, 461–478 (1998). https://doi.org/10.1007/s100520050096. arXiv:hep-ex/9708034

17. JADE Collaboration, O. Biebel, P.A. Movilla Fernandez, S. Bethke, Phys. Lett. B **459**, 326–334 (1999). https://doi.org/10.1016/S0370-2693(99)00733-9. arXiv:hep-ex/9903009

18. JADE, OPAL Collaboration, P. Pfeifenschneider et al., Eur. Phys. J. C **17**, 19–51 (2000). https://doi.org/10.1007/s100520000432. arXiv:hep-ex/0001055

19. P.A. Movilla Fernandez, S. Bethke, O. Biebel, S. Kluth, Eur. Phys. J. C **22**, 1–15 (2001). https://doi.org/10.1007/s100520100750. arXiv:hep-ex/0105059

20. JADE Collaboration, C. Pahl, S. Bethke, S. Kluth, J. Schieck, Eur. Phys. J. C **60**, 181–196 (2009). https://doi.org/10.1140/epjc/s10052-009-0930-5 (Erratum: Eur. Phys. J. C 62, 451–452 (2009)). arXiv:0810.2933

21. CELLO Collaboration, H.J. Behrend et al., Z. Phys. C **44**, 63 (1989). https://doi.org/10.1007/BF01548583

22. C.D.F. Collaboration, T. Aaltonen et al., Phys. Rev. D **83**, 112007 (2011). https://doi.org/10.1103/PhysRevD.83.112007. arXiv:1103.5143

23. C.M.S. Collaboration, V. Khachatryan et al., Phys. Lett. B **699**, 48–67 (2011). https://doi.org/10.1016/j.physletb.2011.03.060. arXiv:1102.0068

24. ALICE Collaboration, B. Abelev et al., Eur. Phys. J. C **72**, 2124 (2012). https://doi.org/10.1140/epjc/s10052-012-2124-9. arXiv:1205.3963

25. ATLAS Collaboration, G. Aad et al., Eur. Phys. J. C **72**, 2211 (2012). https://doi.org/10.1140/epjc/s10052-012-2211-y. arXiv:1206.2135

26. C.M.S. Collaboration, S. Chatrchyan et al., Phys. Lett. B **722**, 238–261 (2013). https://doi.org/10.1016/j.physletb.2013.04.025. arXiv:1301.1646

27. C.M.S. Collaboration, V. Khachatryan et al., JHEP **10**, 087 (2014). https://doi.org/10.1007/JHEP10(2014)087. arXiv:1407.2856

28. ATLAS Collaboration, G. Aad et al., Eur. Phys. J. C **76**, 375 (2016). https://doi.org/10.1140/epjc/s10052-016-4176-8. arXiv:1602.08980

29. CMS Collaboration, A.M. Sirunyan et al., JHEP **12**, 117 (2018). https://doi.org/10.1007/JHEP12(2018)117. arXiv:1811.00588

30. ATLAS Collaboration, G. Aad et al., JHEP **01**, 188 (2021). https://doi.org/10.1007/JHEP01(2021)188 (Erratum: JHEP 12, 053 (2021)). arXiv:2007.12600

31. M. Alvarez, J. Cantero, M. Czakon, J. Llorente, A. Mitov, R. Poncelet, JHEP **03**, 129 (2023). https://doi.org/10.1007/JHEP03(2023)129. arXiv:2301.01086

32. ATLAS Collaboration, G. Aad et al., JHEP **07**, 085 (2023). https://doi.org/10.1007/JHEP07(2023)085. arXiv:2301.09351

33. H1 Collaboration, C. Adloff et al., Phys. Lett. B **406**, 256–270 (1997). https://doi.org/10.1016/S0370-2693(97)00754-5. arXiv:hep-ex/9706002

34. H1 Collaboration, C. Adloff et al., Eur. Phys. J. C **14**, 255–269 (2000). https://doi.org/10.1007/s100520000344 (Erratum: Eur. Phys. J. C 18, 417–419 (2000)). arXiv:hep-ex/9912052

35. Z.E.U.S. Collaboration, S. Chekanov et al., Eur. Phys. J. C **27**, 531–545 (2003). https://doi.org/10.1140/epjc/s2003-01148-x. arXiv:hep-ex/0211040

36. H1 Collaboration, C. Adloff et al., Eur. Phys. J. C **19**, 289 (2001). https://doi.org/10.1007/s100520100621. arXiv:hep-ex/0010054

37. Z.E.U.S. Collaboration, S. Chekanov et al., Nucl. Phys. B **767**, 1–28 (2007). https://doi.org/10.1016/j.nuclphysb.2006.05.016. arXiv:hep-ex/0604032

38. S. Kluth, Rep. Prog. Phys. **69**, 1771–1846 (2006). https://doi.org/10.1088/0034-4885/69/6/R04. arXiv:hep-ex/0603011

39. T. Becher, M.D. Schwartz, JHEP **07**, 034 (2008). https://doi.org/10.1088/1126-6708/2008/07/034. arXiv:0803.0342

40. R. Abbate, M. Fickinger, A.H. Hoang, V. Mateu, I.W. Stewart, Phys. Rev. D **83**, 074021 (2011). https://doi.org/10.1103/PhysRevD.83.074021. arXiv:1006.3080

41. M. Steinhauser, P. Marquard, eds., *Proceedings of: Loops and Legs in Quantum Field Theory 2022 (LL2022)*. Oct 2022. https://pos.sissa.it/416. PoS(LL2022), C22-04-25.3

42. M. Dasgupta, G.P. Salam, Phys. Lett. B **512**, 323–330 (2001). https://doi.org/10.1016/S0370-2693(01)00725-0. arXiv:hep-ph/0104277

43. M. Dasgupta, G.P. Salam, J. Phys. G **30**, R143 (2004). https://doi.org/10.1088/0954-3899/30/5/R01. arXiv:hep-ph/0312283

44. S. Brandt, C. Peyrou, R. Sosnowski, A. Wroblewski, Phys. Lett. **12**, 57–61 (1964). https://doi.org/10.1016/0031-9163(64)91176-X

45. E. Farhi, Phys. Rev. Lett. **39**, 1587–1588 (1977). https://doi.org/10.1103/PhysRevLett.39.1587

46. R.P. Feynman, Photon–hadron interactions. Frontiers in Physics. Benjamin, Reading (1973). https://bib-pubdb1.desy.de/record/356451. Reading (1972)

47. K.H. Streng, T.F. Walsh, P.M. Zerwas, Z. Phys. C **2**, 237 (1979). https://doi.org/10.1007/BF01474667 (DESY-79-10)

48. C. Bouchiat, P. Meyer, M. Mezard, Nucl. Phys. B **169**, 189–215 (1980). https://doi.org/10.1016/0550-3213(80)90029-2

49. B.R. Webber, Hadronic final states, in *3rd Workshop on Deep Inelastic Scattering and QCD (DIS 95)*. 4 (1995). arXiv:hep-ph/9510283

50. D. Graudenz, Deeply inelastic hadronic final states: QCD corrections, in *Ringberg Workshop on New Trends in HERA Physics 1997* 8 (1997). p. 146–160. arXiv:hep-ph/9708362

51. M. Dasgupta, B.R. Webber, Eur. Phys. J. C **1**, 539–546 (1998). https://doi.org/10.1007/s100520050103. arXiv:hep-ph/9704297

52. M. Dasgupta, B.R. Webber, JHEP **10**, 001 (1998). https://doi.org/10.1088/1126-6708/1998/10/001. arXiv:hep-ph/9809247

53. V. Antonelli, M. Dasgupta, G.P. Salam, JHEP **02**, 001 (2000). https://doi.org/10.1088/1126-6708/2000/02/001. arXiv:hep-ph/9912488

54. M. Dasgupta, G.P. Salam, JHEP **08**, 032 (2002). https://doi.org/10.1088/1126-6708/2002/08/032. arXiv:hep-ph/0208073

55. T. Gehrmann, A. Huss, J. Mo, J. Niehues, Eur. Phys. J. C **79**, 1022 (2019). https://doi.org/10.1140/epjc/s10052-019-7528-3. arXiv:1909.02760

56. A. Banfi, G.P. Salam, G. Zanderighi, Phys. Lett. B **584**, 298–305 (2004). https://doi.org/10.1016/j.physletb.2004.01.048. arXiv:hep-ph/0304148

57. A. Banfi, G.P. Salam, G. Zanderighi, JHEP **03**, 073 (2005). https://doi.org/10.1088/1126-6708/2005/03/073. arXiv:hep-ph/0407286

58. G. Zanderighi, A. Banfi, G.P. Salam, CAESAR—Computer Automated Expert Semi-Analytical Resummer (2004). http://home.fnal.gov/~zanderi/Caesar/caesar.html

59. I.W. Stewart, F.J. Tackmann, W.J. Waalewijn, Phys. Rev. Lett. **105**, 092002 (2010). https://doi.org/10.1103/PhysRevLett.105.092002. arXiv:1004.2489

60. D. Kang, C. Lee, I.W. Stewart, Phys. Rev. D **88**, 054004 (2013). https://doi.org/10.1103/PhysRevD.88.054004. arXiv:1303.6952

61. D. Kang, C. Lee, I.W. Stewart, JHEP **11**, 132 (2014). https://doi.org/10.1007/JHEP11(2014)132. arXiv:1407.6706

62. T.T. Jouttenus, I.W. Stewart, F.J. Tackmann, W.J. Waalewijn, Phys. Rev. D **83**, 114030 (2011). https://doi.org/10.1103/PhysRevD.83.114030. arXiv:1102.4344

63. Z.-B. Kang, S. Mantry, J.-W. Qiu, Phys. Rev. D **86**, 114011 (2012). https://doi.org/10.1103/PhysRevD.86.114011. arXiv:1204.5469

64. Z.-B. Kang, X. Liu, S. Mantry, Phys. Rev. D **90**, 014041 (2014). https://doi.org/10.1103/PhysRevD.90.014041. arXiv:1312.0301

65. H. Cao, Z.-B. Kang, X. Liu, S. Mantry, arXiv:2401.01941

66. H1 Collaboration, F.D. Aaron et al., Eur. Phys. J. C **72**, 2163 (2012). https://doi.org/10.1140/epjc/s10052-012-2163-2 (Erratum: Eur. Phys. J. C 74, 2733 (2012)). arXiv:1205.2448

67. H1 Collaboration, I. Abt et al., The H1 detector at HERA. DESY-93-103 (1993)

68. H1 Calorimeter Group Collaboration, B. Andrieu et al., Nucl. Instrum. Methods A **336**, 460–498 (1993). https://doi.org/10.1016/0168-9002(93)91257-N

69. H1 Collaboration, I. Abt et al., Nucl. Instrum. Methods A **386**, 310–347 (1997). https://doi.org/10.1016/S0168-9002(96)00893-5

70. H1 Collaboration, I. Abt et al., Nucl. Instrum. Methods A **386**, 348–396 (1997). https://doi.org/10.1016/S0168-9002(96)00894-7

71. H1 SPACAL Group Collaboration, R.D. Appuhn et al., Nucl. Instrum. Methods A **386**, 397–408 (1997). https://doi.org/10.1016/S0168-9002(96)01171-0

72. D. Pitzl et al., Nucl. Instrum. Methods A **454**, 334–349 (2000). https://doi.org/10.1016/S0168-9002(00)00488-5. arXiv:hep-ex/0002044

73. H1 Collaboration, V. Andreev et al., Eur. Phys. J. C **75**, 65 (2015). https://doi.org/10.1140/epjc/s10052-014-3223-6. arXiv:1406.4709

74. H1 Collaboration, F.D. Aaron et al., JHEP **1209**, 061 (2012). https://doi.org/10.1007/JHEP09(2012)061. arXiv:1206.7007

75. M. Peez, Search for deviations from the standard model in high transverse energy processes at the electron proton collider HERA. Ph.D. thesis (2003). https://doi.org/10.3204/DESY-THESIS-2003-023

76. S. Hellwig, Untersuchung der $D^* - \pi_{slow}$ Double Tagging Methode in Charmanalysen, diploma thesis, Hamburg U., (2004). http://www-h1.desy.de/psfiles/theses/

77. B. Portheault, Premiere mesure des sections efficaces de courant charge et neutre avec le faisceau de positrons polarise a HERA II et analyses QCD-electrofaibles. Ph.D. thesis, 2005. http://www-h1.desy.de/psfiles/theses/

78. R. Kogler, Measurement of jet production in deep-inelastic *ep* scattering at HERA. Ph.D. thesis, Hamburg U., (2011). https://doi.org/10.3204/DESY-THESIS-2011-003

79. H1 Collaboration, C. Adloff et al., Eur. Phys. J. C **30**, 1 (2003). https://doi.org/10.1140/epjc/s2003-01257-6. arXiv:hep-ex/0304003

80. U. Bassler, G. Bernardi, Nucl. Instrum. Methods A **361**, 197–208 (1995). https://doi.org/10.1016/0168-9002(95)00173-5. arXiv:hep-ex/9412004

81. U. Bassler, G. Bernardi, Nucl. Instrum. Methods A **426**, 583–598 (1999). https://doi.org/10.1016/S0168-9002(99)00044-3. arXiv:hep-ex/9801017

82. M. Arratia, D. Britzger, O. Long, B. Nachman, Nucl. Instrum. Methods A **1025**, 166164 (2022). https://doi.org/10.1016/j.nima.2021.166164. arXiv:2110.05505

83. M. Arratia, D. Britzger, O. Long, B. Nachman, JINST **17**, P07009 (2022). https://doi.org/10.1088/1748-0221/17/07/P07009. arXiv:2203.16722

84. R. Brun, F. Bruyant, M. Maire, A.C. McPherson, P. Zanarini, GEANT3: user's guide. 9 (1987). https://cds.cern.ch/record/1119728. published as: CERN-DD-EE-84-1

85. H. Fesefeldt, The Simulation of Hadronic Showers: Physics and Applications. PITHA-85-02 (1985)

86. G. Grindhammer, M. Rudowicz, S. Peters, Nucl. Instrum. Methods A **290**, 469 (1990). https://doi.org/10.1016/0168-9002(90)90566-O

87. H1 Collaboration, J. Gayler, Simulation of H1 calorimeter test data with GHEISHA and FLUKA, in *Workshop on Detector and Event Simulation in High-energy Physics (MC '91)* (1991). p. 312

88. M. Kuhlen, The Fast H1 detector Monte Carlo, in *26th International Conference on High-energy Physics* (1992), p. 1787–1790. https://doi.org/10.1063/1.43288

89. G. Grindhammer, S. Peters, The Parameterized simulation of electromagnetic showers in homogeneous and sampling calorimeters, in *International Conference on Monte Carlo Simulation in High-Energy and Nuclear Physics (MC '93)*. 2 (1993). arXiv:hep-ex/0001020

90. A. Glazov, N. Raicevic, A. Zhokin, Comput. Phys. Commun. **181**, 1008–1012 (2010). https://doi.org/10.1016/j.cpc.2010.02.004

91. DPHEP Collaboration, R. Mount et al., Data Preservation in High Energy Physics. DPHEP-2009-001, 11 (2009). arXiv:0912.0255

92. H1 Collaboration, M. Steder, J. Phys. Conf. Ser. **331**, 032051 (2011). https://doi.org/10.1088/1742-6596/331/3/032051

93. H1 Collaboration, D.M. South, M. Steder, J. Phys. Conf. Ser. **396**, 062019 (2012). https://doi.org/10.1088/1742-6596/396/6/062019. arXiv:1206.5200

94. DPHEP Collaboration, Z. Akopov et al., Status report of the dphep study group: towards a global effort for sustainable data preservation in high energy physics 5 (2012). arXiv:1205.4667

95. H1 Collaboration, D. Britzger, S. Levonian, S. Schmitt, D. South, EPJ Web Conf. **251**, 03004 (2021). https://doi.org/10.1051/epjconf/202125103004. arXiv:2106.11058

96. DPHEP Collaboration, T. Basaglia et al., Eur. Phys. J. C **83**, 795 (2023). https://doi.org/10.1140/epjc/s10052-023-11885-1. arXiv:2302.03583

97. R. Brun, F. Rademakers, Nucl. Instrum. Methods A **389**, 81–86 (1997). https://doi.org/10.1016/S0168-9002(97)00048-X

98. K. Charchula, G.A. Schuler, H. Spiesberger, Comput. Phys. Commun. **81**, 381–402 (1994). https://doi.org/10.1016/0010-4655(94)90086-8

99. H. Jung, Comput. Phys. Commun. **86**, 147–161 (1995). https://doi.org/10.1016/0010-4655(94)00150-Z

100. L. Lönnblad, Comput. Phys. Commun. **71**, 15–31 (1992). https://doi.org/10.1016/0010-4655(92)90068-A

101. A. Kwiatkowski, H. Spiesberger, H.J. Möhring, Comput. Phys. Commun. **69**, 155–172 (1992). https://doi.org/10.1016/0010-4655(92)90136-M

102. J. Pumplin, D.R. Stump, J. Huston, H.L. Lai, P.M. Nadolsky, W.K. Tung, JHEP **07**, 012 (2002). https://doi.org/10.1088/1126-6708/2002/07/012. arXiv:hep-ph/0201195

103. B. Andersson, G. Gustafson, G. Ingelman, T. Sjöstrand, Phys. Rep. **97**, 31–145 (1983). https://doi.org/10.1016/0370-1573(83)90080-7

104. T. Sjöstrand, PYTHIA 5.7 and JETSET 7.4: Physics and manual, 2 (1994). arXiv:hep-ph/9508391

105. ALEPH Collaboration, R. Barate et al., Phys. Rep. **294**, 1–165 (1998). https://doi.org/10.1016/S0370-1573(97)00045-8

106. T. Sjöstrand, Comput. Phys. Commun. **82**, 74–90 (1994). https://doi.org/10.1016/0010-4655(94)90132-5

107. T. Sjöstrand, L. Lönnblad, S. Mrenna, PYTHIA 6.2: Physics and manual (2001). arXiv:hep-ph/0108264

108. T. Abe, Comput. Phys. Commun. **136**, 126–147 (2001). https://doi.org/10.1016/S0010-4655(00)00246-0. arXiv:hep-ph/0012029

109. A. Courau, P. Kessler, Phys. Rev. D **46**, 117–124 (1992). https://doi.org/10.1103/PhysRevD.46.117

110. E. Perez, L. Schoeffel, L. Favart, MILOU: a Monte-Carlo for deeply virtual Compton scattering. DESY-04-228 (2004). arXiv:hep-ph/0411389

111. T. Sjöstrand, S. Ask, J.R. Christiansen, R. Corke, N. Desai, P. Ilten, S. Mrenna, S. Prestel, C.O. Rasmussen, P.Z. Skands, Comput. Phys. Commun. **191**, 159–177 (2015). https://doi.org/10.1016/j.cpc.2015.01.024. arXiv:1410.3012

112. C. Bierlich et al., A comprehensive guide to the physics and usage of PYTHIA 8.3. LU-TP 22-16 (2022). arXiv:2203.11601

113. B. Cabouat, T. Sjöstrand, Eur. Phys. J. C **78**, 226 (2018). https://doi.org/10.1140/epjc/s10052-018-5645-z. arXiv:1710.00391

114. W.T. Giele, D.A. Kosower, P.Z. Skands, Phys. Rev. D **78**, 014026 (2008). https://doi.org/10.1103/PhysRevD.78.014026. arXiv:0707.3652

115. W.T. Giele, D.A. Kosower, P.Z. Skands, Phys. Rev. D **84**, 054003 (2011). https://doi.org/10.1103/PhysRevD.84.054003. arXiv:1102.2126

116. W.T. Giele, L. Hartgring, D.A. Kosower, E. Laenen, A.J. Larkoski, J.J. Lopez-Villarejo, M. Ritzmann, P. Skands, PoS DIS2013, 165 (2013). https://doi.org/10.22323/1.191.0165. arXiv:1307.1060

117. N. Fischer, S. Prestel, M. Ritzmann, P. Skands, Eur. Phys. J. C **76**, 589 (2016). https://doi.org/10.1140/epjc/s10052-016-4429-6. arXiv:1605.06142

118. S. Höche, S. Prestel, Eur. Phys. J. C **75**, 461 (2015). https://doi.org/10.1140/epjc/s10052-015-3684-2. arXiv:1506.05057

119. S. Höche, S. Prestel, Phys. Rev. D **96**, 074017 (2017). https://doi.org/10.1103/PhysRevD.96.074017. arXiv:1705.00742

120. S. Höche, F. Krauss, S. Prestel, JHEP **10**, 093 (2017). https://doi.org/10.1007/JHEP10(2017)093. arXiv:1705.00982

121. PDF4LHC Working Group Collaboration, R.D. Ball et al., J. Phys. G **49**, 080501 (2022). https://doi.org/10.1088/1361-6471/ac7216. arXiv:2203.05506

122. A. Banfi, S. Ferrario Ravasio, B. Jäger, A. Karlberg, F. Reichenbach, G. Zanderighi, JHEP **02**, 023 (2024). https://doi.org/10.1007/JHEP02(2024)023. arXiv:2309.02127

123. P. Nason, JHEP **11**, 040 (2004). https://doi.org/10.1088/1126-6708/2004/11/040. arXiv:hep-ph/0409146

124. S. Frixione, P. Nason, C. Oleari, JHEP **11**, 070 (2007). https://doi.org/10.1088/1126-6708/2007/11/070. arXiv:0709.2092

125. S. Frixione, Z. Kunszt, A. Signer, Nucl. Phys. B **467**, 399–442 (1996). https://doi.org/10.1016/0550-3213(96)00110-1. arXiv:hep-ph/9512328

126. J. Bellm et al., Eur. Phys. J. C **76**, 196 (2016). https://doi.org/10.1140/epjc/s10052-016-4018-8. arXiv:1512.01178

127. S. Gieseke, P. Stephens, B. Webber, JHEP **12**, 045 (2003). https://doi.org/10.1088/1126-6708/2003/12/045. arXiv:hep-ph/0310083

128. B.R. Webber, Nucl. Phys. B **238**, 492–528 (1984). https://doi.org/10.1016/0550-3213(84)90333-X

129. G. Marchesini, B.R. Webber, G. Abbiendi, I.G. Knowles, M.H. Seymour, L. Stanco, Comput. Phys. Commun. **67**, 465–508 (1992). https://doi.org/10.1016/0010-4655(92)90055-4

130. S. Frixione, B.R. Webber, JHEP **06**, 029 (2002). https://doi.org/10.1088/1126-6708/2002/06/029. arXiv:hep-ph/0204244

131. S. Platzer, S. Gieseke, Eur. Phys. J. C **72**, 2187 (2012). https://doi.org/10.1140/epjc/s10052-012-2187-7. arXiv:1109.6256

132. C. Bierlich et al., SciPost Phys. **8**, 026 (2020). https://doi.org/10.21468/SciPostPhys.8.2.026. arXiv:1912.05451

133. Sherpa Collaboration, E. Bothmann et al., SciPost Phys. **7**, 034 (2019). https://doi.org/10.21468/SciPostPhys.7.3.034. arXiv:1905.09127

134. T. Gleisberg, S. Höche, F. Krauss, M. Schönherr, S. Schumann, F. Siegert, J. Winter, JHEP **02**, 007 (2009). https://doi.org/10.1088/1126-6708/2009/02/007. arXiv:0811.4622

135. C. Duhr, S. Höche, F. Maltoni, JHEP **08**, 062 (2006). https://doi.org/10.1088/1126-6708/2006/08/062. arXiv:hep-ph/0607057

136. S. Catani, F. Krauss, R. Kuhn, B.R. Webber, JHEP **11**, 063 (2001). https://doi.org/10.1088/1126-6708/2001/11/063. arXiv:hep-ph/0109231

137. S. Catani, M.H. Seymour, Nucl. Phys. B **485**, 291–419 (1997). https://doi.org/10.1016/S0550-3213(96)00589-5. (Erratum: Nucl. Phys. B 510, 503–504 (1998)). arXiv:hep-ph/9605323

138. S. Schumann, F. Krauss, JHEP **03**, 038 (2008). https://doi.org/10.1088/1126-6708/2008/03/038. arXiv:0709.1027

139. J.-C. Winter, F. Krauss, G. Soff, Eur. Phys. J. C **36**, 381–395 (2004). https://doi.org/10.1140/epjc/s2004-01960-8. arXiv:hep-ph/0311085

140. T. Sjöstrand, S. Mrenna, P.Z. Skands, JHEP **05**, 026 (2006). https://doi.org/10.1088/1126-6708/2006/05/026. arXiv:hep-ph/0603175

141. S. Schumann, S. Höche, D. Reichelt, M. Knobbe, F. Krauss et al., Predictions with the pre-release version of Sherpa 3. Private communication (2023)

142. G.S. Chahal, F. Krauss, SciPost Phys. **13**, 019 (2022). https://doi.org/10.21468/SciPostPhys.13.2.019. arXiv:2203.11385

143. OpenLoops 2 Collaboration, F. Buccioni, J.-N. Lang, J.M. Lindert, P. Maierhöfer, S. Pozzorini, H. Zhang, M.F. Zoller, Eur. Phys. J. C **79**, 866 (2019). https://doi.org/10.1140/epjc/s10052-019-7306-2. arXiv:1907.13071

144. S. Höche, F. Krauss, S. Schumann, F. Siegert, JHEP **05**, 053 (2009). https://doi.org/10.1088/1126-6708/2009/05/053. arXiv:0903.1219

145. S. Höche, F. Krauss, M. Schönherr, F. Siegert, JHEP **04**, 027 (2013). https://doi.org/10.1007/JHEP04(2013)027. arXiv:1207.5030

146. CASCADE Collaboration, S. Baranov et al., Eur. Phys. J. C **81**, 425 (2021). https://doi.org/10.1140/epjc/s10052-021-09203-8. arXiv:2101.10221

147. A. van Hameren, Comput. Phys. Commun. **224**, 371–380 (2018). https://doi.org/10.1016/j.cpc.2017.11.005. arXiv:1611.00680

148. A.V. Lipatov, M.A. Malyshev, S.P. Baranov, Eur. Phys. J. C **80**, 330 (2020). https://doi.org/10.1140/epjc/s10052-020-7898-6. arXiv:1912.04204

149. F. Hautmann, H. Jung, A. Lelek, V. Radescu, R. Zlebcik, Phys. Lett. B **772**, 446–451 (2017). https://doi.org/10.1016/j.physletb.2017.07.005. arXiv:1704.01757

150. H. Jung, S. Taheri Monfared, T. Wening, Phys. Lett. B **817**, 136299 (2021). https://doi.org/10.1016/j.physletb.2021.136299. arXiv:2102.01494

151. A. Gehrmann-De Ridder, T. Gehrmann, E.W.N. Glover, A. Huss, T.A. Morgan, JHEP **07**, 133 (2016). https://doi.org/10.1007/JHEP07(2016)133. arXiv:1605.04295

152. J. Currie, T. Gehrmann, A. Huss, J. Niehues, JHEP **07**, 018 (2017). https://doi.org/10.1007/JHEP07(2017)018 (Erratum: JHEP 12, 042 (2020)). arXiv:1703.05977

153. J. Currie, T. Gehrmann, J. Niehues, Phys. Rev. Lett. **117**, 042001 (2016). https://doi.org/10.1103/PhysRevLett.117.042001. arXiv:1606.03991

154. M. Knobbe, D. Reichelt, S. Schumann, JHEP **09**, 194 (2023). https://doi.org/10.1007/JHEP09(2023)194. arXiv:2306.17736

155. S. Höche, S. Kuttimalai, Y. Li, Phys. Rev. D **98**, 114013 (2018). https://doi.org/10.1103/PhysRevD.98.114013. arXiv:1809.04192

156. E. Gerwick, S. Höche, S. Marzani, S. Schumann, JHEP **02**, 106 (2015). https://doi.org/10.1007/JHEP02(2015)106. arXiv:1411.7325

157. D. Reichelt, S. Caletti, O. Fedkevych, S. Marzani, S. Schumann, G. Soyez, JHEP **03**, 131 (2022). https://doi.org/10.1007/JHEP03(2022)131. arXiv:2112.09545

158. D. Kang, C. Lee, I. W. Stewart, PoS DIS2015, **142** (2015). https://doi.org/10.22323/1.247.0142

159. J. Currie, T. Gehrmann, E.W.N. Glover, A. Huss, J. Niehues, A. Vogt, JHEP **05**, 209 (2018). https://doi.org/10.1007/JHEP05(2018)209. arXiv:1803.09973

160. V. Bertone, S. Carrazza, J. Rojo, Comput. Phys. Commun. **185**, 1647–1668 (2014). https://doi.org/10.1016/j.cpc.2014.03.007. arXiv:1310.1394

161. V. Bertone, PoS DIS2017, 201 (2018). https://doi.org/10.22323/1.297.0201. arXiv:1708.00911

162. S. Moch, J.A.M. Vermaseren, A. Vogt, Nucl. Phys. B **688**, 101 (2004). https://doi.org/10.1016/j.nuclphysb.2004.03.030. arXiv:hep-ph/0403192

163. A. Vogt, S. Moch, J.A.M. Vermaseren, Nucl. Phys. B **691**, 129 (2004). https://doi.org/10.1016/j.nuclphysb.2004.04.024. arXiv:hep-ph/0404111

164. S. Moch, J.A.M. Vermaseren, A. Vogt, Phys. Lett. B **606**, 123–129 (2005). https://doi.org/10.1016/j.physletb.2004.11.063. arXiv:hep-ph/0411112

165. J.A.M. Vermaseren, A. Vogt, S. Moch, Nucl. Phys. B **724**, 3–182 (2005). https://doi.org/10.1016/j.nuclphysb.2005.06.020. arXiv:hep-ph/0504242

166. H1 Collaboration, V. Andreev et al., Eur. Phys. J. C **77**, 791 (2017). https://doi.org/10.1140/epjc/s10052-017-5314-7 (Erratum: Eur.Phys.J.C 81, 738 (2021)). arXiv:1709.07251

167. J. McGowan, T. Cridge, L.A. Harland-Lang, R.S. Thorne, Eur. Phys. J. C **83**, 185 (2023). https://doi.org/10.1140/epjc/s10052-023-11236-0. arXiv:2207.04739

168. S. Moch, B. Ruijl, T. Ueda, J.A.M. Vermaseren, A. Vogt, JHEP **10**, 041 (2017). https://doi.org/10.1007/JHEP10(2017)041. arXiv:1707.08315

169. A. Vogt, F. Herzog, S. Moch, B. Ruijl, T. Ueda, J.A.M. Vermaseren, PoS LL2018, 050 (2018). https://doi.org/10.22323/1.303.0050. arXiv:1808.08981

170. S. Moch, B. Ruijl, T. Ueda, J.A.M. Vermaseren, A. Vogt, Phys. Lett. B **825**, 136853 (2022). https://doi.org/10.1016/j.physletb.2021.136853. arXiv:2111.15561

171. V. Blobel, Unfolding Methods in High-energy Physics Experiments, in *Proceedings, CERN School of Computing: Aiguablava, Spain, September 9-22 1984*. DESY-84-118 (1984)

172. S. Schmitt, JINST **7**, T10003 (2012). https://doi.org/10.1088/1748-0221/7/10/T10003. arXiv:1205.6201

173. C.M. Stein, Ann. Stat. **9**, 1135–1151 (1981)

174. H1 Collaboration, C. Adloff et al., Eur. Phys. J. C **13**, 609 (2000). https://doi.org/10.1007/s100520050721. arXiv:hep-ex/9908059

175. H1 Collaboration, C. Adloff et al., Eur. Phys. J. C **21**, 33–61 (2001). https://doi.org/10.1007/s100520100720. arXiv:hep-ex/0012053

176. H1 Collaboration, C. Adloff et al., Eur. Phys. J. C **19**, 269 (2001). https://doi.org/10.1007/s100520100607. arXiv:hep-ex/0012052

177. H1 Collaboration, F.D. Aaron et al., Eur. Phys. J. C **71**, 1579 (2011). https://doi.org/10.1140/epjc/s10052-011-1579-4. arXiv:1012.4355

178. P.A. Movilla Fernandez, http://nbn-resolving.org/urn:nbn:de:hbz:82-opus-4836 *Studien zur Quantenchromodynamik und Messung der starken Kopplungskonstanten α_s bei $\sqrt{s}$ = 14-GeV - 44-GeV mit dem JADE-Detektor*. PhD thesis (2002)

179. C. Pahl, S. Bethke, O. Biebel, S. Kluth, J. Schieck, Eur. Phys. J. C **64**, 533–547 (2009). https://doi.org/10.1140/epjc/s10052-009-1167-z. arXiv:0904.0786

180. H1 Collaboration, "H1 Publications," 2024. https://www-h1.desy.de/publications/H1publication.short_list.html

181. S. Shushkevich, Measurement of the Neutral Current Reaction at high Q^2 in the H1 Experiment at HERA II. Ph.D. thesis, Munich U. (2012)

182. A. Arbuzov, D.Y. Bardin, J. Blümlein, L. Kalinovskaya, T. Riemann, Comput. Phys. Commun. **94**, 128–184 (1996). https://doi.org/10.1016/0010-4655(96)00005-7. arXiv:hep-ph/9511434

183. H. Spiesberger, EPRC: a program package for electroweak physics at HERA, in *Contributions to the proceedings of the '95–'96 Workshop on Future Physics at HERA, Part 2* (1995)

184. H1 Collaboration, V. Andreev et al., Eur. Phys. J. C **78**, 777 (2018). https://doi.org/10.1140/epjc/s10052-018-6236-8. arXiv:1806.01176

185. H1 Collaboration, V. Andreev et al., arXiv:2403.08982

186. H1 Collaboration, V. Andreev et al., Eur. Phys. J. C **77**, 215 (2017). https://doi.org/10.1140/epjc/s10052-017-4717-9. arXiv:1611.03421

187. H1 and ZEUS Collaboration, H. Abramowicz et al., Eur. Phys. J. C **75**, 580 (2015). https://doi.org/10.1140/epjc/s10052-015-3710-4. arXiv:1506.06042

188. A. Dainese, M. Mangano, A.B. Meyer, A. Nisati, G. Salam, M.A. Vesterinen, (eds.) Report on the Physics at the HL-LHC,and Perspectives for the HE-LHC, vol. 7/2019 of CERN Yellow Reports: Monographs. CERN, Geneva, Switzerland (2019). https://doi.org/10.23731/CYRM-2019-007

189. I. Zurbano Fernandez et al., CERN Yellow Reports: Monographs 10/2020 (2020). https://doi.org/10.23731/CYRM-2020-0010

190. H1 Collaboration, V. Andreev et al., arXiv:2303.13620

191. R. Abdul Khalek et al., Nucl. Phys. A **1026**, 122447 (2022). https://doi.org/10.1016/j.nuclphysa.2022.122447. arXiv:2103.05419

192. F.C.C. Collaboration, A. Abada et al., Eur. Phys. J. C **79**, 474 (2019). https://doi.org/10.1140/epjc/s10052-019-6904-3

193. LHeC, FCC-he Study Group Collaboration, P. Agostini et al., J. Phys. G **48**, 110501 (2021). https://doi.org/10.1088/1361-6471/abf3ba. arXiv:2007.14491

194. I.W. Stewart, Precision Jet Physics in DIS. Talk presented at the Future Physics with HERA Data for Current and Planned Experiments (2014). https://indico.desy.de/event/10523/contributions/1919/